THE PHYSICS OF THE ATMOSPHERES OF COOL WHITE DWARFS

By

Piotr Kowalski

Dissertation

Submitted to the Faculty of the

Graduate School of Vanderbilt University

in partial fulfillment of the requirements

for the degree of

DOCTOR OF PHILOSOPHY

in

Physics

December, 2006

Nashville, Tennessee

Approved:

Professor Didier Saumon

Professor Robert O'Dell

Professor Robert Knop

Professor Medford Webster

Professor David Weintraub

ACKNOWLEDGMENTS

I would like to thank my thesis advisor, Dr. Didier Saumon, for his support and scientific guidance beginning with my first day at Vanderbilt and up to my last day at Los Alamos. As my advisor and mentor, he contributed much to my scientific development and my residence as a foreigner in the U.S.A.

I am especially thankful to Prof. Lidia Smentek, without whom this dissertation would not have seen the light of day. At the end of my education at Nicolaus Copernicus University, she encouraged me to enter graduate studies at Vanderbilt University, and she provided me with valuable advice throughout my Ph.D. studies.

I am grateful to all of those with whom I have had the pleasure to work and who have provided assistance during my work on this dissertation, especially, the Applied Physics division at Los Alamos National Laboratory for its hospitality and support that I received during the past four years. The time I spent as a graduate research assistant at the Los Alamos National Laboratory has been a great scientific adventure.

Many thanks to Vanderbilt University, the U.S. Department of Energy, the National Science Foundation, and the National Aeronautic and Space Administration for their financial support during my graduate studies.

Last, but not least, I am grateful to my wife Magdalena for her love and support during the years we were separated by an ocean and during last two years, when we were reunited again. The continuing inspiration I have received from her each day has been crucial for the completion of this dissertation.

TABLE OF CONTENTS

LIST OF TABLES

LIST OF FIGURES

LIST OF ABBREVIATIONS AND SYMBOLS

The symbols that are often used throughout the dissertation are listed below. When a symbol is used for a different physical quantity from that listed below, it is clearly indicated in the text. The cgs system of units is used throughout.

Symbol	description
B_ν	Planck function
bb	Bound-bound
bf	Bound-free
CIA	Collision induced absorption
c	Speed of light
DFT	Density functional theory
$F_{\rm conv}$	Convective flux
ff	Free-free
$F_{\rm rad}$	Radiative flux
GGA	General gradient approximation
G	Gravitational constant
g	Gravity
P	pressure
h, $\hbar$	Planck constant
H_ν	Eddington flux
ISM	Interstellar medium
k_B	Boltzman constant
LDA	Local density approximation
L	Luminosity
MC	Monte Carlo
m	Mass of a particle
M	Mass of white dwarf
$M_\odot$	mass of the Sun
n	Number density
QMD	Quantum molecular dynamics
R	Radius of the white dwarf
SED	Spectral energy distribution
$T_{\rm eff}$	Effective temperature
T	Temperature
V	Volume
WD	White dwarf
χ_ν	Mass absorption coefficient
χ_R	Rosseland mass absorption coefficient
ρ	Density
σ_R	Stefan-Boltzman constant
τ	Optical depth
$\tau_{\rm R}$	Rosseland optical depth
ν	Frequency
∇	Temperature gradient ($d\ln T/d\ln P$)
∇_A	Adiabatic temperature gradient

CHAPTER I

INTRODUCTION

In this chapter we present the basic facts about white dwarfs that motivate and provide the context of this dissertation. This information can be found in a number of detailed reviews on white dwarfs: Hansen (2004); Fontaine et al. (2001); Koester (2002); and also in D'Antona & Mazzitelli (1990).

1.1 White Dwarf Stars

1.1.1 Physical Properties of White Dwarfs

White dwarfs represent the final state of evolution for about 97% of main sequence stars. Due to the lack of nuclear energy sources, these stellar remnants support themselves against gravity through the pressure of degenerate electron gas and simply cool off, slowly releasing their thermal energy to space (Mestel, 1952). The existence of these stars was realized for the first time through the measurements of the spectrum of Sirius B by Adams (1915). The measured luminosity and effective temperature of Sirius B resulted in a very small radius of $\sim$ 18000 km (modern value: $\sim$ 5200 km, Shapiro & Teukolsky (1983)), which was confirmed later through the measurements of the gravitational redshifts of the spectral lines (Adams, 1925). Such a small radius combined with the mass of the star, thought at that time to be $\sim 0.75 - 0.95\,M_{\odot}$ (modern value: $\sim 1.05\,M_{\odot}$, Shapiro & Teukolsky (1983)) gave a large internal density of $\sim 10^5$ g/cm^3. The nature of such dense matter was not understood until the formulation of Fermi-Dirac statistics by Dirac (1926), and its application to white dwarfs (Fowler, 1926).

A white dwarf is a compact star of about one solar mass and an Earth-like radius of $\sim 9500 - 4000$ km. The analysis of white dwarfs in the galactic disk reveals that the mass distribution has a mean of $0.59\,M_{\odot}$ with a narrow dispersion of $\sim 0.13\,M_{\odot}$ (Bergeron et al., 1997). The small radii of these stars result in a large gravity at their surface, $\log\, g\,(\mathrm{cm/s^2}) \sim 8$ compared with $\log\, g = 4.4$ for the Sun, and a compositionally stratified internal structure (Schatzman, 1958). A

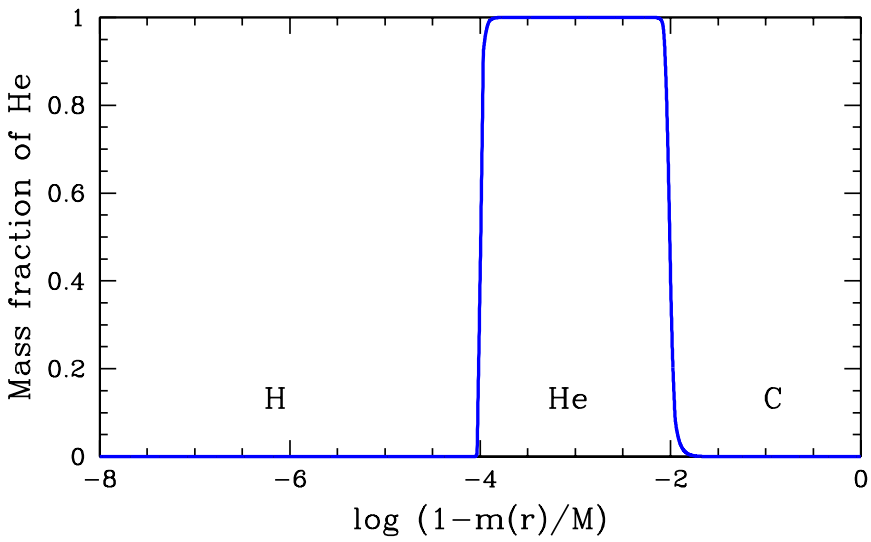

Figure 1: Model of the internal structure of a typical white dwarf of pure C core composition. The structure shows three distinct regions of nearly pure C, He and H composition. The blue line marks the mass fraction of helium, $m(r)$ indicates the mass contained within a distance r from the center of the star. The parameters of this model are: $M = 0.6\,M_{\odot}$, $T_{\rm eff} = 4228\,{\rm K}$, $\log g = 8.03$, $M_{\rm He}/M = 10^{-2}$ and $M_{\rm H}/M = 10^{-4}$. Model provided by Gilles Fontaine.

model of the internal structure of a white dwarf is presented in Fig. 1. As a result of the helium (He) nuclear burning in the pre-white dwarf stage, the average star consist of a massive C/O core (Salaris et al., 1997; Hernanz et al., 1994), which accounts for $\sim 99\%$ of its total mass, M. The core is surrounded by a He envelope ($\sim 10^{-3} - 10^{-2}\,M$), on top of which a tiny surface hydrogen (H) layer is usually found ($\lesssim 10^{-4}\,M$) (Fontaine et al., 2001; Bradley, 2001). The effective temperature varies from $\sim 150000\,{\rm K}$ for newly formed white dwarfs to $\sim 4000\,{\rm K} - 3000\,{\rm K}$ for the coolest and oldest white dwarfs detected. The luminosity ranges between $\sim 100 - 1000\,L_{\odot}$ for the hottest stars and $\sim 10^{-4.7} L_{\odot}$ for the known faintest stars (Fontaine et al., 2001).

The mass-radius relation for white dwarfs (Shapiro & Teukolsky, 1983),

$$M \sim R^{-3} \tag{1}$$

derived assuming that the pressure is provided by a non-relativistic free electron gas, shows that

more massive white dwarfs have smaller radii. There exists an upper limit to the mass of a white dwarf. This limit comes from the fact that the more massive stars are more compact and, with the increase in the density, the electron gas eventually becomes relativistic. The ratio of the energy of the relativistic electron gas to the gravitational potential energy of the star is independent of the radius of the white dwarf. Therefore, there exists a maximal number of ions, $N_{\max}$ above which the total energy becomes negative and decreases with R causing the gravitational collapse of the star. This number is related to the basic physical constants by (Shapiro & Teukolsky, 1983) as

$$N_{\max} \sim \left(\frac{\hbar c}{G m_{\rm I}^2}\right)^{3/2}, \tag{2}$$

where $m_{\rm I}$ is the average mass of the ions. The corresponding maximum mass of $N_{\max} m_{\rm I} \sim 1.5 M_{\odot}$, is known as the *Chandrasekhar limit* (Chandrasekhar, 1931). When this limit is reached, such as by the transfer of material from a companion star onto a white dwarf in a binary system, a Type Ia supernovae explosion of the white dwarf results.

1.1.2 Evolution of White Dwarfs

The cooling theory of the white dwarf stars was originally developed by Mestel (1952). Because of the depletion of nuclear energy sources, a white dwarf can only cool off. As the pressure of a degenerate electron gas is independent of temperature, a white dwarf evolves at essentially a constant radius. The composition of the core (C/O profile) is determined by the poorly known $^{12}\mathrm{C}(\alpha,\gamma)^{16}\mathrm{O}$ burning rate in the red giant phase of evolution, and the evolution history of the progenitor star (Salaris et al., 1997; Hernanz et al., 1994). As the degenerate electrons are excellent conductors of heat, the core is nearly isothermal (Mestel, 1952; Tassoul et al., 1990). However, these electrons do not contribute to the thermal energy reservoir as they occupy the lowest available energy states. Therefore, essentially all the thermal energy is stored in the ions. As the core temperature decreases, the Coulomb interactions between the ions become more and more significant until the fluid plasma starts to crystallize. For stars with $M = 0.6 M_{\odot}$, this phenomenon occures at $T_{\rm eff} \sim 5000\,\mathrm{K}$ (Fontaine et al., 2001).

Very young white dwarfs lose their thermal energy by emitting neutrinos (Beaudet et al., 1967).

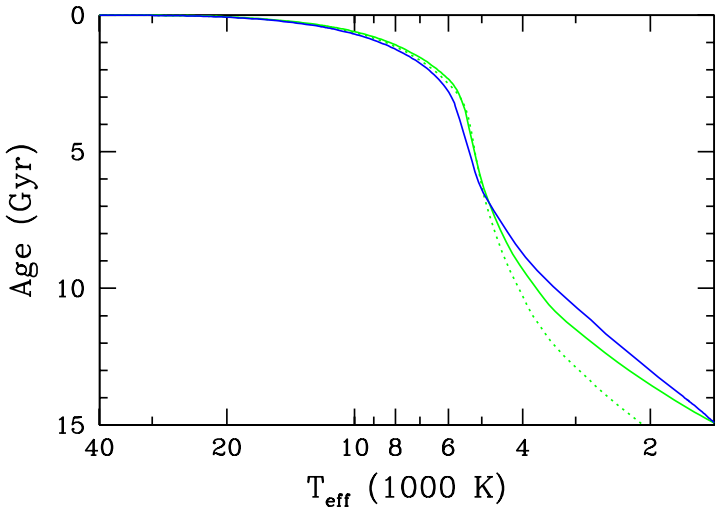

Figure 2: Cooling ages of white dwarfs of Fontaine et al. (2001). The green curves represent the cooling of typical white dwarf ($M = 0.6\,M_{\odot}$) with a surface H layer ($M_{\rm H}/M = 10^{-4}$), $M_{\rm He}/M = 10^{-2}$ and core compositions: C/O = 1 (solid) and pure C (dotted). The solid blue line represents the cooling ages of a white dwarf without a surface hydrogen layer. The effect of the composition of the core is clearly visible below $T_{\rm eff} < 5000\,{\rm K}$.

After this initial period of rapid cooling, the cooling rate depends on the amount of thermal energy stored in the core and the efficiency of its transport through the opaque outer layers and, ultimately, radiation to the interstellar medium. As the transport of energy through the envelope is slowest, its physical properties determine the cooling rate. In the envelopes of stars with $T_{\rm eff} \gtrsim 12000\,{\rm K}$, the heat is transported mainly by radiative diffusion. For cooler stars the temperature gradient in the envelope results in the formation of a large superficial convection zone and more efficient energy transport (Tassoul et al., 1990).

Figure 2 shows how $T_{\rm eff}$ decreases with time for a typical model white dwarf. The cooling slows down significantly for $T_{\rm eff} \lesssim 8000\,{\rm K}$. The cooling rate at lower $T_{\rm eff}$ depends on the composition of the core and the properties of the atmosphere. As helium is much more transparent than hydrogen, a star without a surface hydrogen layer cools faster. In addition with further cooling, a convection zone extends deeper into the star and eventually reaches the core (Fontaine et al., 2001, 1974).

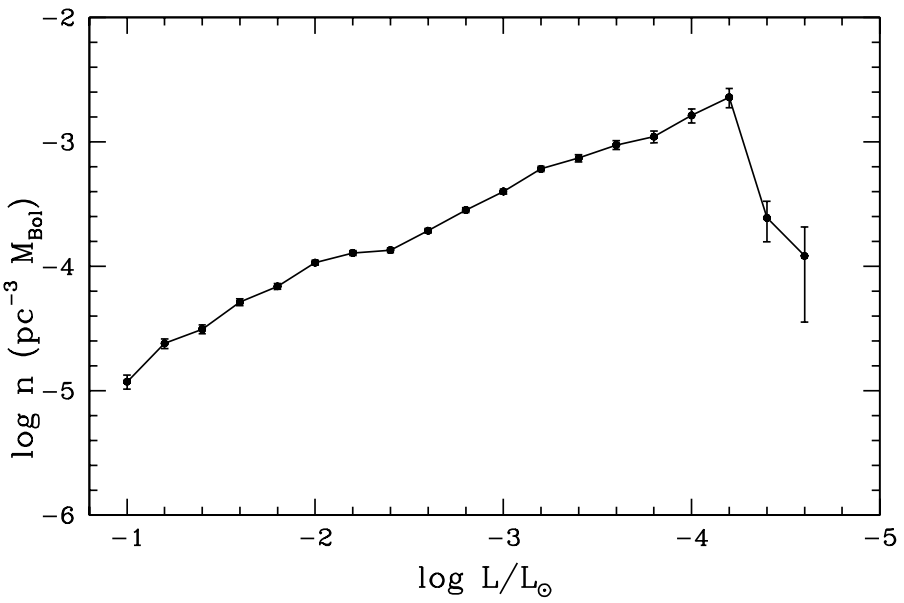

Figure 3: The white dwarf luminosity function of Harris et al. (2006) for the Galactic disk.

The direct convective coupling of the surface to the degenerate core causes a significant increase in the rate of energy transfer across the envelope (Fontaine et al., 2001). This phenomenon occurs in stars with $T_{\rm eff} \sim 6000\,{\rm K}$ and depends on the atmosphere composition and atmosphere models (Hansen, 1999). For instance, when non gray atmosphere models are used, an upward shift of the convective zone is produced that delays the surface-core coupling (Böhm et al., 1977). This coupling introduces an error in the calculated cooling time comparable to that produced by the unknown C/O core composition profile ($1-2\,{\rm Gyr}$, Fig. 2), and shows the importance of the properties of the atmosphere for calculating the cooling rate of cool white dwarfs.

The universe is $\sim 13.7\,{\rm Gyr}$ old and the coolest white dwarfs are probably $\sim 12\,{\rm Gyr}$ old. They have not had enough time to cool below $T_{\rm eff} \sim 3000\,{\rm K} - 2000\,{\rm K}$, and a cut off in the white dwarfs cooling sequences in stellar populations should be present. In fact, there is a large effort to use observed white dwarfs populations as chronometers to measure the age of the Milky Way and galactic and globular clusters (Winget et al., 1987; Wood et al., 1995; Liebert et al., 1979, 1988; Fontaine et al.,

2001; Hansen et al., 2002; Liebert et al., 2005; Richer et al., 2006; Harris et al., 2006; von Hippel, 2005). To achieve this goal, both theoretical and observed luminosity functions are constructed (Schmidt, 1959; Liebert et al., 1979, 1988). The luminosity function represent the number density of white dwarfs as a function of luminosity. In Fig. 3 we present the most recent determination of the luminosity function for the disk of the Milky Way based on the Sloan Digital Sky Survey (SDSS) (Harris et al., 2006). The white dwarf luminosity function shows two distinct features. First, there are more low luminosity stars indicating that the cooling time scale of white dwarfs increases with time. The second feature is the sudden drop in the number density of the coolest white dwarfs at $L \sim 10^{-4.4} L_{\odot}$, which is a consequence of the finite age of the Milky Way. Although white dwarf cosmochronology is beyond the scope of this work, we will elaborate on its application to the Milky Way and the closest globular clusters in Chapter 10.

1.2 Atmospheres of Cool White Dwarfs

1.2.1 The Spectral Classification and Spectral Evolution of White Dwarfs

The atmosphere of a star is the outermost surface layer that is directly observable. Observational and theoretical efforts over the last decades have revealed a complex picture of the time evolution of the white dwarf atmosphere chemical composition. Three main groups of white dwarfs are distinguished on the basis of their spectra (Sion et al., 1983): white dwarfs that show hydrogen lines (DA), white dwarfs that show only lines of atomic (DB) and singly ionized helium (DO), and white dwarfs that show continuum spectra without any lines (DC).

Hot White Dwarfs

Newly formed white dwarfs can have a hydrogen or helium rich atmospheric composition. DA white dwarfs have hydrogen-rich atmospheres and hot helium-rich white dwarfs will appears as DOs. As DO stars cool, He^+ recombines to form He and they gradually turn into DBs below $T_{\rm eff} \sim 45000\,{\rm K}$ (Chayer et al., 2005). The DA/(DO+DB) ratio increases as $T_{\rm eff}$ decreases, and by the time they reach the $T_{\rm eff} \sim 45000 - 30000\,{\rm K}$ there are no DB/DO stars left (Liebert et al., 1986). This increase is caused by the fast gravitational settling of helium ($\lesssim 10^8$ years, Schatzman (1958); Fontaine &

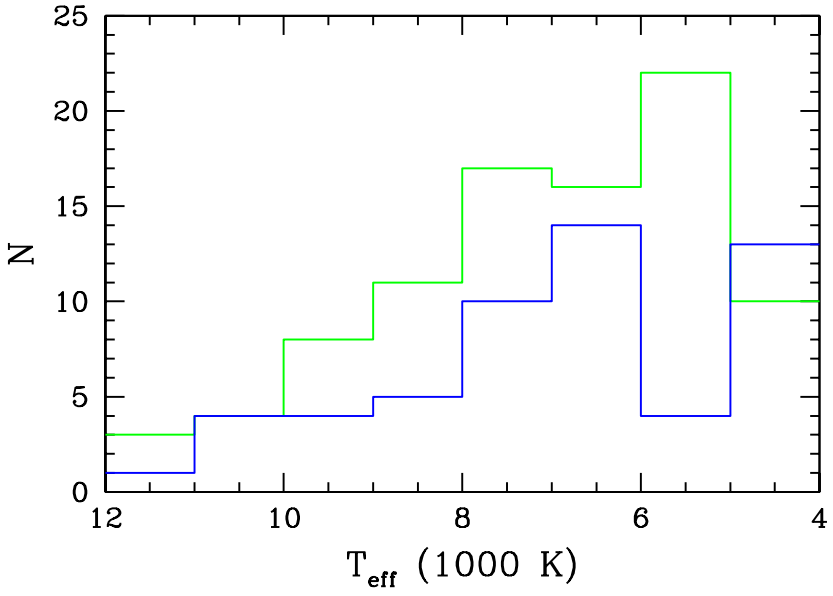

Figure 4: The effective temperature distribution of disk white dwarfs with H (green) and He (blue) atmospheres in the sample of Bergeron et al. (2001) as determined by the authors.

Michaud (1979)), caused by the high-surface gravity. For stars with $T_{\rm eff} \lesssim 30000\,{\rm K}$, convection in the He layer may mix helium with the superficial H layer (Tassoul et al., 1990). This process reverts a significant fraction of DA stars back to DB. By the time the stars reach $T_{\rm eff} \sim 11000\,{\rm K}$, the observed relative number of DA to DB white dwarfs is ~ 1 (Sion, 1984; Greenstein, 1986; Bergeron et al., 1997). This is also the temperature where helium lines become too weak to be detected and the DB stars convert into DC type.

Cool White Dwarfs

As white dwarfs cool further, their chemical evolution become more complicated. This is evident through the detection of some distinct peculiarities in samples of cool white dwarfs.

The first peculiarity outlined below will be addressed in this dissertation. There exists a distinct paucity of stars with helium-dominated atmospheres for $T_{\rm eff} \sim 5000\,{\rm K} - 6000\,{\rm K}$, the so called "non-DA gap" (Bergeron et al., 1997, 2001). This gap is illustrated in Fig. 4. The ratio of stars observed

in the galactic disk with He-rich atmospheres as compared to those with H-rich atmospheres is ~ 0.5 down to $T_{\rm eff} = 6000\,{\rm K}$. Between $6000 - 5000\,{\rm K}$ it drops to ~ 0.2, while at lower $T_{\rm eff}$ it rises again to > 1. The high-$T_{\rm eff}$ edge of the gap is probably related to the change in the surface composition of white dwarfs from helium to hydrogen through the accretion of hydrogen from the interstellar medium (Bergeron et al., 1997). The low-$T_{\rm eff}$ edge has been attributed to the convective mixing that should occur at $T_{\rm eff} \sim 5000\,{\rm K}$ (Tassoul et al., 1990; Bergeron et al., 1997). However, because of the finite extension of the surface convection zone, such mixing occurs for stars with a total mass of hydrogen $< 10^{-6}\,M$, whereas the asteroseismological observations of ZZ Ceti white dwarfs allow us to suspect that the average star possesses probably 100 times more hydrogen (Bradley, 2001; Fontaine et al., 2001). As hydrogen lines become too weak to be detected at $T \sim 4800\,{\rm K}$, almost all white dwarfs with $T_{\rm eff} < 5000\,{\rm K}$ are DC stars. More than half of them were identified as stars with He-rich atmospheres by Bergeron et al. (2001, 1997) (Fig. 4). In the absence of H or He spectral lines, the determination of the atmospheric composition of those stars was conducted by fitting of models to the spectral energy distributions. In view of the limitations in the model atmosphere used, this method is not as reliable as the direct detection of hydrogen lines.

For stars with $T_{\rm eff} < 5000\,{\rm K}$, the hydrogen is increasingly in the molecular form H_2, giving rise to a strong collision induced absorption (CIA) in the infra-red (IR) (Hansen, 1999; Saumon & Jacobson, 1999). Some ultra-cool white dwarfs with strong IR flux deficiency, most probably a result of CIA opacity caused by collisions of H_2 with He in a helium-rich atmosphere, have been discovered recently (Bergeron et al., 2005; Kilic et al., 2005; Gates et al., 2004; Bergeron & Leggett, 2002; Bergeron, 2001; Oppenheimer et al., 2001; Hodgkin et al., 2000). However, current models fail to reproduce their spectra or colors. This difficulty may be related to a poor description of the physics of dense helium.

For some stars with He-rich atmospheres, upward carbon diffusion from the core can penetrate far enough to reach the outer helium convection zone (Pelletier et al., 1986; MacDonald et al., 1998). The dredge-up of trace amounts of carbon (C) enriches the atmosphere in carbon and gives rise to C lines and the Swan bands of C_2 that characterize stars of spectral type DQ. There is a puzzling change in the DQ white dwarfs' cooling sequence. While stars with C_2 bands are detected down to

about 6500 K, they are not observed at lower temperatures (Bergeron et al., 1997; Koester & Knist, 2006; Dufour et al., 2005). Moreover, below this temperature peculiar DQ stars are found. They show absorption bands that are slightly different from the C_2 Swan bands. This phenomenon may be caused by a hydrocarbon compound, such as C_2H, that may form and outnumber C_2 if enough hydrogen (H/He $\sim$ 1), accreted from the interstellar medium, is present in the atmosphere (Schmidt et al., 1995; Bergeron et al., 1997). This result would be consistent with the conversion of DC into DA stars below $T_{\rm eff} \sim 6000$ K outlined in previous paragraph.

There is a group of white dwarfs that show spectral lines of heavier elements, such as Ca, Si, Na, Mg, and sometimes Fe. They are classified as DZ (no hydrogen lines) or DAZ (also showing hydrogen lines) stars. Their existence is thought to be the result of recent accretion (Dupuis et al., 1993; Wolff et al., 2002; Zuckerman et al., 2003; Kilic et al., 2006a) because the time for the gravitational settling of heavier elements in hydrogen and helium is very short, $\lesssim 10^8$ years (Dupuis et al., 1992).

1.2.2 Current State of Cool White Dwarf Atmospheres Modeling

As we mentioned in section 1.1.2, realistic atmospheres models must be used as the outer boundary conditions for a reliable calculation of the cooling of white dwarfs with $T_{\rm eff} < 6000$ K. The atmosphere models allow for the calculation of the emergent fluxes that is essential for the interpretation of the observed spectra and colors of white dwarfs, and the determination of the star's physical parameters, $T_{\rm eff}$, g, and atmospheric composition.

The physical conditions and opacities found in the atmospheres of cool white dwarfs are indicated in Figs. 5 and 6, respectively. Most of the physics included in the current models is only adequate to describe an ideal gas. These models are sufficient for the less extreme hydrogen-rich atmospheres (with the exception of an opacity source in the blue, discussed in Chapters VIII and IX), where $\rho < 0.01\,{\rm g/cm^3}$. On the other hand, the densities encountered in helium-rich atmospheres are as high as $2 - 3\,{\rm g/cm^3}$ and the input physics for the models, including opacities, must take into account the physics of dense fluids that affects the equation of state (EOS), chemistry, opacities, and introduce refraction in the transfer of radiation.

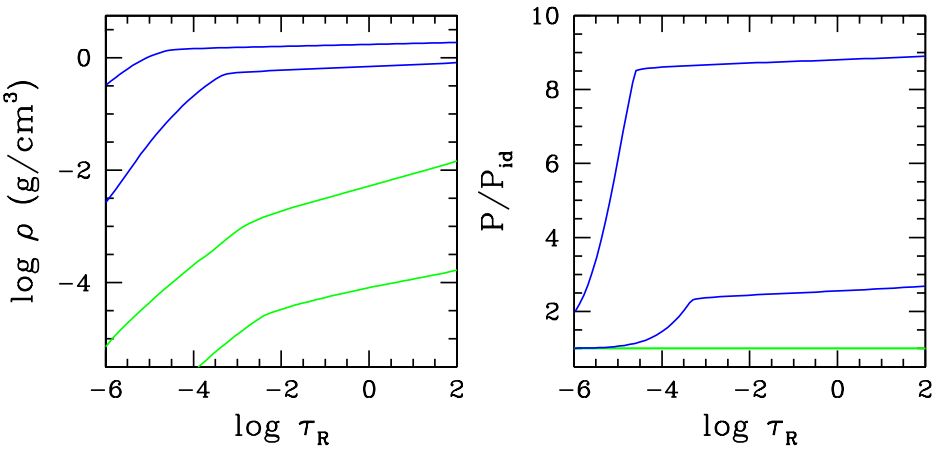

Figure 5: Density (left panel) and pressure (right panel) inside pure hydrogen (green lines) and pure helium (blue lines) atmosphere models with $T_{\rm eff} = 6000\,{\rm K}$ (lower lines) and $4000\,{\rm K}$ (upper lines). The pressure is expressed in terms of the ideal gas pressure. τ_R is the Rosseland mean optical depth.

The only high-density effects included in current modeling efforts are the density effects on CIA opacity from H_2 and the non ideal chemistry in pure hydrogen atmospheres (Saumon & Jacobson, 1999), and the introduction of a non ideal helium EOS in helium-rich atmospheres (Bergeron et al., 1995a). Additionally, corrections to the He^- free-free opacity and Rayleigh scattering in helium-rich atmospheres due to correlations can be as large as factor of 10 (Iglesias et al., 2002), but these effects have not been included in models so far. For cool white dwarfs atmospheres rich in helium, the extremely high density (Fig. 5) makes the computation of the chemistry and opacities extremely difficult because the theory for partially ionized, partially degenerate and dense material, especially helium, is incomplete (Hansen, 2004).

1.2.3 Outline of the Dissertation

The dating of stellar populations with the method of white dwarf cosmochronology provides an independent means of determining astrophysical ages that are not subject to the same systematic uncertainties as other methods. A comparison of the different methods applied to clusters, the disk of the Milky Way, the thick disk, and the halo will lead to a better calibration of astrophysical

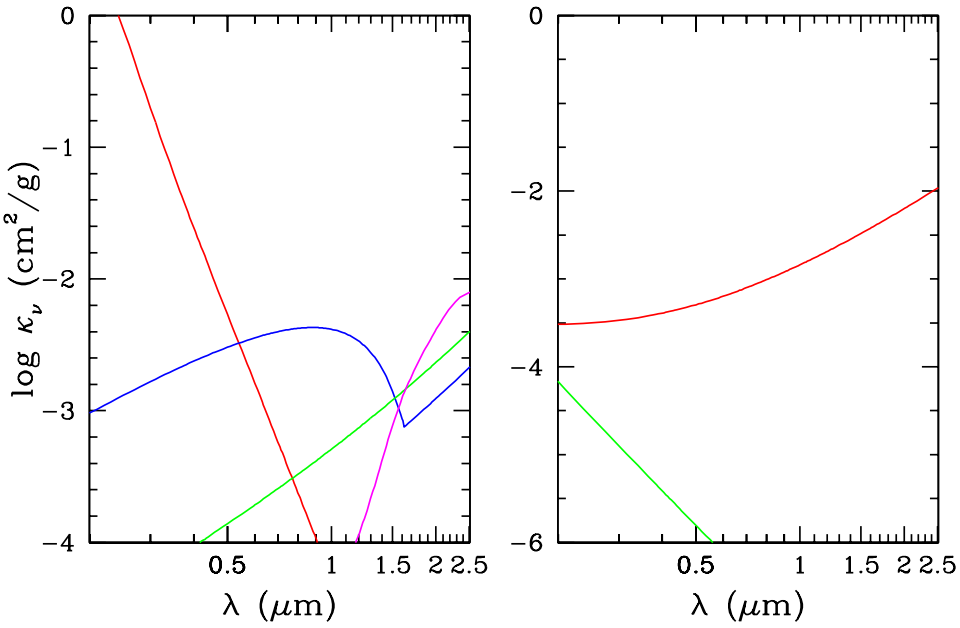

Figure 6: The most important sources of opacity in a photosphere of pure hydrogen (left panel) and pure helium (right panel) white dwarf atmosphere models of $T_{\rm eff} = 4500\,{\rm K}$ and $\log g = 8$. On the left panel the colors show - H Ly α red wing (red), H^- bb & bf (blue), H_2 CIA (magenta) and H_2^- ff (green); on the right panel - He^- ff (red) and Rayleigh scattering from He atoms (green). Note the different scales for κ_ν

clocks and a better understanding of the star formation history of the Milky Way. The main tool of white dwarf cosmochronology, the white dwarf luminosity function, can only be properly understood with reliable models for the interior and the atmospheres of cool white dwarfs. While substantial efforts have led to a good understanding of the interior physics, model atmospheres mostly rely on inadequate, ideal gas input physics. Our work aims to correct this situation by addressing nearly all of the most important dense physics effects pertaining to cool white dwarfs atmospheres. These effects include problems in radiative transfer, chemistry, and opacities. The resulting models will provide better surface boundary conditions for white dwarf cooling calculations, better ages for stellar populations, more reliable surface parameters ($T_{\rm eff}$, g and He/H composition) for individual stars, and a clearer picture of the spectral evolution of very cool white dwarfs.

In the next two chapters we describe the tools and methods used in this dissertation. In Chapter

II we describe how the atmosphere models are calculated. We discuss the energy transport through the atmosphere and the self-consistent solution of the equations that governs the structure of a stellar atmosphere structure model. In particular, our numerical solution for radiative transfer in a refractive medium is presented in detail. The description of the methods used to derive new input physics (EOS, chemistry, and opacities) for the calculation of dense atmosphere models follows in Chapter III.

In He-rich atmospheres the refractive index deviates significantly form unity. We have implemented our solution of refractive radiative transfer in our atmosphere code and its effect on the models is discussed in Chapter IV. This solution is the first detailed description of refractive effects in stellar atmosphere.

In dense helium-rich atmospheres, the inter-particle interactions are strong and interaction energies are often greater than the kinetic energies that affect the chemical equilibrium abundances of species (Fig 5). Using the statistical theory of fluids, we have developed models for the non ideal chemistry of the dominant and spectroscopically important species: He, e, He^+, H_2, H and H^- (Fig. 6). Our calculations are presented in Chapters V, VI, and VIII.

The He^- free-free opacity and Rayleigh scattering from He atoms are most important sources of opacity in helium rich atmospheres (Fig. 6). To account for the correlations in dense helium, we calculated the corrections to the cross sections of these absorption mechanism with the model of Iglesias et al. (2002). The He^- ff absorption depends on the ionization fraction of helium, which is poorly understood in the regime encountered in cool, helium-rich white dwarf atmospheres. To address this issue we performed a large investigation of dense helium, using both a statistical physics approach and state-of-the-art ab initio quantum calculations. We calculated the electron affinities in dense helium with ab initio quantum calculations and constructed the most physically realistic chemical model for the ionization equilibrium of dense helium accounting for the $e - He$, $He^+ - He$, and $He - He$ interactions. We obtained an independent estimate of the ionization fraction and free-free opacity of dense helium by conducting extensive ab initio quantum molecular dynamics simulations of dense helium. Our new results increase the ionization fraction by $2 - 3$ orders of magnitude compared to previous models (Bergeron et al., 1995a), making the He^- free-free opacity

dominant over Rayleigh scattering (Fig. 6). This study of dense He ionization and opacity is reported in Chapter VI.

There is a significant flux excess in the blue part of the spectrum ($\lambda < 5000$ Å) of pure hydrogen atmosphere models compared to the spectral energy distributions of cool white dwarfs (Bergeron et al., 1997). This excess indicates that a source of opacity is missing in the pure hydrogen atmosphere models. A suspected mechanism for this absorption is the pseudo-continuum opacity of hydrogen (Bergeron et al., 1997; Bergeron, 2001; Däppen et al., 1987). As the only model for this absorption mechanism of Däppen et al. (1987) predicts unrealistically high values for the pseudo-continuum opacity in white dwarf atmospheres, we constructed a more sophisticated and reliable model for this absorption mechanism. Our results indicate that the pseudo-continuum opacity is negligible in cool white dwarf atmospheres (Chapter IX).

Another potential source of absorption in the blue is the far red wing of the pressure-broadened Lyman α line (Wolff et al., 2002). We constructed for the first time a reliable model for this absorption mechanism, including the broadening of the Ly α line by $H - H_2$ collisions. This opacity mechanism turns out to be the missing opacity source and it is of great importance for understanding the surface composition of the coolest white dwarfs. Our new models include this source of opacity and reproduce the observations remarkably well (Chapter VII).

All the effects introduced in this dissertation were included in the calculation of a new grid of atmosphere models and spectra. The main features of these new models are discussed in Chapter X. In several instances these models depart qualitatively from previous work in astrophysically significant ways. We apply the models to fitting the colors and spectral energy distributions of a sample of cool white dwarfs to determine their $T_{\rm eff}$, g and He/H composition. One of our main conclusions is that the cool DC stars with $T_{\rm eff} < 5000$ K, previously thought to posses atmospheres highly enriched in helium (He/H $>>$ 1, see Fig. 4), in fact posses hydrogen-rich atmospheres with He/H $\lesssim$ 1.

CHAPTER II

COMPUTATION OF COOL WHITE DWARF ATMOSPHERE MODELS

This dissertation focuses mostly on the input physics of white dwarf atmospheres models; however, we will also calculate models to compare with observations. In this chapter we present how such a calculation is performed. We start with a brief discussion of the basic equations that govern the atmosphere structure and are solved to obtain a model structure and the synthetic spectrum. The transport of energy through the atmosphere is a key physical process that determines its characteristics. In the atmospheres of cool white dwarfs, energy is transported by radiation and convection (Grenfell & Böhm, 1970; Shipman, 1977). We present a description of these two processes. Radiative transfer requires much attention because, in the atmospheres of cool white dwarfs rich in helium, the refractive index deviates significantly from unity (Fig. 7). We have derived original analytical and numerical schemes for the description of radiative transfer in dense, refractive stellar atmospheres (Kowalski & Saumon, 2004). To describe the convective transport we use the standard mixing length theory (Böhm-Vitense, 1958), which we discuss only briefly.

In the last section of this chapter we present the self-consistent solution scheme we developed to solve for the structure of an atmosphere (pressure-temperature profile) with refraction.

2.1 Calculation of an Atmosphere Model

We consider a stellar atmosphere that is static, plane parallel, in local thermal and hydrostatic equilibrium, considering both radiative and convective energy transport. The total flux is constant throughout the atmosphere and scattering of radiation is assumed isotropic. The atmosphere model is calculated for a given $T_{\rm eff}$, g and He/H composition that is assumed to be homogeneous through the atmosphere. The total flux of energy through the atmosphere is specified by $T_{\rm eff}$. The gravity g enters the equation of hydrostatic equilibrium and the composition enters the constitutive physical inputs (equation of state and opacities). Two equations determine the structure of the atmosphere:

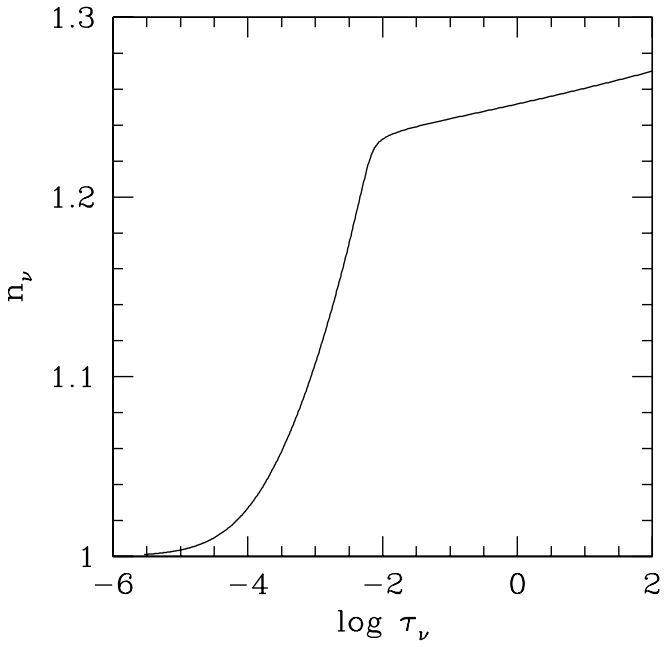

Figure 7: Variation of the index of refraction as a function of vertical optical depth τ_ν for $\lambda = 0.948\,\mu$m in an atmosphere model with $T_{\rm eff} = 4000\,$K, log $g = 8$, and the number abundance ratio He/H $= 10^6$.

the hydrostatic equilibrium equation

$$\frac{dP}{dz} = -\rho g \;\equiv\; \frac{dP}{d\tau_{\rm R}} = \frac{g}{\chi_{\rm R}}, \tag{3}$$

where z is a vertical distance in the atmosphere (Fig. 8), $d\tau_R = \chi_R \rho dz$ is a differential element of vertical optical depth, and χ_R the Rosseland mean extinction coefficient, and the flux conservation equation

$$F(z) = F_{\rm rad}(z) + F_{\rm conv}(z) = \sigma_R T_{\rm eff}^4, \tag{4}$$

where $F_{\rm rad}$ and $F_{\rm conv}$ are the energy fluxes carried by radiation and convection, respectively. Methods for the calculation of these two quantities are presented in the next two sections. Equations (3) and (4) are solved numerically for the $T - P$ profile of the atmosphere with an iterative scheme known

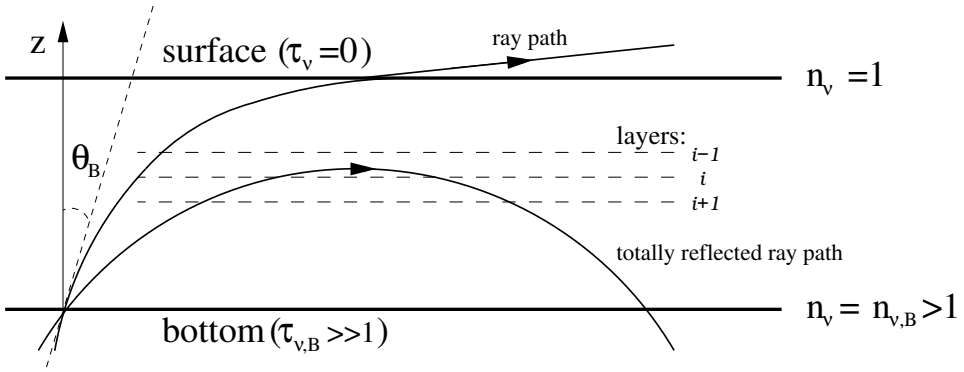

Figure 8: Geometry and typical ray paths for an axially symmetric radiation field in a refractive, planar atmosphere with a monotonically varying refractive index n_ν.

as a "temperature-correction procedure." For the numerical calculations of a model, the atmosphere is divided into layers (Fig 8) and the differential equations are discretized. In the standard case of a non refractive medium, many temperature-correction procedures have been developed, such as the Rybicki solution (Mihalas, 1978). Our temperature-correction procedure for refractive atmospheres is presented at the end of this chapter. The calculation produces a $T - P$ atmospheric profile that uniquely specifies all properties of the fluid and the radiation field throughout the atmosphere. We are particularly interested in the flux distribution that emerges at the surface, the synthetic spectrum, that can be directly compared with observations.

2.2 Radiative Transfer

2.2.1 The Equation of Radiative Transfer in a Dispersive Medium

In this section, we study the transfer of radiation in a stellar atmosphere with refraction. While we are motivated primarily by astrophysical applications, the method developed here is general and can be directly applied to other problems with plane parallel geometry with an arbitrary, monotonic variation of the index of refraction.

We follow the treatment of the theory of radiative transfer in dispersive media presented by (Cox & Giuli, 1968). We assume that the refraction of ray paths follows Snell's law (i.e., geometric optics). For a given run of the index of refraction through the atmosphere, this treatment completely

defines the trajectories of the ray paths and allows the derivation of a simple form of the equation of radiative transfer (ERT) in the presence of dispersive effects. We develop two different numerical schemes to solve the ERT in the presence of refraction, based on the Feautrier and the Λ-iteration methods. Both methods are widely used in stellar atmosphere codes and the procedures we have developed allow for a straightforward implementation of the effects of refraction.

The ERT along an arbitrary ray path is (Cox & Giuli, 1968)

$$\frac{dI_\nu(\vec{r},\vec{q})}{\rho ds} = j_\nu(\vec{r},\vec{q}) - \chi_\nu(\vec{r},\vec{q})I_\nu(\vec{r},\vec{q}) + \left(\frac{dI_\nu(\vec{r},\vec{q})}{\rho ds}\right)_{\rm ref}, \tag{5}$$

where I_ν is the specific intensity at point $\vec{r}$ inside the atmosphere, $\vec{q}$ is the direction of the curved ray path, ρ is the mass density, ds is an element along the curved ray path, j_ν is the total mass emission coefficient, and

$$\chi_\nu = \kappa_\nu + \sigma_\nu \tag{6}$$

is the total mass absorption coefficient, the sum of true absorption (κ_ν) and scattering (σ_ν) processes. The mass emission and absorption coefficients are related to their non dispersive values j^0_ν, χ^0_ν by $j_\nu = n_\nu j^0_\nu$, and $\chi_\nu = \chi^0_\nu/n_\nu$, respectively (Harris, 1965). The last term on the r.h.s. of Eq. (5) includes the contribution to $dI_\nu/\rho ds$ coming from spatial variations of the refractive index. In a horizontally homogeneous medium, the geometry leads to an axially symmetric radiation field. In the presence of refraction, the ray path is defined by Snell's law as

$$n_\nu \sin(\theta) = n'_\nu \sin(\theta') = \text{constant} \tag{7}$$

and

$$\phi = \phi' \pm \pi, \tag{8}$$

where θ and ϕ are the polar angles coordinates with respect to the vertical z axis, parallel to the direction of the gradient of n_ν. Applying the law of energy conservation to an incident beam of radiation with solid angle $d\omega$, propagating from a medium with refractive index n_ν into a medium

with refractive index n'_ν, and refracted into $d\omega'$ we get

$$I_\nu \cos(\theta) d\omega = I'_\nu \cos(\theta') d\omega', \tag{9}$$

and we find that I_ν / n_ν^2 is constant along a ray path if there are no energy losses or gains due to emission, absorption, or interface effects (Cox & Giuli, 1968). On the basis of that assumption, the last term in Eq. (5) is

$$\left(\frac{dI_\nu}{ds} \right)_{\text{ref}} = \frac{\partial I_\nu}{\partial n_\nu} \frac{dn_\nu}{ds} = \frac{2 I_\nu}{n_\nu} \frac{dn_\nu}{ds} \tag{10}$$

and the ERT becomes

$$\frac{d}{\rho ds} \left(\frac{I_\nu(\vec{r}, \vec{q})}{n_\nu^2} \right) = \frac{j_\nu(\vec{r}, \vec{q}) - \chi_\nu(\vec{r}, \vec{q}) I_\nu(\vec{r}, \vec{q})}{n_\nu^2}. \tag{11}$$

In plane-parallel geometry, the derivative d/ds takes the form

$$\frac{d}{ds} = \cos\theta \frac{\partial}{\partial z} + \frac{d\theta}{ds} \frac{\partial}{\partial \theta}. \tag{12}$$

The derivative over θ appears because the ray paths are curved. For a given ray path, however, Eq. (7) allows us to reduce the configuration space from $\{z, \theta\}$ to a one-dimensional curve in $\{z\}$ only. The ray paths are parameterized by θ_B, the value of the ray path angle at a reference level chosen to be the bottom of the atmosphere (Fig. 8). Hereafter, all quantities with subscript "B" refer to this lower boundary. A ray path is described by

$$\mu_B = \cos\theta_B = \text{constant} \tag{13}$$

and as for each one dimensional curve $dz/ds = \cos\theta$, we can write

$$\frac{d}{ds} = \cos\theta \frac{\partial}{\partial z} \tag{14}$$

and rewrite the ERT (11) in a simpler form

$$\frac{\partial I'_\nu(\tau_\nu,\mu_B)}{\partial \sigma_\nu} = I'_\nu(\tau_\nu,\mu_B) - S'_\nu(\tau_\nu) \tag{15}$$

or

$$\mu(\mu_B, n(\tau_\nu))\frac{\partial I'_\nu(\tau_\nu,\mu_B)}{\partial \tau_\nu} = I'_\nu(\tau_\nu,\mu_B) - S'_\nu(\tau_\nu), \tag{16}$$

where a primed quantity f' represents f/n_ν^2, $S_\nu = j_\nu/\chi_\nu$ is the source function, σ_ν is now the optical depth measured along the curved ray path, τ_ν is the vertical optical depth, and

$$\mu = \mathrm{sign}(\mu_B)\sqrt{1-\left(\frac{n_{\nu,B}}{n_\nu}\right)^2(1-\mu_B^2)}. \tag{17}$$

The optical depths σ_ν and τ_ν are related to physical distances through the relations: $d\tau_\nu = -\rho\chi_\nu dz$ and $d\sigma_\nu = -\rho\chi_\nu ds$.

Equation (16) reduces to the well-known expression for the ERT for a non refractive, plane-parallel atmosphere, if we set $\mu =$ constant and $n_\nu = 1$. In the refractive case, however, the angle μ is now a function of μ_B and τ_ν, and, at any given level, only the rays that started at the bottom with μ_B given by

$$\mu_{B\min}^2(\tau_\nu) = 1-\left(\frac{n_\nu(\tau_\nu)}{n_{\nu,B}}\right)^2 < \mu_B^2 < 1. \tag{18}$$

will not have been reflected downward. We label the set of all possible values of μ_B at a given τ_ν by ζ.

While Eqs. (15) and (16) are mathematically equivalent forms of the ERT, their numerical solution with finite difference schemes have very different accuracies for strongly curved ray paths. Equation (16) is simpler to solve numerically, as it does not require the calculation of σ_ν, however, we find that it is essential to integrate the optical depth along the curved ray path to obtain a good solution and we will use the form given by Eq. (15).

2.2.2 Moments of the Radiation Field

The moments of the radiation field $J_\nu(\tau_\nu)$, $H_\nu(\tau_\nu)$, and $K_\nu(\tau_\nu)$ are defined as

$$J_\nu(\tau_\nu) = \frac{1}{2}\int_{-1}^{1} I_\nu(\tau_\nu, \mu)\, d\mu, \tag{19}$$

$$H_\nu(\tau_\nu) = \frac{1}{2}\int_{-1}^{1} \mu I_\nu(\tau_\nu, \mu)\, d\mu, \tag{20}$$

and

$$K_\nu(\tau_\nu) = \frac{1}{2}\int_{-1}^{1} \mu^2 I_\nu(\tau_\nu, \mu)\, d\mu. \tag{21}$$

The radiative flux that enters the Eq. (4) is given by

$$F_{\rm rad}(z) = \int_0^\infty F_\nu(\tau_\nu(z))d\nu, \tag{22}$$

where $F_\nu(\tau_\nu) = 4\pi H_\nu(\tau_\nu)$. F_ν is the flux, H_ν is known as the Eddington flux and J_ν is the mean intensity.

The ERT for the non refractive case can be rewritten in terms of these moments, so that

$$\frac{\partial H_\nu(\tau_\nu)}{\partial \tau_\nu} = J_\nu(\tau_\nu) - S_\nu(\tau_\nu), \tag{23}$$

$$\frac{\partial K_\nu(\tau_\nu)}{\partial \tau_\nu} = H_\nu(\tau_\nu), \tag{24}$$

and

$$\frac{\partial^2 K_\nu(\tau_\nu)}{\partial \tau_\nu^2} = J_\nu(\tau_\nu) - S_\nu(\tau_\nu). \tag{25}$$

For the more general refractive case, the moments of the radiation field become

$$J'_\nu(\tau_\nu) = \frac{1}{2}\int_{-1}^{1} I'_\nu(\tau_\nu, \mu)\, d\mu = \frac{1}{2}\int_{\zeta(\tau_\nu)} I'_\nu(\tau_\nu, \mu_B)\frac{\partial \mu}{\partial \mu_B}\, d\mu_B, \tag{26}$$

$$H'_\nu(\tau_\nu) = \frac{1}{2}\int_{-1}^{1} \mu I'_\nu(\tau_\nu,\mu)\, d\mu = \frac{1}{2}\int_{\zeta(\tau_\nu)} \mu(\mu_B) I'_\nu(\tau_\nu,\mu_B)\frac{\partial\mu}{\partial\mu_B}\, d\mu_B, \tag{27}$$

and

$$K'_\nu(\tau_\nu) = \frac{1}{2}\int_{-1}^{1} \mu^2 I'_\nu(\tau_\nu,\mu)\, d\mu = \frac{1}{2}\int_{\zeta(\tau_\nu)} \mu^2(\mu_B) I'_\nu(\tau_\nu,\mu_B)\frac{\partial\mu}{\partial\mu_B}\, d\mu_B, \tag{28}$$

where

$$\frac{\partial\mu}{\partial\mu_B} = \frac{\eta(\tau_\nu)}{\mu}, \tag{29}$$

and

$$\eta(\tau_\nu) = \mu_B \left(\frac{n_{v,B}}{n_\nu}\right)^2. \tag{30}$$

In the refractive case, J'_ν, H'_ν, and K'_ν are more convenient quantities than J_ν, H_ν and K_ν because I'_ν is constant along a ray path. The construction of the moments Eqs. (23)–(25) is complicated by the fact that μ and the integration domain ζ are now functions of τ_ν. We first consider the derivative of H'_ν over τ_ν. For μ and η given by Eqs. (17) and (30) we get

$$\frac{\partial\eta}{\partial\tau_\nu} = -2\eta\frac{1}{n_\nu}\frac{\partial n_\nu}{\partial\tau_\nu} \tag{31}$$

and

$$\frac{\partial\mu}{\partial\tau_\nu} = -\frac{1-\mu^2}{\mu}\frac{1}{n_\nu}\frac{\partial n_\nu}{\partial\tau_\nu}. \tag{32}$$

Taking the derivative of Eq. (27) over τ_ν, we obtain

$$\begin{aligned}\frac{\partial H'_\nu}{\partial\tau_\nu} &= \frac{1}{2}\frac{\partial}{\partial\tau_\nu}\int_\zeta \eta I'_\nu\, d\mu_B = \frac{1}{2}\int_\zeta \frac{\partial}{\partial\tau_\nu}\left(\eta I'_\nu\right)\, d\mu_B \\ &\quad -\frac{\partial\mu_{B\min}}{\partial\tau_\nu}\eta I'_\nu\Big|_{\mu_B=\mu_{B\min}} + \frac{\partial(-\mu_{B\min})}{\partial\tau_\nu}\eta I'_\nu\Big|_{\mu_B=-\mu_{B\min}}.\end{aligned} \tag{33}$$

Because $I'_\nu(\mu_{B\min}) = I'_\nu(-\mu_{B\min})$ and $\eta(\mu_{B\min}) = -\eta(-\mu_{B\min})$, we get

$$\frac{\partial H'_\nu}{\partial\tau_\nu} = \frac{1}{2}\int_\zeta \frac{\partial}{\partial\tau_\nu}(\eta I'_\nu)\, d\mu_B$$

$$= \frac{1}{2}\int_\zeta \frac{\partial\eta}{\partial\tau_\nu}(I'_\nu)\,d\mu_B + \frac{1}{2}\int_\zeta \eta\mu^{-1}(I'_\nu - S'_\nu)\,d\mu_B$$
$$= J'_\nu - S'_\nu - 2H'_\nu\frac{1}{n_\nu}\frac{\partial n_\nu}{\partial\tau_\nu}, \tag{34}$$

and finally

$$\frac{\partial H_\nu(\tau_\nu)}{\partial\tau_\nu} = J_\nu(\tau_\nu) - S_\nu(\tau_\nu), \tag{35}$$

which is identical to Eq. (23). The condition for radiative equilibrium that expresses the flux conservation in the radiative zone

$$\frac{\partial F_{\rm rad}(z)}{\partial z} = 4\pi\frac{\partial}{\partial z}\int_0^\infty H_\nu\,d\nu = 4\pi\int_0^\infty \chi_\nu(J_\nu - S_\nu)\,d\nu = 0 \tag{36}$$

remains unchanged. An analogous derivation for $\partial K'_\nu/\partial\tau_\nu$ gives

$$\frac{\partial K'_\nu}{\partial\tau_\nu} = H'_\nu(\tau_\nu) + \frac{1}{2}\int_\zeta \frac{\partial(\mu\eta)}{\partial\tau_\nu}I'_\nu\,d\mu_B - \frac{1}{2}\int_\zeta \eta S'_\nu\,d\mu_B. \tag{37}$$

Because η is antisymmetric in μ_B, the last term in Eq. (37) is 0 and we finally get

$$\frac{\partial K'_\nu}{\partial\tau_\nu} = H'_\nu(\tau_\nu) - (3K'_\nu - J'_\nu)\frac{1}{n_\nu}\frac{\partial n_\nu}{\partial\tau_\nu} \tag{38}$$

or

$$\frac{\partial K_\nu}{\partial\tau_\nu} = H_\nu(\tau_\nu) - (K_\nu - J_\nu)\frac{1}{n_\nu}\frac{\partial n_\nu}{\partial\tau_\nu}. \tag{39}$$

Equation (39) contains an additional term due to refraction. In cool white dwarf atmospheres, this term can dominate near the surface, as the gradient of the index of refraction becomes very large (Fig. 7). This equation may be used to evaluate the Eddington flux H_ν when J_ν, K_ν, and n_ν are known. The form of Eq. (25) that includes refraction contains a term in $\partial J_\nu/\partial\tau_\nu$ and is not useful.

2.2.3 Solution of the Equation of Radiative Transfer in a Dispersive Medium

Feautrier Solution

In the presence of refraction, it remains advantageous to define the symmetric average of the specific intensity

$$P'(\mu_B, v, \sigma_\nu) = \frac{1}{2}[I'(\mu_B, \nu, \sigma_\nu) + I'(-\mu_B, \nu, \sigma_\nu)]. \tag{40}$$

Differentiating with respect to σ_ν, we obtain

$$\frac{\partial P'(\mu_B, \nu, \sigma_\nu)}{\partial \sigma_\nu} = \frac{1}{2}[I'(\mu_B, \nu, \sigma_\nu) - I'(-\mu_B, v, \sigma_\nu)] \tag{41}$$

and

$$\frac{\partial^2 P'(\mu_B, \nu, \sigma_\nu)}{\partial \sigma_\nu^2} = P'(\mu_B, \nu, \sigma_\nu) - S'(\sigma_\nu). \tag{42}$$

The source function in a dispersive medium and under the assumption of local thermal equilibrium (LTE) and isotropic scattering is (Cox & Giuli, 1968)

$$S'_\nu(\tau_\nu) = \epsilon_\nu B_\nu + (1 - \epsilon_\nu) J'_\nu, \tag{43}$$

where $\epsilon_\nu = \kappa_\nu / \chi_\nu$ is an absorption coefficient (equivalently, $1 - \epsilon_\nu$ is the scattering coefficient, or albedo). Equations (40)–(42) are mathematically identical to those used in the non refractive case (Mihalas, 1978), and their solution will require only minor changes.

Two boundary conditions are required to solve the second-order differential Eq. (42). At the bottom of the atmosphere, where $\tau_\nu >> 1$, the radiation field is very close to thermodynamic equilibrium and

$$P'_B = B_\nu, \tag{44}$$

where B_ν is the Planck function. To ease the notation, we drop the subscript ν in the remainder of our discussion of the solution of the ERT.

We consider that there is no incident radiation on the top of the atmosphere ($\tau_\nu = 0$). For ray paths that exit at the surface ($\mu_B > \mu_{B\min}(0)$), the surface boundary condition is obtained from

Eqs. (40) and (41):

$$\left.\frac{\partial P'}{\partial \sigma}\right|_{\sigma_{\rm surface}} = P'_0. \tag{45}$$

Because of refraction, rays with $\mu_B < \mu_{B\min}(0)$ are reflected downward (Fig. 8). These ray paths require a different boundary condition. At the reflection point, $\mu = 0$, $I'(+\mu) = I'(-\mu)$, and we have (Eq. 41)

$$\left.\frac{\partial P'}{\partial \sigma}\right|_{\sigma_{\rm reflection\ point}} = 0. \tag{46}$$

We solve the equations in finite difference form, where the vertical structure of the atmosphere is divided in $i = 1, 2, \ldots, N$ horizontal layers with $i = 1$ corresponding to the topmost layer. We develop higher-order expressions for the boundary conditions using Taylor expansions

$$P'_{i+1} = P'_i + \left.\frac{\partial P'}{\partial \sigma}\right|_{\sigma_i} \Delta\sigma_{i+1} + \frac{1}{2}(P'_i - S'_i)\Delta\sigma^2_{i+1} \tag{47}$$

and

$$\left.\frac{\partial P'}{\partial \sigma}\right|_{\sigma_{\rm top}} = \left.\frac{\partial P'}{\partial \sigma}\right|_{\sigma_i} + (P'_i - S'_i)(\sigma_{\rm top} - \sigma_i), \tag{48}$$

where $\Delta\sigma_i = \sigma_i - \sigma_{i-1}$ and $\sigma_{\rm top}$ is the optical depth at the boundary (either the surface or the reflection point) measured along the ray path. For the surface boundary condition we get

$$\frac{P'_2 - P'_1}{\Delta\sigma_2} = P'_1 + \frac{1}{2}(P'_1 - S'_1)(\sigma_1 + \sigma_2 - 2\sigma_{\rm top}). \tag{49}$$

and for the boundary condition for ray paths that are totally reflected between levels τ_R and τ_{R-1}

$$\frac{P'_{R+1} - P'_R}{\Delta\sigma_{R+1}} = \frac{1}{2}(P'_R - S'_R)(\sigma_R + \sigma_{R+1} - 2\sigma_{\rm top}). \tag{50}$$

Equations (42), (44), (49), and (50) are solved by modifying the Feautrier solution (Mihalas, 1978). The derivatives of any physical quantity f with respect to σ are evaluated with finite differences

$$\left(\frac{df}{d\sigma}\right)_{i-\frac{1}{2}} = \frac{f_i - f_{i-1}}{\sigma_i - \sigma_{i-1}}, \tag{51}$$

and for the second derivative

$$\left(\frac{d^2f}{d\sigma^2}\right)_i = \frac{\left(\frac{df}{d\sigma}\right)_{i+\frac{1}{2}} - \left(\frac{df}{d\sigma}\right)_{i-\frac{1}{2}}}{\frac{1}{2}(\sigma_{i+1} - \sigma_{i-1})}. \tag{52}$$

The ERT is solved on a discrete grid of μ_B points, that defines the ray paths. Each ray path is labeled $\mu_{B,k}$, where $k = 1, ..., D$. The set of radiative transfer Eqs. (42), can then be written as an algebraic matrix equation (Mihalas, 1978)

$$-\mathbf{A}_i\mathbf{P}'_{i-1} + \mathbf{B}_i\mathbf{P}'_i - \mathbf{C}_i\mathbf{P}'_{i+1} = \mathbf{L}_i, \tag{53}$$

where $\mathbf{A}_i$, $\mathbf{C}_i$, and $\mathbf{L}_i$ are $D \times 1$ vectors corresponding to layer i, with row $\{\mathbf{A}_i\}_j$,$\{\mathbf{C}_i\}_j$,$\{\mathbf{L}_i\}_j$ corresponding to ray path j, and $\mathbf{B}_i$ is a $D \times D$ matrix, corresponding to layer i with elements $\{\mathbf{B}_i\}_{j,k=1,...,D}$ corresponding to ray path j. The surface and bottom boundary conditions are constructed from Eqs. (49) and (44).

In the presence of refraction we need to consider the treatment of totally reflected ray paths. According to Eq. (50), for ray path j reflected between layers R and $R-1$, the boundary condition for reflected rays can be written as

$$\sum_k \{\mathbf{B}_R\}_{j,k}\{\mathbf{P}'_R\}_k - \{\mathbf{C}_R\}_j\{\mathbf{P}'_{R+1}\}_j = \{\mathbf{L}_R\}_j. \tag{54}$$

Furthermore, the number of rays in a given layer decreases toward the top of the atmosphere. To maintain the dimensions of $\mathbf{B}_i$, the elements corresponding to reflected ray paths are treated differently. For angles $\mu_{B,j} < \mu_{B\min}(\tau_i)$, i.e., for ray paths reflected deeper than τ_i, we set

$$\{\mathbf{B_i}\}_{j,k} = \begin{cases} 0, & \text{for } j \neq k \\ 1, & \text{for } j = k \end{cases} \tag{55}$$

and

$$\{\mathbf{A_i}\}_j = \{\mathbf{C_i}\}_j = \{\mathbf{L_i}\}_j = 0. \tag{56}$$

The solution of Eq. (42) for $P'(\tau_\nu, \mu_B)$ is otherwise identical to the non refractive case (Mihalas, 1978):

$$\begin{aligned}
\mathbf{P}'_i &= \mathbf{D}_i \mathbf{P}'_{i+1} + \mathbf{v}_i \\
\mathbf{D}_i &= (\mathbf{B}_i - \mathbf{A}_i \mathbf{B}_{i-1})^{-\mathbf{1}} \mathbf{C}_i \\
\mathbf{v}_i &= (\mathbf{B}_i - \mathbf{A}_i \mathbf{B}_{i-1})^{-\mathbf{1}} (\mathbf{L}_i + \mathbf{A}_i \mathbf{v}_{i-1}) \\
\mathbf{D}_1 &= \mathbf{B}_1^{-\mathbf{1}} \mathbf{C}_1 \\
\mathbf{v}_1 &= \mathbf{B}_1^{-\mathbf{1}} \mathbf{L}_1,
\end{aligned} \tag{57}$$

and the moments of the radiation field are then obtained with

$$J'_\nu(\tau_\nu) = \frac{1}{2} \int_0^1 P'_\nu(\tau_\nu, \mu_B)\, d\mu, \tag{58}$$

$$H'_\nu(\tau_\nu) = \frac{1}{2} \int_0^1 \mu^2 \frac{\partial P'_\nu(\tau_\nu, \mu_B)}{\partial \tau_\nu}\, d\mu = \frac{1}{2} \int_0^1 \mu \frac{\partial P'_\nu(\sigma_\nu, \mu_B)}{\partial \sigma_\nu}\, d\mu, \tag{59}$$

and

$$K'_\nu(\tau_\nu) = \frac{1}{2} \int_0^1 \mu^2 P'_\nu(\tau_\nu, \mu_B)\, d\mu. \tag{60}$$

Λ-iteration method

Given the formal solution of the ERT along a ray path between optical depths $\sigma_{\nu,1}$ and $\sigma_{\nu,2}$ $(\sigma_{\nu,1} < \sigma_{\nu,2})$

$$I'_\nu(\sigma_{\nu,1}) = I'_\nu(\sigma_{\nu,2}) e^{-(\sigma_{\nu,2} - \sigma_{\nu,1})} + \int_{\sigma_{\nu,1}}^{\sigma_{\nu,2}} S'_\nu(t) e^{-(t - \sigma_{\nu,1})}\, dt, \tag{61}$$

the mean intensity (26) is given by

$$J'_\nu(\tau_\nu) = \frac{1}{2} \int_{-1}^{1} I'_\nu(\sigma_\nu(\tau_\nu))\, d\mu = \Lambda[S'_\nu(t)], \tag{62}$$

where Λ is an operator that acts on the source function S'_ν. The source function (43) is

$$S'_\nu(\tau_\nu) = \epsilon_\nu B_\nu + (1-\epsilon_\nu)\Lambda[S'_\nu(t)]. \tag{63}$$

An iterative method can be used to find the value of the source function S'_ν at a given atmosphere level

$$S'_{l+1} = \epsilon_\nu B_\nu + (1-\epsilon_\nu)\Lambda S'_l. \tag{64}$$

This solution is known as the Λ-iteration method (Mihalas, 1978). For a discrete grid of τ_ν points, Λ may also be represented as a matrix operator $\mathbf{\Lambda}$ that acts on the source function vector $\mathbf{S}'$ (Olson & Kunasz, 1987)

$$\mathbf{J}' = \mathbf{\Lambda}\mathbf{S}'. \tag{65}$$

The elements of the matrix $\mathbf{\Lambda}$ depend only on the numerical scheme adopted for integrating over σ_ν and μ to evaluate the specific intensity I'_ν, and the mean intensity J'_ν, respectively. A good choice is to locally interpolate the source function by a quadratic expression in σ_ν, which allows for analytic integration in Eq. (61) and excellent numerical precision. In this case the construction of the $\mathbf{\Lambda}$ matrix is well-known and presented in details by Olson & Kunasz (1987). Once the source function S'_ν is obtained by solving Eq. (64), I'_ν is computed from Eq. (61), and the moments J'_ν, H'_ν and K'_ν follow by direct integration. For the Λ-iteration procedure, the boundary conditions are physically the same as in the non refractive case: 1) $I'_\nu = B_\nu$ at the bottom of the atmosphere and 2) there is no incident radiation at the surface $I'_\nu(\mu < 0) = 0$. There is no need for a "surface" boundary condition for the totally reflected ray paths. Because the Λ-iteration method solves directly for I'_ν, we can integrate along the full length of the reflected ray path (Eq. 61), including the downward part.

We found that the Λ-iteration method works very well for cool white dwarf atmospheres. However, it is well known that the Λ-iteration method converges poorly for nearly pure scattering media ($\epsilon_\nu << 1$) (Mihalas, 1978). This difficulty can be circumvented with the accelerated Λ-iteration

methods (ALI) (Cannon, 1973; Olson et al., 1986; Hauschildt, 1992; Hauschildt et al., 1993). Because the introduction of refraction does not affect the Λ-iteration method proper, the solution can be implemented just as easily with ALI as with the Λ-iteration.

2.2.4 Application to Stellar Atmospheres

Numerical Considerations

As is usual, the atmosphere is divided vertically into discrete layers, $\tau_{\nu,i}$ (Fig. 8) and the ERT is solved for a finite set of ray paths $\mu_{B,k}$. Because in the refractive case the rays are no longer straight, the optical depth along the ray path σ_ν must be obtained by integration and it is related to the vertical optical depth τ_ν by

$$\sigma_\nu(\tau_\nu) = \int_{\tau_{0,\nu}}^{\tau_\nu} \frac{d\tau'_\nu}{\mu(\tau'_\nu)}, \tag{66}$$

where $\tau_{0,\nu}$ is the optical depth at the bottom of the atmosphere for upward rays and $\tau_{0,\nu} = 0$ for downward rays that start from the surface. We found that it is essential to calculate σ_ν precisely along the curved ray paths. This calculation is especially important in the layer where a given ray path is internally reflected. This is where the curvature of the ray is maximal and the ray can travel over a large horizontal distance (in optical depth) within that layer (Fig. 8). We locally interpolate $\mu(\tau_\nu)$ between τ_ν grid points with a quadratic polynomial to evaluate σ_ν analytically. To find the vertical optical depth τ_ν of the reflection point ($\mu(\tau_\nu) = 0$), we use Eq. (17) and a quadratic interpolation of $n_\nu(\tau_\nu)$. The integrals for the moments of the radiation field are performed numerically with a quadratic (3-point) integration scheme. The integration consists of two parts, $0 \leq \mu \leq \mu_c$ and $\mu_c \leq \mu \leq 1$, because $P'_\nu(\tau_\nu, \mu)$ is discontinuous at $\mu = \mu_c(\tau_\nu) = \sqrt{1 - n_\nu^2(\tau_\nu = 0)/n_\nu^2(\tau_\nu)}$. Rays with $\mu < \mu_c(\tau_\nu)$ will be reflected before they reach the surface. In Eq. (61), $S'_\nu(\tau_\nu)$ is approximated by a quadratic polynomial in each layer (Olson & Kunasz, 1987). The radiative flux from the Feautrier solution is calculated with both Eqs. (59) and (39) to check the numerical consistency of the solution.

We have verified that our methods of solutions and codes are correct in two ways. To check the consistency of the solutions obtained with the Feautrier and Λ-iteration methods, and their

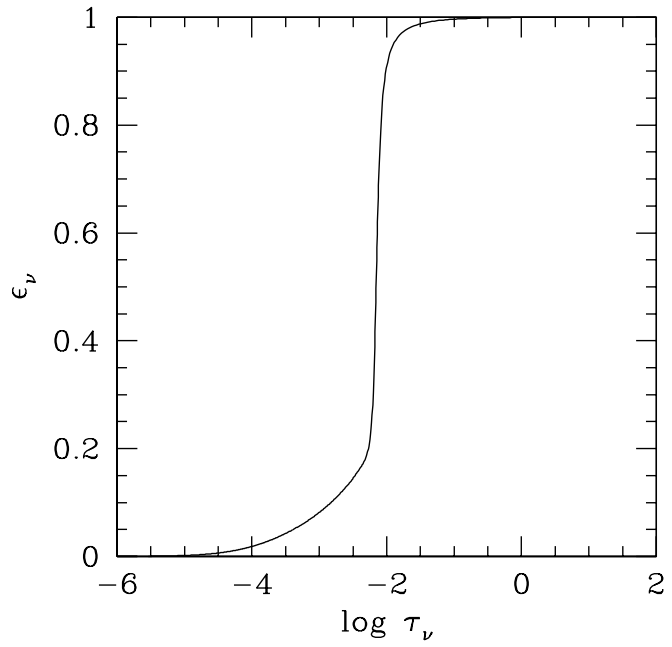

Figure 9: Absorption parameter $\epsilon_\nu = \kappa_\nu/\chi_\nu$ in the atmosphere model with $T_{\rm eff} = 4000\,{\rm K}$, $\log g = 8$, and ${\rm He/H} = 10^6$ for $\lambda = 0.948\,\mu{\rm m}$. Pure scattering corresponds to $\epsilon_\nu = 0$.

sensitivity to the resolution of the τ_ν and μ_B grids, we solved for the radiation field in a white dwarf atmosphere with a fixed (T, P) structure for a helium-rich model with $T_{\rm eff} = 4000\,{\rm K}$, $\log g = 8$, and ${\rm He/H}) = 10^6$ in radiative/convective equilibrium. In this model the convection zone extends from the bottom of the atmosphere up to $\tau_R \sim 10^{-2}$. The inputs for computing the radiation field are the refractive index $n_\nu(\tau_\nu)$ (Fig. 7 and Appendix A), the absorption parameter $\epsilon_\nu(\tau_\nu)$ (Fig 9), and the Planck function $B_\nu(\tau_\nu)$, all computed from the (T, P) structure.

For our most precise calculation, using $N = 500$ layers and $D = 500$ ray-paths, the relative differences between the two methods are smaller than 0.1% in both J_ν and H_ν, and the internal precision of both methods is better than 0.01%. The difference between the two solutions decreases significantly as the number of layers increases. With 50 layers, the moments of the radiation field can differ by as much as 1%. On the other hand, the solution is much less sensitive to the number of ray paths. In situations where the optical thickness of a layer $\tau_{\nu,i+1} - \tau_{\nu,i} \gtrsim 1$, as is common in

the deeper region of atmosphere models, the application of a quadratic interpolation of the source function S'_ν in Eq. (61) is more precise than the solution of Eq. (42) using a finite difference scheme. The Λ-iteration method is therefore a better choice when computing a model with a relatively small number of layers ($N \sim 50$).

When computing white dwarf atmosphere models, we use 50 layers from $10^{-6} < \tau_R < 10^2$ and 30 μ-angle points with the Feautrier solution. In some cases where convergence of the model is difficult, we switch to the Λ-iteration method. The frequency integral in the radiative equilibrium Eq. (36) is performed with 180 ν-points covering $0.15 < \lambda < 100\,\mu$m. Our models account for the following opacity sources: H bf and ff, H^- bf and ff, H_2^+ bf and ff, H_2^- ff, H_2 CIA (collisions with H_2, H and He), He_2^+ bff, He^- ff, He ff, Rayleigh scattering by H, H_2 and He, and the red wing of the H Ly α line (chapter VII). Cool white dwarfs do not show lines of He and the Balmer lines of H are very weak for $T_{\rm eff} < 6000\,$K. Except for Ly α (Chapter VII), line transitions are not modeled.

We have also compared with published solutions to a similar but simpler problem, where radiative transfer with refraction is considered in a dielectric slab (Abdallah & Dez, 2000; Huang et al., 2003). Both surfaces of the slab are maintained at fixed but different temperatures, radiative equilibrium is imposed, the index of refraction varies linearly between the two surfaces, and the absorption coefficient is constant. We note that Abdallah & Dez (2000) neglected the effect of dispersion on the absorption coefficient, assuming that $\kappa_\nu = \kappa^0_\nu$, whereas the correct expression is $\kappa_\nu = \kappa^0_\nu / n_\nu$, where κ^0_ν is the mass absorption coefficient in the absence of dispersive effects (Harris, 1965). Setting $\kappa_\nu = \kappa^0_\nu$, we reproduce Figs. (3a–3c) of Abdallah & Dez (2000) perfectly. Introducing the effect of dispersion on κ_ν raises the temperature profile in the slab by a few degrees.

2.3 Convection

The deeper layers of all cool white dwarf atmospheres are convectively unstable. The convection zone extends into the optically thin part of the atmosphere, typically to $\tau_R \lesssim 10^{-2}$. The convective flux in our models is estimated with the mixing-length theory, which we summarize here for completeness, following Mihalas (1978). The presence of convective instability is established with

Schwarzschild's criterion

$$\nabla_R > \nabla_A, \tag{67}$$

where $\nabla = d\ln T/d\ln P$ denotes the temperature gradient. The radiative gradient ∇_R is the temperature gradient that would occur if the entire stellar flux were carried by radiation

$$\nabla_R = \frac{3\pi F \chi_{\rm R} P}{16\sigma_R g \rho T^4}, \tag{68}$$

where $F = \sigma_R T_{\rm eff}^4$ is the total flux. The adiabatic gradient ∇_A is the temperature gradient of an element of gas or fluid displaced adiabatically (i.e., without heat transfer with the surrounding medium)

$$\nabla_A = \left.\frac{\partial \ln T}{\partial \ln P}\right|_S \tag{69}$$

and is a thermodynamic property of the fluid.

The convective flux is

$$F_{\rm conv} = \left(\frac{gQH}{32\pi^2}\right)^{1/2} (\rho C_p T) \left(\nabla - \nabla'\right)^{3/2} \left(\frac{l}{H}\right)^2 = \alpha \left(\nabla - \nabla'\right)^{3/2}, \tag{70}$$

where ∇ is the actual temperature gradient in the atmosphere and ∇' is the temperature gradient in the convective elements. The latter is given by

$$\left(\nabla - \nabla'\right)^{1/2} = -\frac{B}{2} + \frac{1}{2}\left(B^2 + 4\left(\nabla - \nabla_A\right)\right)^{1/2}, \tag{71}$$

where

$$B = \frac{16\sqrt{2}\sigma_R T^3 \tau_e}{\rho C_p (gQH)^{1/2} (l/H)(1 + \frac{1}{3}\tau_e^2)} \tag{72}$$

and

$$Q = -\left.\frac{\partial \ln \rho}{\partial \ln T}\right|_P. \tag{73}$$

C_p is the molar specific heat at constant pressure and $H = P/(g\rho)$ is the pressure scale height. l is the mixing length, the distance traveled by a convective element, and usually chosen to be some

multiple of H (we choose $l = H$). τ_e denotes the optical thickness of the characteristic element of size l, $\tau_e = \chi_R \rho l$. In cool white dwarf atmospheres, the convective flux is not sensitive to the choice for l, as the gradient ∇ is extremely close to the adiabatic gradient ∇_A (Bergeron et al., 1997).

2.4 Numerical Solution for the Atmosphere Model

To obtain the atmosphere model for given $T_{\rm eff}$, g and He/H composition, we have to solve simultaneously the hydrostatic equilibrium equation (Eq. 3) and the total flux conservation equation (Eq. 4). The flux conservation equation in the radiative zone is expressed by the radiative equilibrium equation (Eq. 36). Starting with an approximate input $T - P$ structure, an iterative method is used to converge to a consistent solution of the equations.

For a non refractive medium, the linearization method of Rybicki (1971) is very powerful and was originally implemented in the white dwarf atmosphere code we use (Bergeron et al., 1991). In a refractive atmosphere, the Rybicki solution is no longer applicable, because Eq. (24) now assumes a complicated form (Eq. 39). We constructed a new temperature correction scheme for calculating the $T - P$ profile.

In our approach we keep the pressure constant in each layer during the iteration procedure. With an initial input $P - T$ profile, we first calculate the chemical abundances of all species, the thermodynamics and the opacities in each layer. The equation of state model, which provides the thermodynamics of the fluid and the chemical abundances required for the opacity calculation, includes the following species: H, H_2, H^+, H^-, H_2^+, H_3^+, He, He^+, He_2^+, HeH^+ and e. Most of these species have very low abundances but are nonetheless important sources of opacity. Interactions among the most important species (H, H_2, He), which cause departures from ideal gas thermodynamics are also accounted for (Chapters III, V and VI).

We solve the radiative transfer equation (5) with the Feautrier solution (§2.2.3) for the moments of radiation field, including $F_{\rm rad}$. We compute the convective flux, $F_{\rm conv}$ (Eq. 70) in each layer where the Schwarzschild criterion indicates convective instability (Eq. 67).

In the next step we iterate a new temperature profile, that satisfies the radiative equilibrium equation (Eq. 36) in the radiative zone. The temperature correction in a radiative layer i at step k

is given by

$$T_i^{k+1} = T_i^k + \Delta T_i^k, \tag{74}$$

where

$$\Delta T_i^{k+1} = L_i^k \left(\frac{\partial L_i^k}{\partial T_i^k} \right)^{-1} \tag{75}$$

$$L_i^k = \int_0^\infty \chi_{i,\nu}^k (J_{i,\nu}^k - S_{i,\nu}^k) d\nu \tag{76}$$

This is a simple Newton-Raphson method to achieve radiative equilibrium. In the convective zone,

$$\Delta T^{k+1} = T_i^k \left(\left(\frac{F_{tot}}{F_{i=1,rad}^k} \right)^{1/4} - 1 \right). \tag{77}$$

The temperature correction in the convection zone (Eq. 77) is temporary and only ensures that radiative equilibrium is obtained with the correct value of $F_{\rm rad} = \sigma_R T_{\rm eff}^4$. This step is necessary because the equation for radiative equilibrium (Eq. 36) only guarantees constancy of the flux through the radiative zone, but not its correct value which in these models is determined in the convection zone where the photosphere is found. In each iteration step we recalculate the chemistry, $\chi_{i,\nu}$, and the radiative transfer equation (Eq. 5) for new $J_{i,\nu}^k(T)$, $S_{i,\nu}^k(T)$ and $F_{i,\rm rad}^k(T)$. This procedure is run until $\Delta T_i/T_i < 10^{-5}$ in each layer.

In the next step, we correct the temperature in the convection zone to satisfy the total flux conservation equation (Eq. 4) in the following way

$$T_i = T_{i-1} \frac{(P_i + P_{i-1}) + (P_i + P_{i-1})\nabla_i}{(P_i + P_{i-1}) - (P_i + P_{i-1})\nabla_i}, \tag{78}$$

where the temperature gradient ∇_i in layer i is estimated from

$$\nabla_i = \left(\left(\frac{F - F_{i-\frac{1}{2},\rm rad}}{\alpha_{i-\frac{1}{2}}} \right)^{\frac{1}{3}} + \frac{B_{i-\frac{1}{2}}}{2} \right)^2 - \frac{B_{i-\frac{1}{2}}^2}{4} + \nabla_{i,A}, \tag{79}$$

and for any quantity f, we define $f_{i-\frac{1}{2}} = (f_i + f_{i-1})/2$. This procedure allows for finding the temperature gradient ∇_i, which gives $F_{\rm conv}$ that conserves the total flux. In the final step, the Rosseland

mean optical depth, $\tau_{\rm R}$ is recalculated in each layer by integrating the hydrostatic equilibrium equation in discretized form

$$\tau_{R,1} = P_1 \frac{\chi_{R,1}}{g}, \tag{80}$$

$$\tau_{R,i} = \tau_{R,i-1} + (P_i - P_{i-1}) \frac{\chi_{R,i-\frac{1}{2}}}{g} \quad \text{for } i > 1. \tag{81}$$

We repeat the procedure outlined above in a loop to get simultaneous convergence in the hydrostatic equilibrium equation (Eq. 3), the radiative equilibrium equation in the radiative zone (Eq. 36) and the flux conservation in the convective zone (Eq. 4). A model is considered converged when the total flux in each layer is within 10^{-5} of $F = \sigma_R T_{\rm eff}^4$. If the input $P-T$ profile is relatively close to the converged solution, this procedure requires about 10 to 20 iterations. Once the $T-P$ profile is obtained we also have the chemical abundances of all species throughout the atmosphere and the synthetic spectrum that comes from the solution of the radiative transfer equation.

CHAPTER III

THE PHYSICS OF DENSE FLUIDS

In Chapters IV–VII, we will be calculating thermodynamical quantities like pressure, internal energy, chemical potentials of particles, chemistry and opacities of a spatially uniform, dense H/He medium in the absence of an external force field that would affect the behavior of the particles at microscopic scales. In this chapter we briefly present the theoretical methods used to conduct most of the work discussed in this dissertation: the statistical theory of liquids, non ideal chemistry, and ab initio quantum calculations based on the density functional theory (DFT). The material presented in this chapter is based mostly on two books: Martynov (1992) (§3.1-3.3) and Koch & Holthausen (2000) (§3.5)

3.1 Thermodynamical Quantities: A Statistical Approach

It is impossible to solve the equations of motion for all particles in a macroscopic system that consist of large number ($\sim 10^{23}$) of particles, and obtain the trajectory for each particle that would allow a calculation of thermodynamical quantities by averaging over time. At the beginning of the 20^{th} century, Gibbs suggested averaging over an ensemble of particles instead. This method grew into the method of distribution functions named the *Bogolyubov-Born-Green-Kirkwood-Ivon (BBGKY) hierarchy.* The calculation of thermodynamical quantities in the BBGKY hierarchy is based on Gibbs' distribution, where the coordinate part of the N particle distribution function G_N is given by

$$G_N(\vec{r}_1, ..., \vec{r}_N) = Z_N^{-1} \exp\left(-\frac{U_N}{k_B T}\right), \tag{82}$$

where $U_N = U_N(\vec{r}_1, ..., \vec{r}_N) = \frac{1}{2}\sum_{i,j} \Phi(\vec{r}_i - \vec{r}_j)$ is the total potential energy of N particles, $\vec{r}_i$ is the position vector of particle i, and $\Phi(\vec{r}_i - \vec{r}_j)$ is the pair interaction potential between particles i and j and is usually known from quantum calculations. For simplicity we assume that the medium consists of one type of particles. The equations for multiple component systems will be provided in

§3.2.1. The normalization constant Z_N, called *the partition function*, is defined as

$$Z_N = \frac{1}{V^N} \int_V \exp\left(-\frac{U_N}{k_B T}\right) d^3 r_1 ... d^3 r_N, \tag{83}$$

where V^N is the volume of a $3N$ dimension coordinate space. The two-particle distribution function for a spherically symmetric interaction potential (the most common case in this dissertation), is defined as

$$g(r) = \int G_N(\vec{r}_1, ..., \vec{r}_N) d^3 r_3 ... d^3 r_N = \exp\left(-\frac{\Phi(r)}{k_B T} + \omega(r)\right), \tag{84}$$

where $r = |\vec{r}_2 - \vec{r}_1|$ is the inter-particle separation and $\omega(r)$ is the *partial thermal potential.*

The function $g(r)$ describes the relative distributions of particles in a medium. It reduces to $g(r) = 1$ for the ideal gas. Given a pair interaction potential $\Phi(r)$, the knowledge of $g(r)$ allows for a full thermodynamical description of the fluid. The internal energy of system of N particles is calculated as a sum of kinetic and potential energy

$$E_{int,N} = \frac{3}{2} N k_B T + \frac{1}{2} n^2 \int_V \Phi(r) g(r) d^3 r + T^2 \frac{\partial (N k_B \ln Z_{int})}{\partial T}\Big|_V, \tag{85}$$

where $n = N/V$ denotes the number density of particles and Z_{int} is the internal partition function that accounts for the internal degrees of freedom of atoms or molecules (Hummer & Mihalas, 1988). The pressure P of the system is given by:

$$P = n k_B T + \frac{1}{6} n^2 \int_0^\infty r \frac{d\Phi(r)}{dr} g(r) 4\pi r^2 dr + \frac{\partial (n k_B T V \ln Z_{int})}{\partial V}\Big|_T. \tag{86}$$

The integrals in Eqs. (85) and (86) represent the contribution to the internal energy and pressure that arises from the inter particle interactions.

Knowing the internal energy, $E_{int,N}$, the entropy of the system, S_N, is given by

$$T S_N = E_N + k_B T \ln Z_N + N k_B T \ln Z_{int} + N k_B T \left[\ln\left(\frac{V}{N}\right) + 1 + \frac{3}{2} \ln\left(\frac{m k_B T}{2\pi\hbar^2}\right)\right]. \tag{87}$$

The last term in Eq. 87 represents the quantum partition function in phase space, where one particle occupies a phase space volume of $(2\pi\hbar)^3$ (Cox & Giuli, 1968).

The free energy of the system may be calculated from the fundamental thermodynamical identity,

$$F_N = E_N - TS_N \tag{88}$$

This is a very important thermodynamical function, as the chemistry of the equilibrium system is given by its minimization (§3.4). In the calculation of the chemical equilibrium of the system it is useful to work with the chemical potential, μ defined as

$$\mu = \frac{\partial F_N}{\partial N}\Big|_{T,V}. \tag{89}$$

3.2 Ornstein-Zernike Equation

In this section we present a method to calculate the two-particle distribution function $g(r)$, given a pair interaction $\Phi(r)$. As $g(r) \to 1$ for $r \to \infty$, it is convenient to work with the *total correlation function* $h(r)$,

$$h(r) = g(r) - 1. \tag{90}$$

As $r \to \infty$ both $h(r)$ and $\omega(r)$ asymptotically approach 0. $h(r)$ is obtained by the solution of the Ornstein-Zernike equation that is a fundamental equation in the statistical theory of uniform fluids (Martynov, 1992)

$$h(r) = C(r) + n \int_V C(r_3) h(|\vec{r}_3 - \vec{r}|) d^3 r_3, \tag{91}$$

where $C(r)$ is the *second order correlation function*

$$C(r) = h(r) - \omega(r) + M(r). \tag{92}$$

The function $M(r)$ is called the *bridge functional*, which is generally unknown and must be approximated to close the set of equations (Eq. 84), (Eq. 91) and (Eq. 92). In our work we will use the two most common approximations: the hypernetted chain approximation (HNC), where $M(r) = 0$,

which is most suitable for long range potentials (e.g., Coulomb), and the Percus-Yevick approximation (PY), where $M(r) = 1 + \omega(r) - e^{\omega(r)}$, which gives more accurate results for short-range potentials (interatomic and intermolecular).

For a given interaction potential $\Phi(r)$ Eqs. (84), (91), and (92) allow for the calculation of $g(r)$. Knowing the pair distribution function, we can then compute the $E_{int,N}$ and P through Eqs. (85) and (86), respectively.

The Ornstein-Zernike equation (Eq. 91) involves a convolution and is usually solved in Fourier space where it takes a simple form

$$h(k) = C(k) + nh(k)C(k), \tag{93}$$

where

$$h(k) = \int_V h(r)e^{-i\vec{k}\vec{r}}d\vec{r} = 4\pi \int_0^\infty h(r)\frac{sinkr}{kr}r^2 dr, \tag{94}$$

and

$$C(k) = \int_V C(r)e^{-i\vec{k}\vec{r}}d\vec{r} = 4\pi \int_0^\infty C(r)\frac{sinkr}{kr}r^2 dr. \tag{95}$$

The non ideal contribution to the chemical potential μ, that arises from inter-particle interactions, is

$$\mu^{nid} = 4\pi k_B T \int_0^\infty h(r) - \omega(r) - \frac{1}{2}h(r)(\omega(r) + \frac{1}{3}M(r))r^2 dr. \tag{96}$$

Besides the pair distribution function $g(r)$, another useful function is the *structure factor*, $S(k)$, defined as

$$S(k) = 1 + nh(k). \tag{97}$$

As the structure factor is linear in $h(k)$, it represents the Fourier transform of $g(r)$. Examples of both $g(r)$ and $S(k)$ for helium are given in Fig. 10. At large r and k, both $g(r)$ and $S(k) \to 1$. For all real substances, the pair distribution function drops to 0 at small distances, even in the dilute gas limit. This behavior reflects the strong repulsion between two helium atoms at short distances that prevents the atoms from being on top of each other. On the other hand, the structure factor,

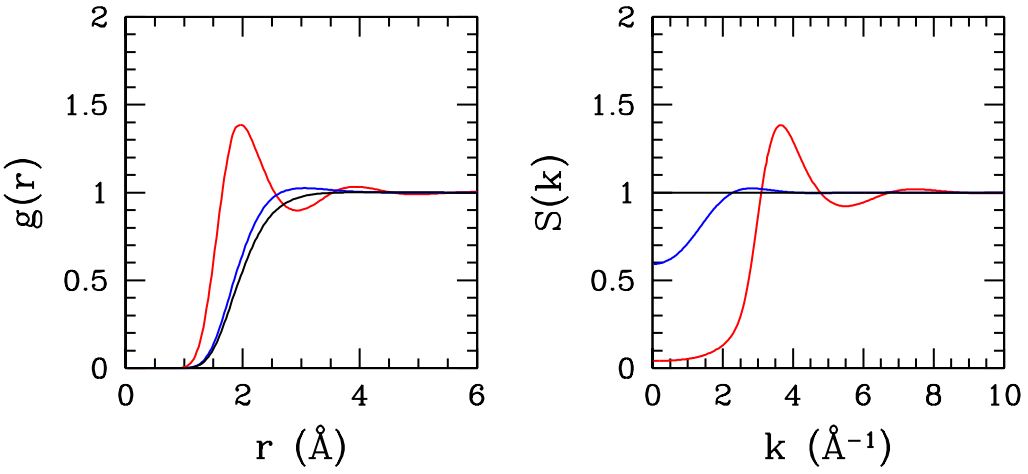

Figure 10: The pair distribution (left panel) and the structure factor (right panel) in helium for different densities: $10^{-4}\,\mathrm{g/cm^3}$ (black), $0.1\,\mathrm{g/cm^3}$ (blue), and $1\,\mathrm{g/cm^3}$ (red) at $T = 5000\,\mathrm{K}$.

$S(k)$, is 1 in a dilute gas and in fluids it drops to small values for small k. The oscillations visible in both functions at the largest density indicate strong correlations and the nonuniform, shell-like relative distribution of particles in the fluid.

3.2.1 Many Component Systems

Expressions for the thermodynamics of a mixture of m species are generalized in the following equations

$$\epsilon_{int} = \frac{3}{2}k_B T + \frac{1}{2}n\sum_{\alpha\beta}\nu_\alpha\nu_\beta\int_0^\infty \Phi_{\alpha\beta}g_{\alpha\beta}(r)4\pi r^2 dr + \sum_\alpha T^2\frac{\partial(k_B \ln Z_{\alpha,int})}{\partial T}\Big|_V \tag{98}$$

$$P = nkT + \frac{1}{6}n\sum_{\alpha\beta}\nu_\alpha\nu_\beta\int_0^\infty r\frac{d\Phi_{\alpha\beta}(r)}{dr}g_{\alpha\beta}(r)4\pi r^2 dr + \sum_\alpha \frac{\partial(n_\alpha k_B T V \ln Z_{\alpha,int})}{\partial V}\Big|_T, \tag{99}$$

where ϵ_{int} is the internal energy per particle,

$$\nu_i = \frac{n_i}{n}, \quad n = \sum_{i=1}^{m} n_i, \tag{100}$$

and α and β label the species. The pair distribution function $g_{\alpha,\beta}(r)$ is

$$g_{\alpha\beta}(r) = \exp\left(-\frac{\Phi_{\alpha\beta}(r)}{k_B T} + \omega_{\alpha\beta}(r)\right), \tag{101}$$

and Eqs. (90), (91), and (92) become

$$h_{\alpha\beta}(r) = g_{\alpha\beta}(r) - 1 \tag{102}$$

$$h_{\alpha\beta}(r) = C_{\alpha\beta}(r) + \frac{1}{2}\sum_{\gamma=1}^{m} n_\gamma \int_V \left[C_{\alpha\gamma}(r_3) h_{\gamma\beta}(|\vec{r}_3 - \vec{r}|) + C_{\beta\gamma}(r_3) h_{\gamma\alpha}(|\vec{r}_3 - \vec{r}|)\right] d^3 r_3 \tag{103}$$

and

$$C_{\alpha\beta}(r) = h_{\alpha\beta}(r) - \omega_{\alpha\beta}(r) + M_{\alpha\beta}(r), \tag{104}$$

respectively. Finally, the non ideal contribution to the chemical potential of species α is

$$\mu_\alpha^{nid} = k_B T \left(\sum_\beta \int_0^\infty h_{\alpha\beta}(r) - \omega_{\alpha\beta}(r) - \frac{1}{2} h_{\alpha\beta}(r)(\omega_{\alpha\beta}(r) + \frac{1}{3} M_{\alpha\beta}(r)) 4\pi r^2 dr\right) \tag{105}$$

Due to symmetry, α and β are interchangeable in the above equations $g_{\alpha\beta}(r) = g_{\beta\alpha}(r)$, $h_{\alpha\beta}(r) = h_{\beta\alpha}(r), ...$ etc. We have programmed the self-consistent numerical solution of equations (101)–(104), to obtain $g_{\alpha\beta}(r)$ and from it the thermodynamics of the interacting fluid.

3.3 Classical Simulations of Dense Media

Computer simulations are one of the most powerful tools for investigating many-particles systems. Molecular Dynamics and Monte Carlo are the most commonly used simulation methods, and closely reproduce the behavior of real physical systems. The computation of thermodynamics in the former method is based on averaging over time, whereas the later uses averaging over the ensemble. In

principle these methods always should give the same answers. This equivalence is established by quite a complicated mathematical theory of ergodic systems (Martynov, 1992).

The advantage of using simulations over the classical theory of fluids is that for a given inter-particle interaction potential $\Phi(r)$, there is no need for any approximation (such as the bridge functional, $M(r)$ in Eq. (92)) and results are principally exact. Moreover, simulations generate actual distributions of particles that may be used as input for other calculations, such as the calculation of the electronic structure of dense fluids (Chapter VI).

All thermodynamical quantities can be calculated in the same way as stated in §3.1, through the knowledge of pair distribution function, $g(r)$, obtained from an analysis of the distribution of particles in a simulation. The internal energy and pressure also can be computed by averaging the configurations of particles generated in the simulation, where for each configuration $(\vec{r}_1, ..., \vec{r}_N)$ the internal energy and pressure are computed with

$$E_{int,N} = \frac{3}{2} N k_B T + \frac{1}{2} \sum_{i>j=1}^{N} \Phi(r_{ij}) + T^2 \frac{\partial (N k_B \ln Z_{int})}{\partial T}\Big|_V, \tag{106}$$

and

$$P = n k_B T + \frac{1}{6} \sum_{i>j=1}^{N} r_{ij} \frac{d\Phi(r_{ij})}{dr_{ij}} + \frac{\partial (n k_B T V \ln Z_{int})}{\partial V}\Big|_T, \tag{107}$$

where $r_{ij} = |\vec{r}_i - \vec{r}_j|$.

3.3.1 Classical Molecular Dynamics Simulations

In this method the particle positions and momenta are propagated in time along classical trajectories calculated from the classical equations of motion. The simplest numerical realization of such a calculation is given by

$$\vec{p}_i^{\,k+1} = \vec{F}_i^{\,k} \Delta t + \vec{p}^{\,k}, \tag{108}$$

and

$$\vec{r}_i^{\,k+1} = \vec{r}_i^{\,k} + \frac{\vec{p}_i^{\,k+1}}{m_i} \Delta t, \tag{109}$$

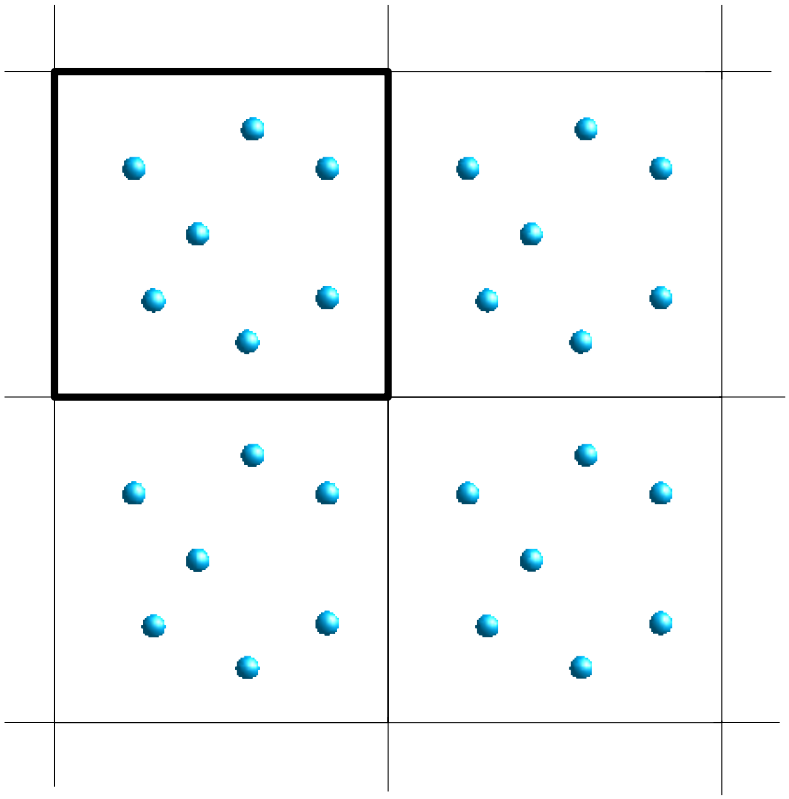

Figure 11: The periodic boundary condition used in both Molecular Dynamics and Monte Carlo simulation methods. Positions of particles in unit cells are exact replicas of particles positions from the simulation cell, marked by thick lines.

where $\vec{p}_i^k$ and $\vec{r}_i^k$ are the momentum and position of particle i, m_i is its mass, $\vec{F}_i^k$ is the force acting on it due to interactions with the other particles, Δt is the time step, and k indicates the iteration step.

As it is impossible to simulate a macroscopic system of $N \sim 10^{23}$ particles, the system is partitioned into V/L^3 identical systems of $N \sim 10^2 - 10^3$ particles, where V is the volume of the macroscopic system and L is the length of the cubic, unit cell (the simulation box). Periodic boundary conditions are imposed to simulate a system of infinite extent, so the position of the particles in the different cells are exact replicas of the position in the simulation cell (Fig. 11). L and N must be large enough to eliminate the chance of correlations between particles from the neighboring unit cells. Initially, particles are assigned random positions in the simulation box, with random velocities following a Maxwell distribution.

3.3.2 Classical Monte Carlo Simulations

Monte Carlo simulations, named after the city with world-famous casinos, are based on averaging over the ensemble. For these simulations, we use the same approximations for the simulation box, periodic boundary conditions, and initial spatial distribution of particles as described in the section on molecular dynamics simulations. The key quantity is the total potential energy, $U_N(\vec{r}_1, ..., \vec{r}_N) = \frac{1}{2}\sum_{i,j}\Phi(\vec{r}_i - \vec{r}_j)$ of a configuration of the N-particle system. For a given initial configuration of particles in the simulation box, we randomly change the position of one particle by

$$\vec{r}_i^{\,k} \rightarrow \vec{r}_i^{\,k} + (\alpha L, \beta L, \gamma L), \tag{110}$$

where α, β, and γ are random numbers in the interval from -1 to $+1$ and L is the length of the simulation box. Such a displacement results in a change in the interaction energy, ΔU_N, of the whole system. If ΔU is negative, then the displacement is accepted. In the case when $\Delta U_N > 0$ it is accepted conditionally, i.e., with the probability $\exp(-\Delta U/k_B T)$. This operation is repeated again and again for each particle. This procedure eventually brings the system to the minimum energy state around which it fluctuates, mimicking the thermal fluctuations of a real system.

3.4 Chemical Equilibrium in Non Ideal Systems

The interaction between chemical species affects their relative abundance. To calculate the chemical equilibrium of an interacting fluid, we use the free-energy-minimization approach (Cox & Giuli, 1968). The chemical equilibrium for a reaction

$$A_1 + A_2 + A_3 + ... \leftrightarrow B_1 + B_2 + B_3 + ... \tag{111}$$

is obtained when

$$\mu_{A_1} + \mu_{A_2} + \mu_{A_3} + ... = \mu_{B_1} + \mu_{B_2} + \mu_{B_3} + ..., \tag{112}$$

where the chemical potentials μ_i include: ideal (id) and non ideal (nid) contributions. The former arises from the internal degrees of freedom of atoms and molecules and the quantum partition of

phase space and is expressed as

$$\mu^{id} = E_0 - k_B T \ln Z_{int} + k_B T \left[\ln n - \frac{3}{2} \ln \left(\frac{m k_B T}{2\pi\hbar^2} \right) \right], \tag{113}$$

where E_0 is the ground state energy of the species under consideration. The non ideal part of the chemical potential is given by Eqs. (105).

3.5 The Density Functional Theory

3.5.1 Basic Assumptions

The statistical approach presented so far is valid when describing the interactions between classical particles, such as atoms, molecules, and ions. To describe the electrons – both free and those bound in the atoms – and their interactions with nuclei in dense systems we have to use the methods of quantum mechanics. To obtain a full description of a N-electrons system we have to solve the Schrödinger equation for the N-particle wave function. This wave function is usually very complicated and for any calculations of many electrons systems, like the Hartree-Fock (HF) approximation, it reaches an unmanageable size. On the other hand, the Hamilton operator $\hat{H}$ acts only on one or two particles at a time and, in principle, it is possible to write a Schrödinger equation that depends on fewer than $4N$ variables (three spatial + one spin variable for each electron). In the Density Functional Theory (DFT), one uses the charge density of the electrons, $\rho(\vec{r})$, that depends only on the three spatial variables for a full quantum mechanical description of the N-electron system. The DFT is used extensively in condensed matter physics to compute the electronic structure of solids and in quantum chemistry to compute the properties of complex molecules.

The first attempt to use the electron density rather than wave functions in quantum calculations was made by Thomas (1927) and Fermi (1927). In the Thomas-Fermi model (TF) designed to calculate the energies of a single many-electrons atom, the energy of the N-electrons and 1 nucleus of charge Z is given by

$$E_{\mathrm{TF}} = \frac{3}{10}(2\pi^2)^{2/3} \int \rho^{5/3}(\vec{r}) d\vec{r} - Z \int \frac{\rho(\vec{r})}{r} d\vec{r} + \frac{1}{2} \int \int \frac{\rho(\vec{r}_1)\rho(\vec{r}_2)}{r_{12}} d\vec{r}_1 d\vec{r}_2, \tag{114}$$

where the first term is the kinetic energy approximated by that of the free electron gas, and the following terms represent the Coulomb electron-nucleus and electron-electron interactions, respectively. The proper electron density $\rho(\vec{r})$ is that which gives the lowest energy, and it is found by applying a variational principle. Two significant deficiencies of the TF model are that it does not contain the correct kinetic energy (ideal gas assumption) and the inter-electronic exchange and correlations quantum effects (Davydov, 1965) are completely neglected.

The formal justification for expressing the electronic energy in terms of the electron charge density is provided by the Hohenberg-Kohn theorems (Hohenberg & Kohn, 1964). Hohenberg and Kohn proved that the electron density $\rho(\vec{r})$ uniquely determines the Hamilton operator and thus all properties of the system (the first theorem). The electronic energy can be written as

$$E_e(\rho) = \int \rho(\vec{r}) \sum_j^M \frac{Z_j \rho(\vec{r})}{|\vec{r} - \vec{r}_j|} d\vec{r} + F_{\mathrm{HK}}(\rho), \tag{115}$$

where j labels the nuclei. The first term contains the electron-nucleus interaction energies that depend on distribution of nuclei. F_{HK} is the Hohenberg-Kohn functional that involves only the electron-electron interaction terms, and is expressed by

$$F_{\mathrm{HK}}(\rho) = T(\rho) + E_{ee}(\rho), \tag{116}$$

where T is the kinetic energy of the electrons and E_{ee} contains electron-electron interactions terms. The functional F_{HK} is universal, i.e., for a given $\rho(\vec{r})$ it is completely independent of the distribution of nuclei. If F_{HK} were known exactly we would have an exact solution of the Schrödinger equation. Also, as the ground state electron density $\rho(\vec{r})$ determines the Hamiltonian (which characterizes all states of the system), all properties of all states are determined by the ground state density.

The second Hohenberg-Kohn theorem states that the F_{HK} functional delivers the ground state energy of the system only when the true ground state electron density is used. Therefore, it assures us that the electron density found by the variational method resembles the actual density of the ground state.

3.5.2 The Kohn-Sham Approach

The main limitation of the TF model is the approximation of the kinetic energy by that of a free electron gas. To go beyond this approximation, Kohn & Sham (1965) mapped the problem of the N interacting electrons to an equivalent system of N non interacting electrons, as in the Hartree-Fock approximation. They set up a reference system of non interacting electrons with a Hamiltonian

$$\hat{H}_s = -\frac{\hbar^2}{2m}\sum_i^N \nabla_i^2 + \sum_i^N V_s(\vec{r}_i), \tag{117}$$

where $V_s(\vec{r}_i)$ is an effective local potential. The wave function of such a system is represented by a Slater determinant. The orbitals, ϕ_i, are determined by the solution of a one-electron Kohn-Sham (KS) equation:

$$\hat{f}^{\mathrm{KS}}\phi_i = \epsilon_i\phi_i, \tag{118}$$

where $\hat{f}^{\mathrm{KS}}$ is the one-electron KS operator defined as

$$\hat{f}^{KS} = -\frac{\hbar}{2m_e}\nabla_i^2 + V_s(\vec{r}_i) \tag{119}$$

and ϕ_i are the KS orbitals. The reference system is related to the real one by the choice of the effective potential $V_s(\vec{r}_i)$, such that the electron density obeys the equation

$$\rho(\vec{r}) = \sum_i^N \sum_s |\phi_i(\vec{r}, s)|^2, \tag{120}$$

where s labels the spin state. The effective potential is written as:

$$V_s(\vec{r}_i) = \int \frac{\rho(\vec{r}_2)}{r_{i2}} d\vec{r}_2 + V_{xc}(\vec{r}_i) - \sum_j^M \frac{Z_j}{r_{1j}}. \tag{121}$$

As $V_s(\vec{r})$ depends on the electron density, which depends on the KS orbitals, equations (118) and (121) must be solved self-consistently. The exchange-correlation potential is defined in terms of the

exchange correlation energy E_{xc}

$$V_{xc} = \frac{\delta E_{xc}}{\delta \rho} = \frac{\partial(\rho \epsilon_{xc}(\rho))}{\partial \rho}, \tag{122}$$

where ϵ_{xc} is the exchange-correlation energy per electron. Unlike in the HF model, where we assume the form of the wave function to be a Slater determinant, the KS approach is, in principle, exact. The only approximation is the unknown function for the exchange-correlation energy E_{xc}. As $V_s(\vec{r})$ is local, i.e., depends only on values at $\vec{r}$, the KS equation has a much less complicated structure than the single electron equation in the HF approximation, where the exchange operator $\hat{K}_j$ acting on the orbital-i depends on the value of one-electron orbital everywhere in the coordinate space (Davydov, 1965). As the kinetic energy in the KS equation is not that of the real system, the E_{xc} contains also corrections to the kinetic energy. Knowledge of the exact E_{xc} is equivalent to an exact solution of the Schrodinger equation. Some of the common approximations for E_{xc} are given in the next section.

With a knowledge of the KS orbitals, the total energy is given by

$$E_e = -\frac{\hbar}{2m_e} \sum_i < \phi_i | \nabla^2 | \phi_i > + \frac{1}{2} \int \int \frac{\rho(\vec{r}_1)\rho(\vec{r}_2)}{r_{12}} d\vec{r}_1 d\vec{r}_2 + E_{xc}[\rho] - \int \sum_j^M \frac{Z_j \rho(\vec{r})}{|\vec{r} - \vec{r}_j|} d\vec{r}. \tag{123}$$

3.5.3 Approximations for Exchange-Correlation Energy

The local density approximation (LDA)

In the LDA approximation the exchange-correlation energy is given by

$$E_{xc}^{LDA} = \int \rho(\vec{r}) \epsilon_{xc}(\rho(\vec{r})) d\vec{r}, \tag{124}$$

where ϵ_{xc} is the exchange-correlation energy per particle of a uniform electron gas of density $\rho(\vec{r})$. The exchange part can be calculated analytically, whereas the correlation part is derived from the accurate quantum Monte Carlo simulations of the homogeneous electron gas (Ceperley & Alder, 1980)

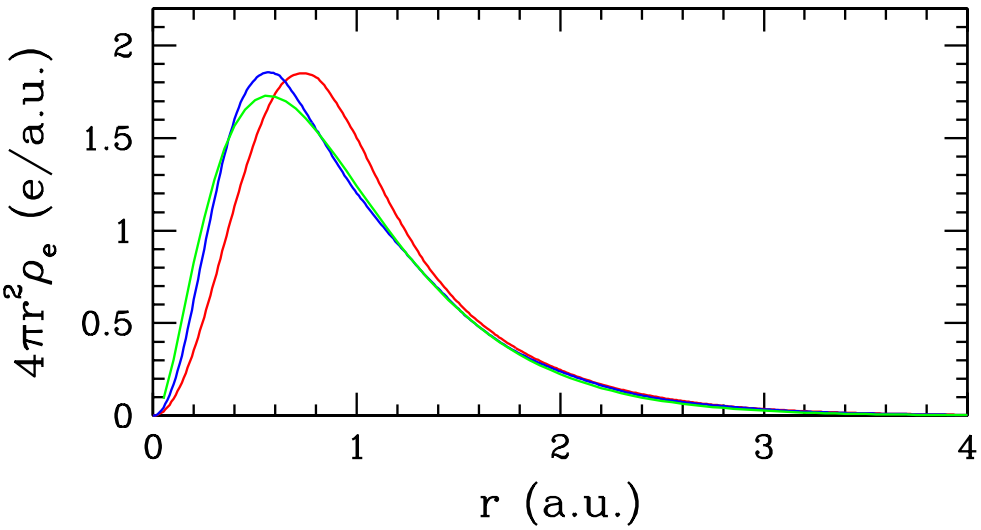

Figure 12: The charge density in an isolated helium atom. Colors indicate various calculations: exact (Hart & Herzberg (1956), green), DFT-LDA (red), and DFT-GGA (blue).

As for real systems the electron densities are not even close to that of the uniform electron gas; the LDA approximation must be extended to include the effect of spatial variations in the electron density.

The generalized gradient approximation (GGA)

In the construction of GGA exchange-correlation energy, the knowledge of $\nabla\rho$ is used to include some information about the spatial variations of $\rho(\vec{r})$. There exists several approximations for the exchange and correlation parts of E_{xc}^{GGA}. In our calculations we use the most common approximations: the so-called PBE functional (Perdew et al., 1996), the PW91 and PW92 functionals (Perdew & Wang, 1992) and the BLYP functional (Becke (1988); Lee et al. (1988)).

Figure 12 shows the electron charge density of an isolated helium atom calculated with the DFT formalism in the LDA and the GGA-PBE approximations. In both cases the exact charge density

(Hart & Herzberg, 1956) is qualitatively reproduced. However, the GGA functional gives a much better agreement with the exact result.

3.5.4 Finite Temperature Calculation

The above DFT scheme is developed for electrons in the ground state at $T = 0\,\mathrm{K}$. For systems at finite temperature, equations (120) and (123) are modified

$$\rho_s(\vec{r}) = \sum_i^N \sum_s f_i(\epsilon_i)|\phi_i(\vec{r}, s)|^2 = \rho_0(\vec{r}) \tag{125}$$

$$E_e = -\frac{\hbar}{2m_e}\sum_i f_i(\epsilon_i) < \phi_i|\nabla^2|\phi_i > \; + \frac{1}{2}\int\int \frac{\rho(\vec{r}_1)\rho(\vec{r}_2)}{r_{12}} d\vec{r}_1 d\vec{r}_2 + E_{xc}[\rho] + \int \sum_j^M \frac{Z_j\rho(\vec{r})}{|\vec{r} - \vec{r}_j|} d\vec{r}, \tag{126}$$

where $f_i = f_i(\epsilon_i)$ is the occupation probability of level ϵ_i given by the Fermi-Dirac statistics. The quantity that is minimized in this case is the electronic free energy $F_e = E_e - TS_e$, where E_e is the total electronic energy and the electronic entropy S_e is (Nikiforov et al., 2005)

$$S_e = -k_B \sum_i^N \left[f_i \ln f_i + (1 - f_i)\ln(1 - f_i)\right]. \tag{127}$$

CHAPTER IV

REFRACTION IN COOL WHITE DWARF ATMOSPHERES

Problems involving radiative transfer in refractive media appear to have received limited attention (Harris, 1965; Zheleznyakov, 1967; Pomranin, 1968). In stellar atmospheres in particular, refraction is always ignored because the gas is so tenuous that the index of refraction does not depart from unity. A notable exception is found in the atmospheres of very cool white dwarfs, especially those rich in helium, where the gas (or rather the fluid) density can reach $0.1 - 2\,\mathrm{g/cm^3}$. Under these conditions, the refractive index of fluid, atomic helium can become as large as ~ 1.3 with very large gradients (Fig. 7) and refraction can be expected to affect the radiation field.

4.1 Refraction in White Dwarf Atmospheres

There is a number of interesting physical effects that we can expect in a stellar atmosphere where the index of refraction is greater than unity. The index n_ν is a monotonically increasing function of density. In a stellar atmosphere, the index decreases from the bottom toward the surface where $n_\nu = 1$ at $\tau_\nu = 0$. All rays are refracted away from the upward vertical and some rays are internally reflected back toward the interior (Fig. 8). Intuitively, this effect should lead to an increase in the temperature profile of the atmosphere to achieve flux conservation. Because the largest variations of the index occur in the optically thin regions of the atmosphere (Fig. 7), we expect refraction to be mainly a surface effect. Furthermore, the group velocity of light is reduced by a factor of n_ν so it increases toward the surface where it reaches the speed of light in a vacuum. This result directly effects the flux through its dependence on the velocity of propagation. The angular redistribution of light due to refraction will reduce the limb darkening effect. Finally, the index of refraction of fluid helium is nearly independent of frequency from the optical to the near infrared and there should not be any significant chromatic effects.

To illustrate the effects of refraction in a stellar atmosphere, we apply the Feautrier method (§2.2.3) to solve for the radiation field in a helium-rich white dwarf atmosphere model with $T_{\mathrm{eff}} =$

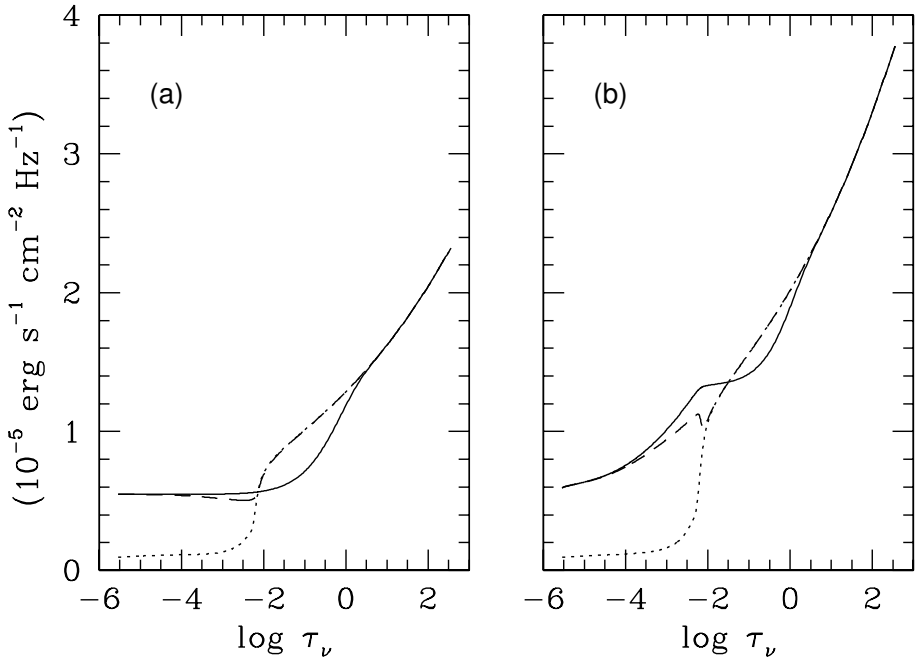

Figure 13: Mean intensity J_ν (solid line), source function S_ν (dashed line), and Planck function $n_\nu^2 B_\nu$ (dotted line) for non refractive (a) and refractive (b) cases as a function of vertical optical depth τ_ν in the nominal white dwarf atmosphere model for $\lambda = 0.948\,\mu$m.

4000 K, a gravity of $\log g = 8$, and a homogeneous composition of He/H $= 10^6$. We will refer to this atmospheric structure, obtained with our white dwarf atmosphere code (Chapter II), as the "nominal" model for the rest of this chapter. The index of refraction of helium is expressed as a virial expansion (Appendix A).

Figure 13 shows the mean intensity, the source function, and the Planck function for the refractive and non refractive cases for the same nominal (T, P) structure. In the refractive case, J_ν increases by a factor of n_ν^2 at large optical depth because $J_\nu \sim S_\nu \sim n_\nu^2 B_\nu$ (Eq. 43). For $\tau_\nu < 10^{-2}$, $n_\nu \sim 1$ and $n_\nu^2 B_\nu \sim B_\nu$. However, J_ν remains significantly larger than in the non refractive case because of total internal reflection. This can be understood from the angular distribution of the radiation. Figure 14 shows the angular dependence of the symmetric average of the specific intensity P'_ν (40) for both cases at different levels in the atmosphere. Deep inside the atmosphere P'_ν is just the Planck

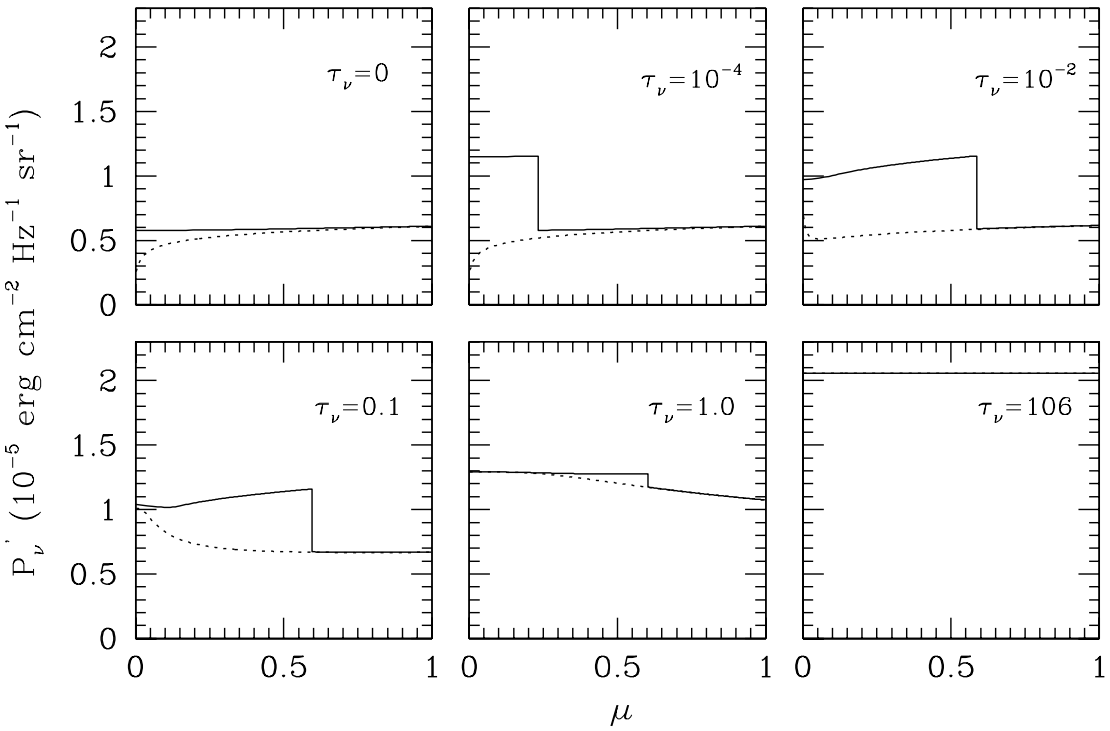

Figure 14: Symmetric average of the specific intensity $P'_\nu = P_\nu/n_\nu^2$ for refractive (solid line) and non refractive (dotted line) cases as a function of angle $\mu = \cos\theta$ at various levels in the nominal white dwarf atmosphere model. $\mu = 0$ and 1 correspond to the horizontal and vertical directions, respectively. The wavelength is $\lambda = 0.948\,\mu$m.

function B_ν and it is the same in both cases. Toward the surface, P'_ν splits into two regions separated by a discontinuity at $\mu = \mu_c(\tau_\nu)$. The additional intensity for $\mu < \mu_c$ arises from the contribution of ray paths that have been reflected at lower τ_ν (above the level considered). Toward the surface, P'_ν doubles across the discontinuity

$$P'_\nu(\mu_c^-) \sim 2P'_\nu(\mu_c^+) \tag{128}$$

because the contribution from the source function in the optically thin regions lying above for $\mu > \mu_c$ is negligible, but the contribution from the downward rays ($\mu < 0$) that have been reflected higher up is nearly the same as for the upward rays ($\mu > 0$), because of negligible absorption-emission effects inside the optically thin region. This effect should result in a warming of an atmosphere in

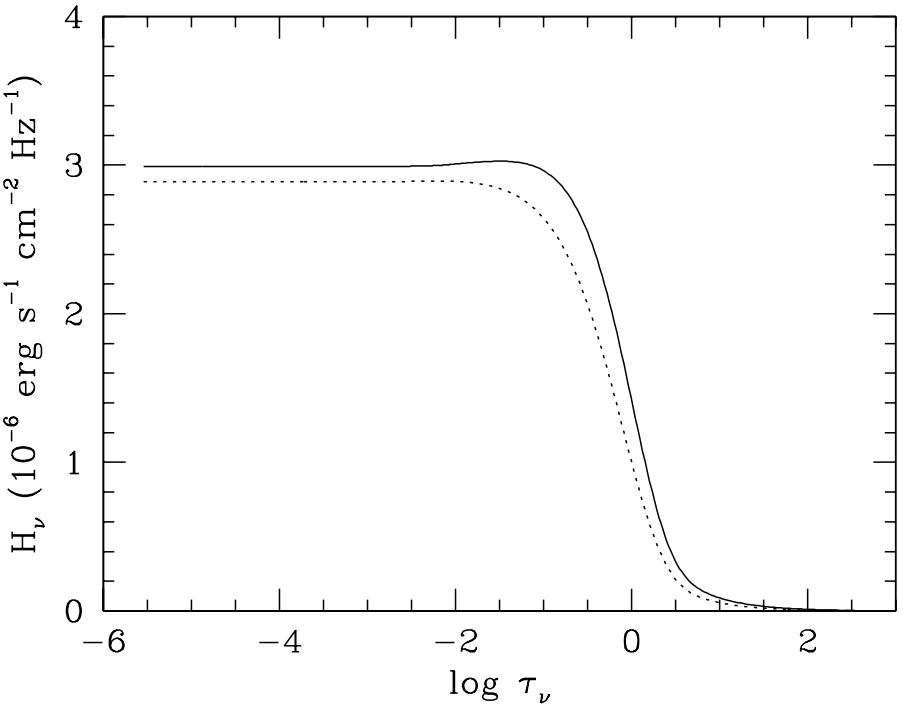

Figure 15: Eddington flux for the refractive (solid line) and the non refractive (dotted line) cases as a function of the vertical optical depth in the nominal white dwarf atmosphere model for $\lambda = 0.948\,\mu$m. The atmospheric structure is the same for both calculations, which is why the surface fluxes are slightly different and the refractive case shows a small bump at $\tau_\nu \sim 0.1$.

radiative equilibrium because an increase in the mean intensity J_ν must generally be compensated for by an increase in the Planck function B_ν (Eqs. 36 and 43).

The angular distribution of the emergent radiation, known as limb darkening, is affected by refraction. Limb darkening can be seen in the first panel of Fig. 14 because at $\tau = 0$, $P'_\nu(\mu) = P_\nu(\mu) = I_\nu(\mu)$. In the non refractive case, we have $I_\nu(\tau_\nu = 0, \mu = 0)/I_\nu(0,1) = 0.423$ for $\lambda = 0.948\,\mu$m. When refraction is introduced, the limb darkening is much weaker and $I_\nu(0,0)/I_\nu(0,1) = 0.947$. In the presence of refraction, ray paths that emerge with $\mu \sim 0$ (horizontally) are strongly deflected. The vertical optical depth τ_ν for a ray path exiting with $\mu = 0$ is related to the optical

depth, σ_ν measured along the ray-path by

$$\tau_\nu = \int_0^{\sigma_\nu} \sqrt{1 - 1/n_\nu^2(\sigma'_\nu)}\, d\sigma'_\nu. \tag{129}$$

For $n_\nu(\tau_\nu)$ shown in Fig. 7 and $\sigma_\nu = 1$, we get $\tau_\nu = 0.56$. This means that due to refraction, a horizontal viewing angle allows us to see as deep inside the atmosphere as under angle $\mu = 0.56$ in the non refractive case. We can indeed see on Fig. 14 that $I'_\nu(0,0)_{\rm ref} = I'_\nu(0,0.56)_{\rm non\ ref}$.

Despite the significant change in the specific intensity shown in Fig. 13, the radiative fluxes are nearly identical throughout the atmosphere (Fig. 15). This happens because in the absence of absorption and emission, refraction is a geometric effect that does not affect the value of the integral (Eq. 20). By symmetry, the reflected ray paths do not contribute to the flux ($I'_\nu(+\mu) = I'_\nu(-\mu)$) and Snell's law implies that $n_\nu^2 \mu d\mu$ is constant. For reflected ray paths in an actual atmosphere, $I'_\nu(\tau_\nu, \mu > 0) > I'_\nu(\tau_\nu, \mu < 0)$, as emission is usually larger deeper inside the atmosphere, and absorption processes are present. This explains why the Eddington flux H_ν is slightly larger in the refractive case and increases between $\tau_\nu \sim 10^{-6}$ and 0.1. For $\tau_\nu > 0.1$, the radiative flux decreases rapidly due to the presence of a convective zone, a characteristic of all cool white dwarf atmospheres models.

So far, our discussion of the effects of refraction on the radiation field are based on a fixed (non refractive) atmospheric pressure-temperature structure. A full atmosphere calculation consists of finding the structure that satisfy the hydrostatic equilibrium and the flux conservation equations (Eq. (3) and (4) respectively). Figure 16 compares such a self-consistent calculation for both the non refractive and the refractive cases (nominal model) . As expected, internal reflection leads to a hotter structure near the surface. The spectra resulting from these self-consistent structures are shown in Fig. 16. The $0.4\,\mu\mathrm{m}^{-1}$ feature seen in the non refractive case is caused by collision-induced absorption (CIA) by the small amount of H_2 molecules present in this model ($n(H_2)/n(He) \sim 4 \times 10^{-7}$). In the refractive case, the hotter structure results in the dissociation of H_2 and reduces the CIA absorption. The effects of refraction become much larger in models with lower effective temperatures or higher gravities as both effects increase the density and the index of refraction in

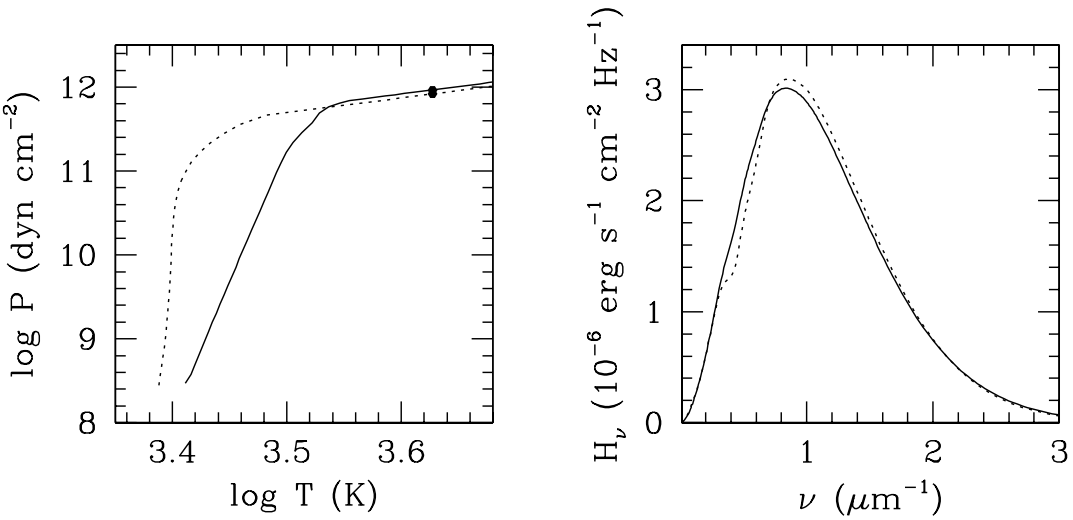

Figure 16: Pressure-temperature structure (left panel) and synthetic spectrum (right panel) for the nominal white dwarf atmosphere model parameters with (solid line) and without (dotted line) dispersive effects. Both models are computed by imposing flux conservation and hydrostatic equilibrium. The filled circle indicates the level where the Rosseland mean optical depth $\tau_R = 1$.

the atmosphere. On the other hand, the density and the index generally decrease as the hydrogen abundance increases, with reduced refractive effects.

CHAPTER V

DISSOCIATION EQUILIBRIUM OF H_2 IN DENSE HELIUM

In this chapter we present the solution for the dissociation of molecular hydrogen in dense fluid helium, in the limit He/H >> 1 (Kowalski, 2006a). We introduce non ideal effects in the calculation of the dissociation equilibrium of molecular hydrogen through a modification of the chemical potentials of H and H_2. We find that the strong interactions in dense, helium-rich atmospheres make H_2 more stable against dissociation. This stability results in a significant decrease in the dissociation fraction of molecular hydrogen, with a corresponding increase in the $H_2 - He$ collision-induced absorption (CIA) opacity. H_2. This particular problem illustrates the method we will apply to dense helium (Chapter VI) and to the ionization of H^- (Chapter VIII).

5.1 The Dissociation Equilibrium of Molecular Hydrogen in an Interacting Fluid

5.1.1 Theoretical Approach

The condition for chemical equilibrium (at a given density and temperature) for the dissociation reaction

$$H_2 \rightleftharpoons 2H \tag{130}$$

is given by (§3.4)

$$\mu_{H_2} = 2\mu_H, \tag{131}$$

where μ_i is a chemical potential of the species i expressed as (Eq. 113)

$$\mu_i = E_{0,i} + k_B T \ln \frac{n_i h^3}{Z_{int}(2\pi m_i k_B T)^{3/2}} + \mu_i^{nid}. \tag{132}$$

The first two terms on the r.h.s. of equation (132) represent the ideal contributions of translational and internal degrees of freedom, and μ_i^{nid} is the non ideal contribution to the chemical potential arising from the inter-particle interactions in the fluid (§3.2). Setting $\mu_i^{nid} = 0$, we recover the Saha

equation for the dissociation of molecular hydrogen

$$\beta^{id} = \frac{n_{\rm H_2}}{n_{\rm H}^2} = \frac{Z_{\rm H_2}}{Z_{\rm H}^2}\left[\frac{m_{\rm H_2}h^2}{2\pi m_{\rm H}^2 k_B T}\right]^{3/2} e^{D_0/k_B T}, \tag{133}$$

where $D_0 = 2E_{0,\rm H} - E_{0,\rm H_2} = 4.478\,\rm eV$ is the dissociation energy of the isolated hydrogen molecule. Even for trace species, like H or H_2 in dense helium, the μ_i^{nid} which arise from interactions with the atoms are not negligible and in principle should be comparable in magnitude to $\mu_{\rm He}^{nid}$.

If we define the quantity ΔI as

$$\Delta I = \mu_{\rm H_2}^{nid} - 2\mu_{\rm H}^{nid}, \tag{134}$$

the non ideal equilibrium equation can be written in the following form

$$\beta = \frac{n_{\rm H_2}}{n_{\rm H}^2} = \frac{Z_{\rm H_2}}{Z_{\rm H}^2}\left[\frac{m_{\rm H_2}h^2}{2\pi m_{\rm H}^2 k_B T}\right]^{3/2} e^{(D_0-\Delta I)/k_B T}$$

$$= \beta^{id} e^{-\Delta I/k_B T}. \tag{135}$$

Comparing (Eq. 133) with (Eq. 135), we see that the non ideal effects on the dissociation equilibrium can be *interpreted* as a change in the dissociation energy by a value of ΔI. For simplicity, we will adopt this interpretation hereafter.

In the atmosphere of cool white dwarfs, hydrogen exists mostly as H_2 and H, and the $\rm H/H_2$ ratio is governed by reaction (130) only. For a given temperature, density ρ, and composition $y = \rm He/H$ [1] (by number), the number densities of H_2 and H are

$$n_{\rm H} = \frac{-1 + \sqrt{1 + 8\beta n_{\rm tot}}}{4\beta}, \tag{136}$$

and

$$n_{\rm H_2} = \beta n_{\rm H}^2, \tag{137}$$

[1] The composition of the fluid, y = He/H is the ratio of the number density of helium atoms to the total number density of hydrogen in all chemical compounds.

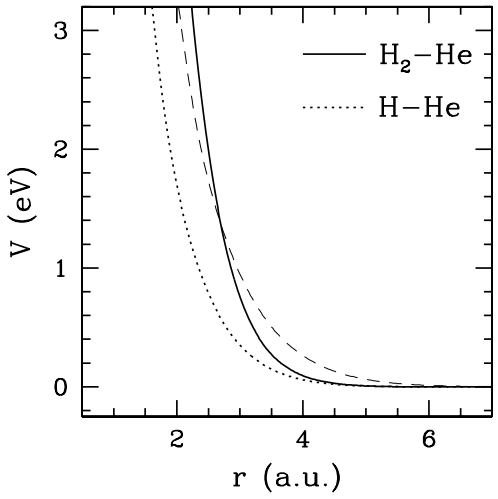

Figure 17: The $H-He$ and H_2-He pair interaction potentials. The dashed line represents the radius (horizontal axis) of a sphere whose volume equals the effective volume of two H atoms colliding with a kinetic energy of $\frac{3}{2}k_BT$ (see text).

where

$$n_{\rm tot} = n_{\rm H} + 2n_{\rm H_2} = \frac{\rho}{m_{\rm H} + ym_{\rm He}} \tag{138}$$

refers to the hydrogen species only.

5.1.2 Computation of the H_2 Dissociation Equilibrium

The non ideal contributions to the chemical potentials of H and H_2 were obtained with a code we wrote to numerically solve the Ornstein-Zernike equation in the Percus-Yevick (PY) approximation (§3.2). For the $H-He$ interaction we use the pair potential of Shalabi et al. (1998), and for the H_2-He interaction the pair potential given by Ree (1983) (Fig. 17). Both potentials are from *ab initio* quantum mechanical calculations and are in good agreement with the independent calculations of Tang & Yang (1990) for $H-He$, and of Tao (1993) and Shafer & Gordon (1976) for H_2-He. As we consider a helium-dominated mixture ($He/H \gtrsim 10^2$), the $H-H$, H_2-H, and H_2-H_2 interactions can be neglected.

High-pressure experiments have shown that *ab initio* pair potentials are too repulsive to describe dense systems where N-body effects become important (Nellis et al., 1984; Ross et al., 1983). The

softening of the pair potentials at high densities can only be quantified experimentally or, alternatively, estimated with N-body quantum mechanical calculations. Because neither are available for mixtures of trace hydrogen in helium, we resort to *ab initio* potentials. The net effect on the dissociation equilibrium depends on the *relative* softening of the potentials (Eq. 134) and is therefore less sensitive to N-body effects than the individual potentials. We also calculated the chemical potentials in the Hypernetted Chain approximation (§3.2) and found them to agree within 5% of the PY values up to $2\,\mathrm{g/cm^3}$. Because the PY approximation is better suited for short range potentials such as the ones we use here, we estimate that our PY calculations are reliable up to at least $2\,\mathrm{g/cm^3}$.

For the internal partition functions Z_{int}, we use expressions for the electronic ground state of the unperturbed hydrogen molecule accounting for the vibrational and rotational excitations (Huber & Herzberg, 1979), and set $Z_{\mathrm{H}} = 2$ for the hydrogen atom. This approximation is justified as the electronic excitation energies of both species are large and for temperatures of a few thousands degrees the populations of the electronic excited levels are extremely small. However, there is significant thermal excitation of the rotational and vibrational levels of H_2 and the effect of the dense medium on $Z_{\mathrm{H_2}}$ must be considered. Since the molecule does not have spherical symmetry, it is possible that its rotation modes will be hindered by interactions with neighbors at very high density. Furthermore, the energies of the vibrational levels, which are spaced by a mere 0.54 eV, could also be significantly shifted by these interactions. Both of these effects are discussed by Saumon & Chabrier (1991) and can be neglected under the present conditions. The use of the unperturbed rotational and vibrational levels of H_2 is thus justified in the calculation of $Z_{\mathrm{H_2}}$.

More importantly, the excited rotational and vibrational levels of the H_2 molecule may be differentially affected by the interactions. This relates to the general problem of the cutoff of the sum over states in the internal partition function and is the subject of an extensive literature. This truncation of the partition function sum is often described by an occupation probability formalism (Hummer & Mihalas, 1988), and, in the case of interactions between neutral particles, is generally described in terms of the volume occupied by each bound state. For a diatomic molecule, the volume occupied increases with the rotational quantum number (centrifugal stretching) and with the vibrational quantum number (larger amplitude of vibration). The first effect is very small and can be

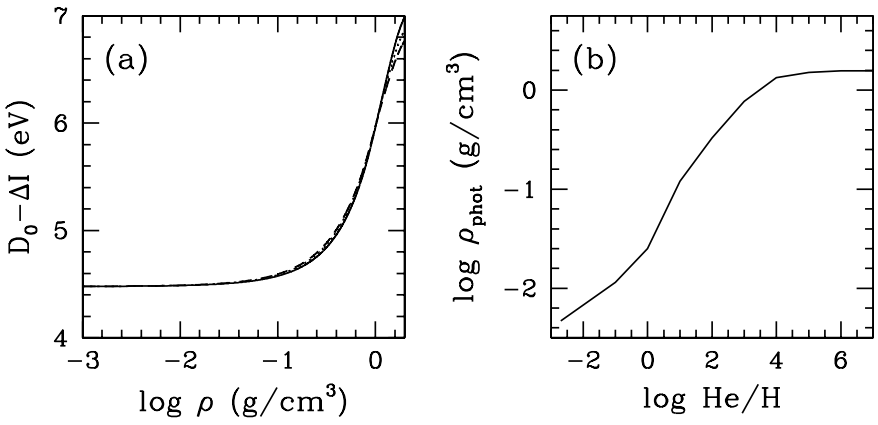

Figure 18: (a) Variation of the effective dissociation energy $D_0 - \Delta I$ as a function of the density of helium for temperatures of 3000 K (solid line), 4000 K (dotted line), and 5000 K (dashed line). (b) The density ρ at the photosphere of atmosphere models of $T_{\rm eff} = 4000$ K, log $g = 8$ (cgs), and range of compositions (by number).

safely neglected. We estimate the vibrational stretching by considering the change in the equilibrium internuclear separation of the molecule with the vibrational quantum number. Because of the anharmonicity of the potential, higher vibrational levels correspond to larger equilibrium separations and a larger average molecular volume. Based on the potential curve of the H_2 molecule (Kolos & Wolniewicz, 1965) we find that for T < 6000 K and densities of up to 2 g/cm^3, the vibrational excitation is largely limited to the lowest five levels and the partition function is reduced by a few percent when the larger volume of the excited states is taken into account. This is a small effect that can be neglected in view of the other uncertainties in the model such as the N-body effects on the interaction potentials. Thus, the use of the internal partition function of the isolated H_2 molecule, with all states being affected identically by the interactions with He (Eq. 135), is a very good approximation.

5.2 Results and Discussion

5.2.1 The H_2 Dissociation Equilibrium in Fluid Helium

In general, ΔI (Eq. 134) is a function of the density of helium and temperature, but is independent of the He/H ratio if hydrogen is a trace species (He/H $\gtrsim 10^2$). For the conditions in white dwarf

atmospheres, the temperature dependence is weak but there is a strong variation with density (Fig. 18a and Table 1). The change in the dissociation energy ΔI is negative, making H_2 more stable in dense helium. This may be qualitatively understood by comparing the effective volume occupied by one H_2 molecule to that of two H atoms in He. Lets assume that these effective volumes are the spaces around each of the particles where the energy of their interaction with He atoms is greater than the average thermal kinetic energy of the particles $\frac{3}{2}k_BT$. This radius is the classical distance of closest approach in a collision. On Figure 17, we plot the radius of a sphere whose volume equals the effective volume of two hydrogen atoms, as a function of k_BT (dashed curve). The corresponding radius for the hydrogen molecule is represented by the $H_2 - He$ potential (solid curve). The effective volume of H_2 is smaller than that of two H atoms for $k_BT \lesssim 1\,\mathrm{eV}$. Since the exclusion of a greater volume results in a decrease of the entropy of He, H_2 is more stable in dense helium than two H atoms. In dense hydrogen, we have the opposite situation where H_2 is less stable at high density (leading to pressure dissociation of H_2) because H_2–H_2 is more repulsive than the sum of the H–H and H–H_2 interactions (Saumon & Chabrier, 1991).

5.2.2 The Dissociation Equilibrium of H_2 in He-rich White Dwarf Atmospheres

The non ideal recombination of H becomes significant when $-\Delta I/k_BT \gtrsim 1$. For an atmosphere with $T_{\rm eff} = 4000\,\mathrm{K}$, this will occur at the photosphere if $\rho \gtrsim 0.3\,\mathrm{g/cm^3}$, a density easily achieved in He-rich models for $\mathrm{He/H} > 10^2$ (Fig 18b). In atmospheres with a lower helium abundance, the photospheric densities are much lower and the dissociation equilibrium is given by the usual Saha relation (Eq. 133). As $D_0 - \Delta I$ increases with increasing helium density, a lower dissociation fraction will result. A strong deviation from the ideal-gas abundance of H_2 is expected.

We have introduced the non ideal correction to the H_2 dissociation equilibrium in our white dwarf atmosphere models. To show the effect, we solved for the chemical composition and the opacity along fixed $T - P$ profiles with $T_{\rm eff} = 4000\,\mathrm{K}$, a gravity of $\log g = 8$ (cgs), and various He/H ratios. Figure 19 shows the atmospheric density profiles. The new abundances of H and H_2 are given in Figure 20 (left panels). As expected, the amount of molecular hydrogen increases significantly

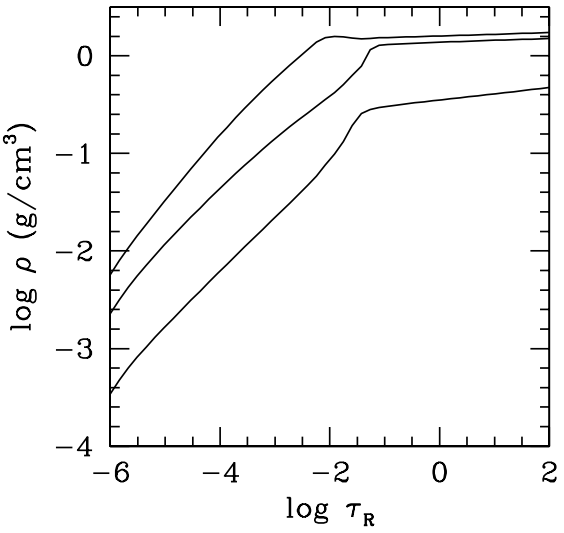

Figure 19: The density profiles of white dwarf atmosphere models of $T_{\rm eff} = 4000\,{\rm K}$, $\log g = 8$ (cgs), and composition of He/H $= 10^6, 10^4$ and 10^2 (from top to bottom, respectively).

throughout the atmosphere for He/H $\gtrsim 10^3$, and H_2 can become the dominant hydrogen species at the photosphere.

The most important sources of opacity in helium-rich white dwarf atmospheres are He^- free-free, Rayleigh scattering, and $H_2 - He$ CIA (Hansen, 2004). The effect of non ideal chemistry on the H_2 dissociation and on the opacity is shown in the right-hand panels of Figure 20. The increase in the number density of molecular hydrogen results in an increase of the $H_2 - He$ CIA opacity. This follows from the linear dependence of $H_2 - He$ CIA opacity on n_{H_2}. On the other hand, the H^- bound-free and free-free opacities are reduced, due to the decrease in the abundance of atomic hydrogen. Based on the atmospheric structures used here, the effects of the non ideal chemistry of H_2 in dense helium are maximal for He/H $\sim 10^3$. This arises from a competition between the need for a high He/H ratio to increase the non ideal effects by increasing the density at the photosphere (Fig. 18b) and the need for a high enough hydrogen content in the atmosphere so that H_2 (or H) contributes to the total opacity (Fig. 20, right-hand side).

The impact of the non ideal dissociation equilibrium of H_2 on the synthetic spectrum of a He-rich white dwarf model is shown in Figure 21. For a white dwarf atmosphere model of $T_{\rm eff} = 4000$K,

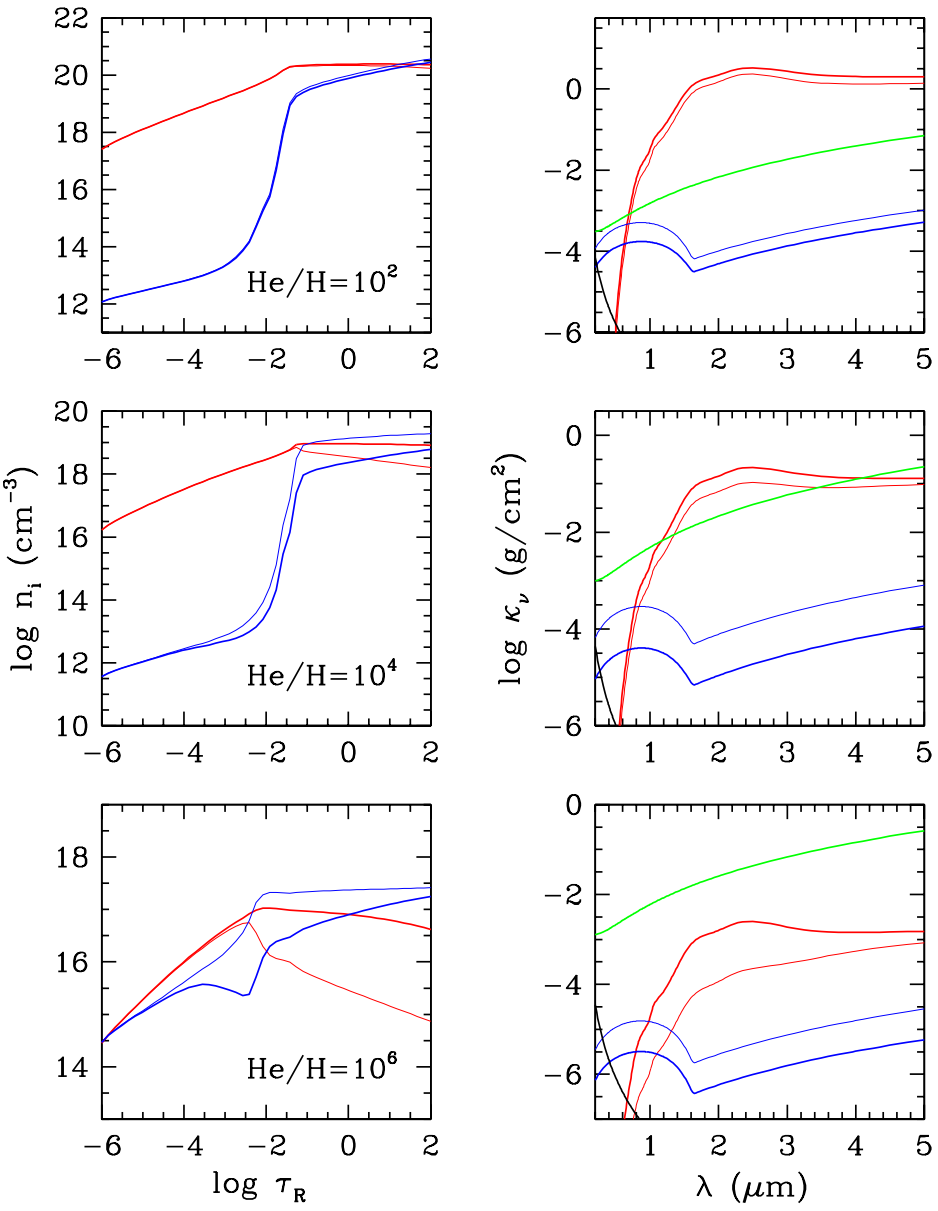

Figure 20: Left panels: The number density of atomic (blue) and molecular (red) hydrogen with (thick lines) and without (thin lines) the non ideal chemical equilibrium along the atmosphere profiles of Fig. 19. Right panels: Corresponding contributions to the photospheric opacity: $H_2 - He$ CIA (red), He^- free-free of Iglesias, Rogers, & Saumon (2002) (green), H^- bound-free and free-free (blue) and Rayleigh scattering (black).

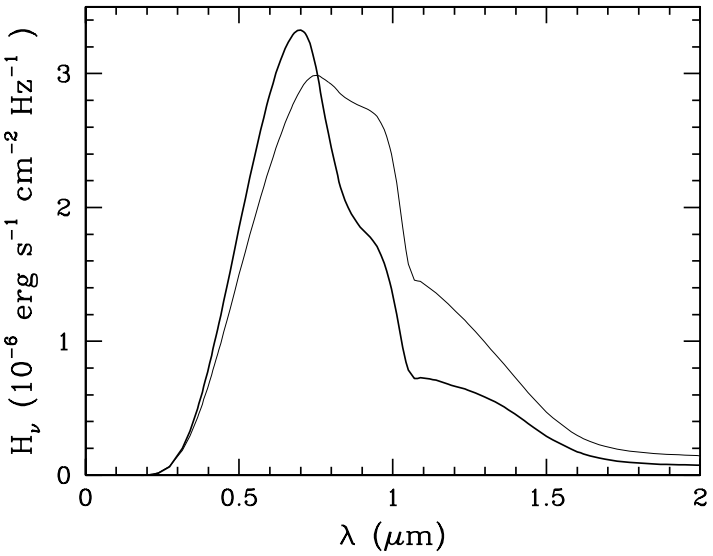

Figure 21: The synthetic spectrum for an atmosphere model of $T_{\rm eff} = 4000\,{\rm K}$, log $g = 8$ (cgs), and ${\rm He/H} = 10^3$ with (thick line) and without (thin line) the non ideal dissociation equilibrium of H_2.

log $g = 8$, and ${\rm He/H} = 10^3$, the rise in abundance of H_2 increases significantly the CIA opacity in the infrared, causing a redistribution of the flux toward shorter wavelengths. This effect on the spectrum of cool white dwarfs is largest for $T_{\rm eff} = 4000{\rm K} - 4500{\rm K}$, where H_2 is partially dissociated. At lower effective temperatures hydrogen exists mostly in molecular form and the effect of the non ideal dissociation equilibrium on the spectrum vanishes at $T_{\rm eff} \sim 3000{\rm K}$.

In the absence of spectral lines of H or He, the determination of the hydrogen abundance in very cool He-rich white dwarfs depends mostly on the relative strength of the ${\rm He} - {\rm H_2}$ CIA, and H^- free-free opacities (Fig. 20, right hand panels). Because the non ideal recombination increases the CIA opacity, this effect, taken by itself, would result in a lower hydrogen number fraction inferred from a given stellar spectrum. On the other hand, we also need to consider revision of the ionization fraction of dense helium which affects the H^- free-free opacity (Chapter VI). However, we emphasize that as the chemical equilibrium (Eq. 135) is not affected by the number of free electrons in the atmosphere, our solution for the non ideal abundance of H_2 will not be affected by weak ionization of He, and the results are limited only by the validity of the ${\rm H_2} - {\rm He}$ and ${\rm H} - {\rm He}$ interaction potentials.

The non ideal dissociation equilibrium in pure hydrogen atmospheres is discussed in Saumon & Jacobson (1999). As hydrogen is much more opaque than helium, the density at the photospheres of these stars is much smaller than in helium-rich atmosphere of the same effective temperature (Fig 5). The non ideal effects are therefore weaker and become important only in stars of lower effective temperatures and/or higher gravity, where high densities are achieved. Saumon & Jacobson (1999) show that interactions matter in pure-hydrogen atmospheres with $T_{\rm eff} \lesssim 2500$K. White dwarfs with hydrogen-rich atmospheres of such low effective temperatures have not yet been identified.

Table 1. The change in the dissociation energy of H_2, $\Delta I(\rho_{He}, T)$ in eV (Eq. 134).

ρ (g/cm^3)	T(K) :	2000	4000	6000	8000
0.001		−0.001	−0.001	−0.001	−0.001
0.010		−0.007	−0.010	−0.011	−0.012
0.100		−0.083	−0.108	−0.120	−0.127
0.250		−0.242	−0.297	−0.323	−0.334
0.500		−0.579	−0.668	−0.697	−0.702
0.750		−1.006	−1.075	−1.088	−1.070
1.000		−1.471	−1.494	−1.469	−1.414
1.500		−2.011	−2.094	−1.963	−1.825
2.000		−2.189	−2.387	−2.192	−1.988

CHAPTER VI

DENSE HELIUM

We saw in Chapter I that because of the low opacity of helium, the highest pressures and densities are encountered in atmospheres of pure He composition. Pure He atmospheres thus represent a limiting case, where dense fluid effects on the EOS, chemistry, and opacity are maximized. We have performed an extensive study of dense helium to account for these effects in our model atmospheres. Despite its astrophysical importance, warm dense helium has received relatively little attention from experimentalists and theorists alike. Experimental data is limited to a few shock compression EOS points below 60 GPa [1] (Nellis et al., 1984) and conductivities at pressures up to ~ 160 GPa (Fortov et al., 2003). In this chapter we investigate the physical properties of warm dense helium under conditions found in the atmospheres of cool white dwarfs using both a statistical physics approach and *ab initio* simulations. The challenge is to calculate the free-free absorption resulting from a very small ($\lesssim 10^{-6}$) but nonetheless crucial fraction of free electrons in a dense fluid. A few large EOS tables that model the regime of pressure ionization have been computed with chemical models (Fontaine et al., 1977; Saumon et al., 1995; Winisdoerffer et al., 2005) but they are poorly constrained in the regime of interest as demonstrated by the broad range of predictions for the density at which helium pressure ionizes (from ~ 0.3 to 10 g/cm^3). We revisit the problem of the ionization of fluid He in the limit of very low ionization ($\lesssim 0.1\,\%$), primarily to estimate the He^- ff opacity more reliably. We extend our calculations to temperatures above the cool white dwarfs regime (up to $T \sim 17000$ K) to compare with experimental conductivities and to explore more completely the properties of fluid helium.

First, we describe classical corrections to the cross sections of Rayleigh scattering and He^- ff with the formalism introduced by Iglesias et al. (2002) to account for correlations in a fluid. This formalism represents only one manifestation of dense fluid effects, however, and we have concluded a more comprehensive study. In particular, because the He^- ff opacity depends on the density

[1] 1 GPa=0.01 Mbar=10^{10} dyn/cm^2

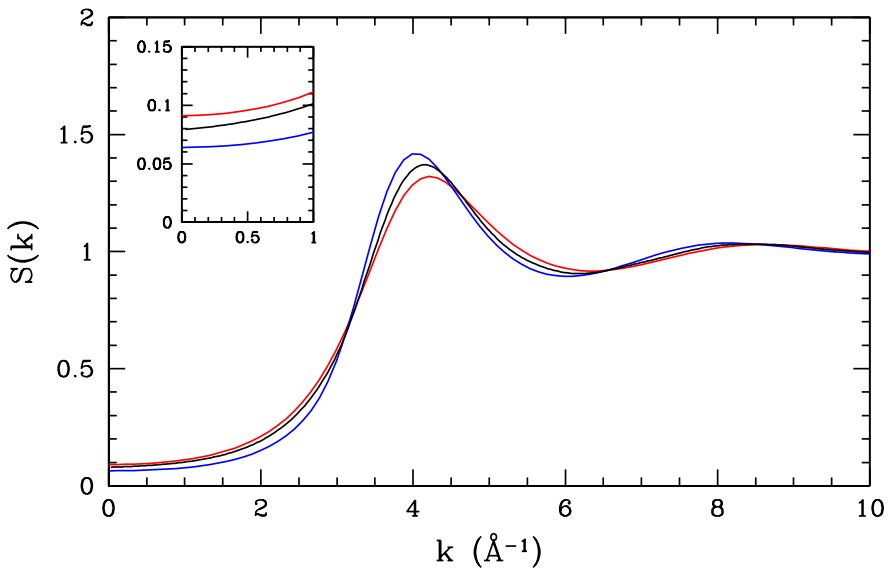

Figure 22: The structure factor of helium at $\rho = 1.2\,\mathrm{g/cm^3}$ and $T = 4000\,\mathrm{K}$. The colors indicate the structure factor obtained with HNC (red), PY (blue), and classical Monte Carlo (black). The figure in the corner shows an enlargement of the $k \sim 0$ region.

of free electrons, which is difficult to evaluate, we use a state-of-the-art density functional theory coupled with quantum molecular dynamics (QMD-DFT) simulations of dense helium to obtain a better estimate of the ionization fraction. This method also gives the free-free absorption coefficient with full quantum mechanical treatment (beyond the correction of Iglesias et al. (2002)). Finally, we estimate the density of free electrons with a completely independent approach based on a new chemical model for the calculation of the chemistry of dense helium. Part of this work, reported in §6.2.1, §6.2.2, and §6.2.3, was performed by Stephane Mazévet of the Theoretical division at the Los Alamos National Laboratory.

6.1 Correlation Effects on Rayleigh Scattering and He^- Free-free Absorption

The correlation effects on the cross section for Rayleigh scattering and He^- ff absorption, the two most important sources of opacity in pure He atmospheres (Fig. 6), have been discussed by

Iglesias et al. (2002) but have never been introduced in white dwarf atmosphere models. In this section we present our calculation of these high-density corrections.

According to Iglesias et al. (2002), because of the density fluctuations described by the structure factor $S(k)$ (Eq. 97), the cross section for Rayleigh scattering in a fluid is

$$\sigma_{\rm sc}(\nu) = \delta_{sc}(\nu)\sigma^0_{\rm sc}(\nu), \tag{139}$$

where

$$\delta_{\rm sc}(\nu) = \frac{3}{8}\int_{-1}^{1} d\mu(1-\mu)(1+\mu^2)S(k), \tag{140}$$

$\sigma^0_{\rm sc}$ is the scattering cross section in the dilute gas limit, ν is the frequency of the scattered radiation, $k = 2\pi\nu n(\nu)\sqrt{2(1-\mu)}/c$, μ is the cosine of the scattering angle, and $n(\nu)$ is the index of refraction.

For the He^- free-free opacity, the corrected cross section in the fluid is

$$\sigma_{\rm ff}(\nu) = \delta_{\rm ff}(\nu)\sigma^0_{\rm ff}(\nu), \tag{141}$$

where

$$\delta_{\rm ff}(\nu) = \frac{g_{\rm ff}(\nu)}{g^0_{\rm ff}(\nu)} \sim \frac{\left(\int_0^\infty dk I(k)\right)}{\left(\int_0^\infty dk I_0(k)\right)}, \tag{142}$$

$g_{\rm ff}$ is a Gaunt factor in the Born approximation that represents the quantum correction to the classical Kramers result (Cox & Giuli, 1968),

$$I(k) = I_0(k)\frac{S(k)}{|\epsilon(k,\nu)|^2}, \tag{143}$$

$\epsilon(k,\nu)$ is the dielectric constant, and

$$I_0(k) = \frac{1}{k}\exp\left[-\frac{\hbar^2}{2mk_BT}\left(\frac{k}{2} - \frac{2\pi m\nu}{\hbar k}\right)^2\right]\left|\frac{k^2 V_{\rm e-He}(k)}{4\pi e^2}\right|^2. \tag{144}$$

$V_{\rm e-He}(k)$ is the Fourier transform of the $e-$He interaction potential. For the physical conditions in He-rich white dwarf atmospheres and the wavelengths of interest ($h\nu \lesssim 3\,{\rm eV}$, $k \approx 2\pi\nu/c = 2\pi/\lambda \lesssim$

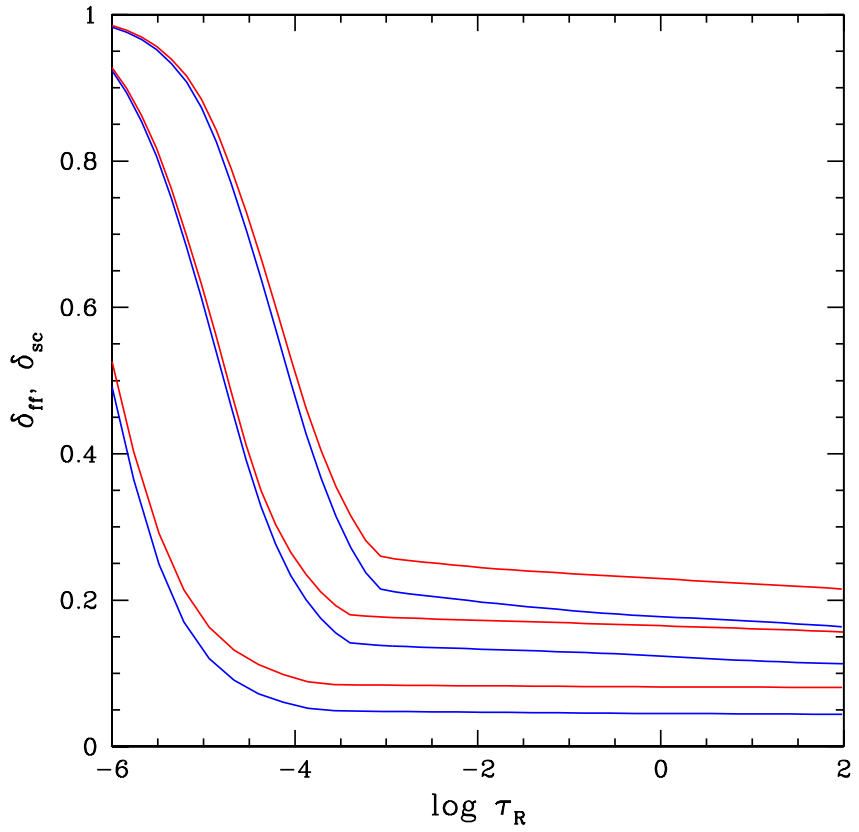

Figure 23: The strength of the correlation effects on the Rayleigh scattering (red) and He^- ff (blue) cross sections at $\lambda = 1\,\mu$m in pure He atmosphere models of $T_{\rm eff} = 6000\,$K, 5000 K, and 4000 K (from top to bottom). The gravity is $\log g = 8$.

$0.01\,\text{Å}^{-1}$), the above relations for the cross sections are reduced to

$$\sigma_{\rm sc}(\nu) \sim S(0)\sigma^0_{\rm sc}(\nu) \tag{145}$$

and

$$\sigma_{\rm ff}(\nu) \sim \frac{S(0)}{|\epsilon(k,\nu)|^2}\sigma^0_{\rm ff}(\nu). \tag{146}$$

These results are consistent with previous estimates by Fortov & Iakubov (2000) and Jackson (1987).

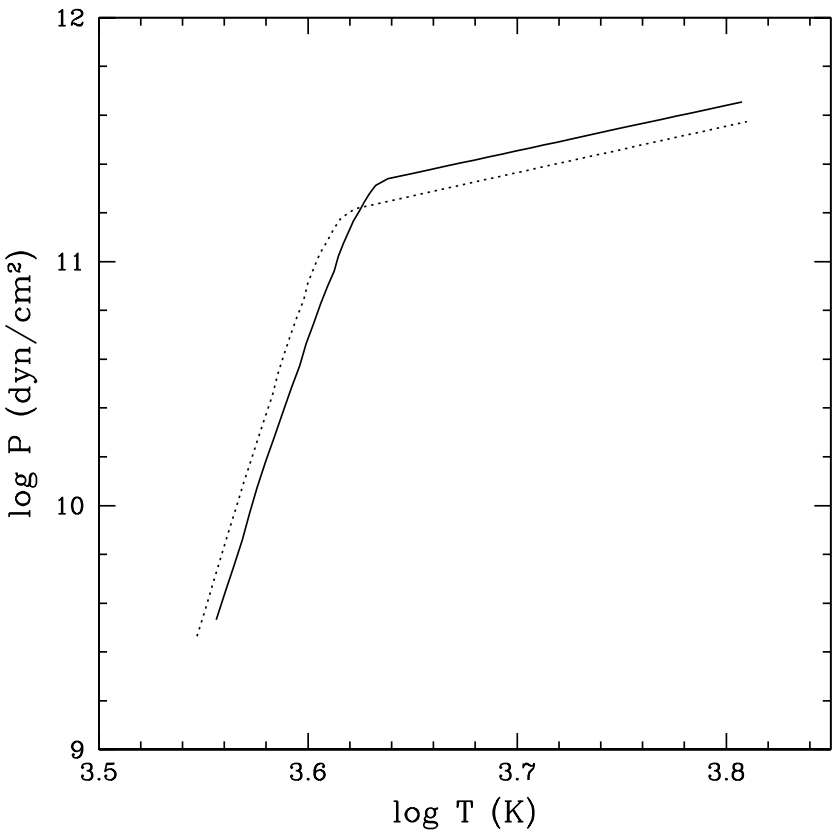

Figure 24: The $P-T$ profile of atmosphere models of $T_{\rm eff} = 5000\,{\rm K}$ calculated with (solid line) and without (dotted line) the correlations effects on the Rayleigh scattering and He^- ff opacities. The gravity is $\log g = 8$.

To obtain the best possible value for the structure factor that enters Eqs. (140)–(146), we conducted classical Monte Carlo (MC) simulations of dense helium with the effective pair interaction potential of Ross & Young (1986). To conduct the simulations we used the code of Allen & Tildesley (1987). 400 atoms were used in the simulation box with the periodic boundary conditions (§3.3) and calculations were conducted for $1000\,{\rm K} < T < 20000\,{\rm K}$ and $10^{-3}\,{\rm g/cm^3} < \rho < 3\,{\rm g/cm^3}$. Figure 22 compares the structure factors obtained from the MC simulations and by solving the Ornstein-Zernike equation in both the HNC and PY approximations (§3.2). For example, at 4000 K and

$1.2\,\mathrm{g/cm^3}$, $S(0) = 0.079$ in the MC simulations, 0.091 with HNC, and 0.064 with PY. The MC simulations are more accurate than the fluid theory methods by $\sim 20\%$.

Figure 23 presents the effects of correlations on the Rayleigh scattering and the He^- ff opacity inside pure helium atmosphere models. Both cross sections are reduced by a factor of 5 to 10, depending on $T_{\rm eff}$, through most of the atmosphere. As a consequence of the hydrostatic equilibrium (Eq. 3), this lowering of the opacity increases the atmospheric pressure (Fig. 24), which makes the non ideal effects even stronger.

6.2 Quantum Molecular Dynamics Simulations

6.2.1 Equation of State

For the quantum molecular dynamics simulations presented here, we used the VASP *ab initio* simulation code (Kresse, 1993). In those simulations nuclei move according to the classical equations of motion (§3.3.1), where forces acting on them are calculated from the electron charge distribution obtained using DFT calculations (§3.5) and the coulomb forces from the other nuclei. The simulations were run for typically 2 ps with time steps ranging from 2 fs for the lowest densities to 0.5 fs at the highest, and using 54 and 128 atoms in the simulation cell. We used the PW91 parametrization of the generalized gradient approximation (GGA) of the density functional (§3.5.3) and the KS orbitals were described with a plane wave basis set.

In Fig. 25, we compare the QMD Hugoniot with the experimental shock compression data of Nellis et al. (1984). The Rankine-Hugoniot equation (Zeldovich & Raizer, 1966)

$$(E_0 - E_1) + \frac{1}{2}(V_0 - V_1)(P_0 + P_1) = 0, \tag{147}$$

describes the shock adiabat through a relation between the initial and final volume, internal energy, and pressure, respectively, (V_0, E_0, P_0) and (V_1, E_1, P_1). For a given V_1, a least squares fit of the QMD values of P_1 and U_1 with a quadratic function in T is used to solve Eq. (147) (Kress, 2001).

While high-pressure experimental data are very sparse, it is reassuring to find that the quantum molecular dynamics (QMD) calculations agree very well with the data as these four experimental points are used extensively to adjust a large majority of helium EOS at high pressures, such as the

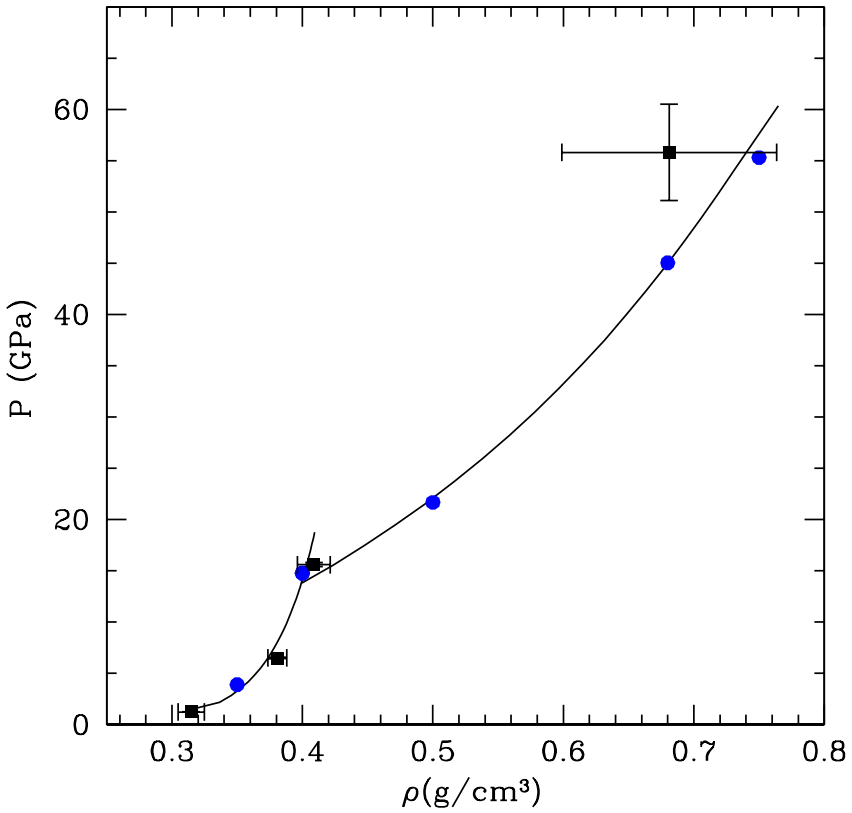

Figure 25: Principal and second shock Hugoniots of helium as a function of density. The experimental data (Nellis et al., 1984) is shown by squares with error bars. Solid dots (blue) show the QMD calculation and the two solid curves represent the first and second shock Hugoniots computed with the chemical model. The latter also guide the eye through the experimental and QMD first and second shock points.

one in our white dwarf atmosphere code. For the principal Hugoniot calculation, the initial condition used is $P_0 = 0\,\mathrm{GPa}$, and $\rho_0 = 0.1245\,\mathrm{g/cm^3}$, based on the experimental conditions. The reference energy point for the QMD calculations is defined as $E_0 = 0\,\mathrm{eV/atom}$, obtained after subtracting the computed internal energy of an isolated He atom in a box of 12 Å from the QMD internal energies. For the principal Hugoniot, the agreement at the highest pressure measured is excellent. For the reshocked points, we used the QMD Hugoniot point obtained at the highest pressure as the initial condition: ρ_1=0.4 g/cm^3, $E_1 = 1.7\,\mathrm{eV/atom}$ and $P_1 = 14.7\,\mathrm{GPa}$. The highest QMD reshocked point calculated also agrees with the experimental measurement within the error bars. However, the QMD

calculations indicate a slightly softer reshock Hugoniot, in agreement with the EOS obtained with our chemical model (§6.3) and independent path integral Monte Carlo *ab initio* simulations (Militzer, 2006).

6.2.2 Optical Properties

We now turn to the principal motivation of the current study that is the calculation of the optical properties of helium at high pressures and for conditions relevant to white dwarf atmospheres. From the QMD trajectories produced, we calculate the electrical properties on a set of configurations using the Kubo-Greenwood formulation (linear response theory) of the optical conductivity, where the real part of the conductivity is given as (Harrison, 1970; Callaway, 1974)

$$\mathrm{Re}\,\sigma(\nu) = \frac{2\pi e^2}{3\nu}\frac{1}{\Omega}\sum_{\mathbf{k}} W(\mathbf{k}) \sum_{n,m} (f_n^{\mathbf{k}} - f_m^{\mathbf{k}}) \left| \left\langle \psi_n^{\mathbf{k}} \left| \vec{\nabla} \right| \psi_m^{\mathbf{k}} \right\rangle \right|^2 \delta(E_m^{\mathbf{k}} - E_n^{\mathbf{k}} - h\nu). \quad (148)$$

In Eq. (148), ν is the frequency, e is the electronic charge, $\psi_n^{\mathbf{k}}$ and $E_n^{\mathbf{k}}$ are the electronic eigenfunctions and eigenvalues for the electronic band n at a given $\mathbf{k}$-point in the Brillouin zone, $W(\mathbf{k})$ is the $\mathbf{k}$-point weight in the Brillouin zone, and $f_n^{\mathbf{k}}$ is the Fermi distribution function. $\vec{\nabla}$ is the velocity operator and Ω the volume of the simulation cell. The matrix elements $\left\langle \psi_n^{\mathbf{k}} \left| \vec{\nabla} \right| \psi_m^{\mathbf{k}} \right\rangle$ are directly related to the dipole matrix elements. The imaginary part of the conductivity is related to the real part by the Kramers-Kronig relation (Jackson, 1987)

$$\mathrm{Im}\,\sigma(\nu) = -\frac{2}{\pi}\mathrm{P}\left[\int_{-\infty}^{+\infty} \frac{\mathrm{Re}\,\sigma(\nu) y}{y^2 - \nu^2} dy\right], \quad (149)$$

where $P[...]$ is the principal value. The real and imaginary parts of the dielectric constant $\epsilon(\omega)$ are (Mazevet et al., 2003)

$$\mathrm{Re}\,\epsilon(\nu) = 1 - \frac{4\pi}{\nu}\mathrm{Im}\,\sigma(\nu), \quad (150)$$

and

$$\mathrm{Im}\,\epsilon(\nu) = \frac{4\pi}{\nu}\mathrm{Re}\,\sigma(\nu). \quad (151)$$

The index of refraction $n(\nu)$ is then

$$n(\nu) = \sqrt{\frac{1}{2}(|\epsilon(\nu)| + \mathrm{Re}\,\epsilon(\nu))} \tag{152}$$

and the absorption coefficient $\alpha(\nu)$ is given by

$$\alpha(\nu) = \frac{4\pi}{n(\nu)c}\mathrm{Re}\,\sigma(\nu). \tag{153}$$

Additional details on this type of calculation can be found in Mazevet (2004).

We show in Fig. 26 the variation of the index of refraction $n(\nu)$ and the absorption coefficient $\alpha(\nu)$ as a function of frequency ν for two temperatures and densities. The QMD calculations agree very well in the density dependence of the index of refraction calculated with a virial expansion (Appendix A). The largest difference between the two calculations appears at $2\,\mathrm{g/cm^3}$ and $T = 2000\,\mathrm{K}$, where the virial expansion shows a stronger temperature dependence than the QMD calculation. We also compare the QMD-DFT absorption coefficients with a typical He^- free-free opacity calculation used in modeling the atmospheres of cool white dwarf stars (Bergeron et al., 1995a). The latter uses the dilute gas He^- free-free cross section (Bell et al., 1982) based on standard electron scattering calculations. The free electron density that enters the He^- free-free opacity is obtained from a chemical EOS for helium that includes only interactions between He atoms (Bergeron et al. (1995a), see §6.3). Figure 26 shows two significant differences between the two calculations. First, the absorption coefficients differ by several orders of magnitude. This difference is a direct consequence of the huge difference between the number density of free electrons in the chemical model and in the fraction of electrons in the conduction band of the QMD-DFT calculation. These two quantities are equivalent concepts within their respective models. The strong density dependence of the absorption coefficient calculated from the chemical model indicates strong pressure ionization effects at $\rho \sim 2\,\mathrm{g/cm^3}$. Second, the frequency dependence of the absorption coefficient is noticeably different. The QMD-DFT calculation shows a nearly flat, Drude-like behavior typical of solids and the dilute gas He^- free-free cross section diverges rapidly at low frequencies. At $T = 2000\,\mathrm{K}$, the standard He^-

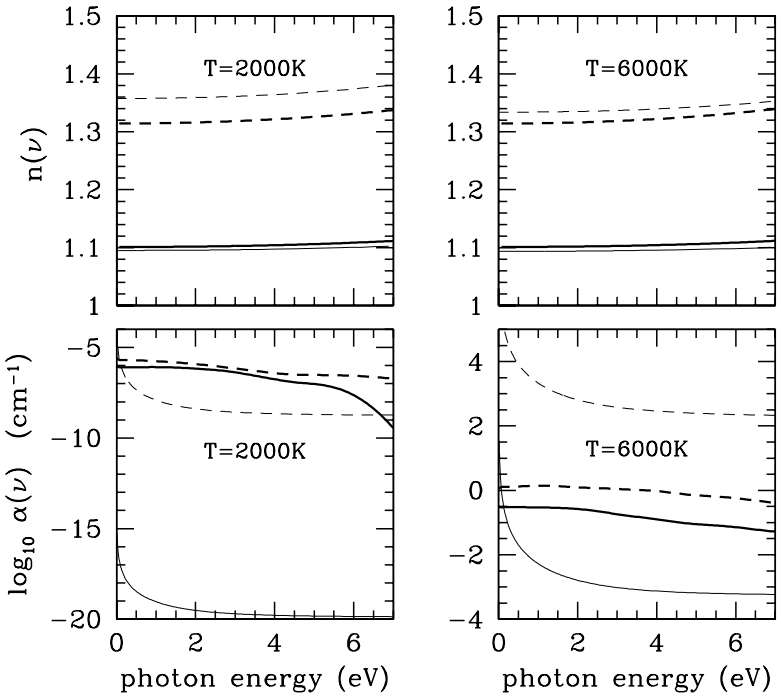

Figure 26: Comparison between the index of refraction and the absorption coefficient obtained with QMD-DFT with other calculations for two temperatures and $\rho = 0.5$ (solid curves) and $2\,\mathrm{g/cm^3}$ (dashed curves). The QMD calculations are shown with thick lines. The QMD-DFT index of refraction is compared with a semi-empirical virial expansion (thin lines, Eq. 204). The absorption coefficient is compared to the He^- free-free absorption commonly used in modeling white dwarf atmospheres of pure helium composition (thin lines, Bergeron et al. (1995a)).

free-free opacity is 2 to 13 orders of magnitude lower than that of the QMD-DFT simulations for $0.5 \leq \rho \leq 2\,\mathrm{g/cm^3}$. At higher temperature ($T = 6000\,\mathrm{K}$), the discrepancy is smaller, about 2 orders of magnitude. On the other hand, it is well known that the GGA-DFT overestimates the ionization fraction and therefore the free-free opacity. This deficiency is related to an underestimation of the band gap (similar to the ionization energy, in this model) in DFT-GGA calculations and is discussed in the next section below.

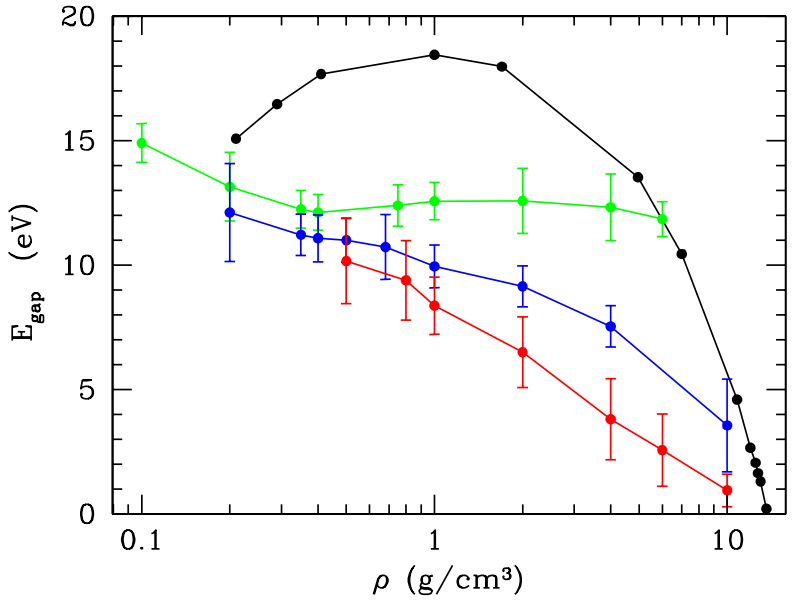

Figure 27: GGA band gap as a function of density for (from top to bottom) the T=0 fcc solid (black), and fluid QMD simulations at temperature $T_i = T_e = 0.52\,\mathrm{eV}$ (green), 1.5 eV (blue) and 3 eV (red), where T_i and T_e are the ion and electron temperatures, respectively.

6.2.3 GGA Band Gap

At normal conditions, helium in the ground state is an insulator with a rather large HOMO-LUMO band gap ($\sim 20\,\mathrm{eV}$), which is defined as the energy difference between the highest occupied orbital and the lowest unoccupied orbital at $T = 0$. Figure 27 shows the variation of the KS band gap as a function of density and temperature as obtained with the QMD-DFT simulations (GGA functional). For a regular fcc lattice at $T = 0$, the method predicts that the He band gap closes at a density of $13.5\,\mathrm{g/cm^3}$ in agreement with previous LMTO calculations (Young et al., 1981). At finite temperature, the KS band gap shown in Figure 27 is obtained by averaging the energy difference of the eigenstates on either side of the Fermi energy along the trajectory. This is equivalent to the HOMO-LUMO gap. Figure 27 shows the KS band gap obtained at finite temperature that appears in Eq. 148. At low temperatures (0.5 eV), the KS band gap obtained from the simulations is almost constant up to $6\,\mathrm{g/cm^3}$, which is reflected in the weak density dependence of the absorption

coefficient (Fig. 26). At higher temperatures, the band gap diminishes as a function of both density and temperature with a closure of the band gap predicted somewhat above $10\,\mathrm{g/cm^3}$. The band gap of fluid helium is smaller than for the solid fcc structure as a result of increased disorder.

At low densities, the gap tends to a value of about 15 eV. For the isolated atom, calculation of the first excited state gives a value of 15.8 eV using either the PW91 or the PBE functionals (§3.5.3). The experimental value for the energy of the first excited state of He is 19.82 eV above the ground state. It is well known that the DFT method, which is a ground state approach not suited for handling excited states, systematically underestimates band gaps, usually by $\sim 50\%$ (Johnson & Ashcroft, 1998). This deficiency of DFT methods is related to the discontinuity in the exchange-correlation potential (Vyrdov & Scuseria, 2005; Johnson & Ashcroft, 1998; Perdew & Levy, 1997), which is present even if the exact F_{HK} functional is used in Eq. (116) (Godby & Schluter, 1986). For open shell atoms, this discontinuity causes the eigenvalue of the highest occupied KS level to approximate the average of the ionization energy (I_p) and of the electron affinity (E_A) (Vyrdov & Scuseria, 2005; Perdew & Levy, 1997) rather than the ionization energy. Usually, $I_p >> E_A$ for atoms, leading to a $\sim 50\%$ underestimation of I_p and of the HOMO-LUMO band gap. Thus, the excited state energies $E_m^{\mathbf{k}}$ used in Eq. (148) are underestimated, resulting in a significant overestimation of the number density of electrons in the conduction band and the free-free opacities. For semi-conductors and insulators (like helium), the eigenenergies need to be corrected with more elaborate methods to calculate the electrical properties more reliably (Johnson & Ashcroft, 1998; Onida et al., 2002).

6.2.4 Band Gap Correction: GW Calculation

A powerful method for the correction of the band gap is the GW approximation (Johnson & Ashcroft, 1998). As the VASP code does not support such a calculation, we used the ABINIT code (Gonze et al., 2002, 2005). For this purpose, we generated ion configurations with classical Monte Carlo (MC) simulations of 32 helium atoms interacting with an effective He–He pair potential (Ross & Young, 1986). This results in significant savings of computational time compared to generating configurations with full QMD-DFT simulations (e.g. VASP). We have verified that these configurations give the same ion-ion pair correlation function and the same thermodynamics as full

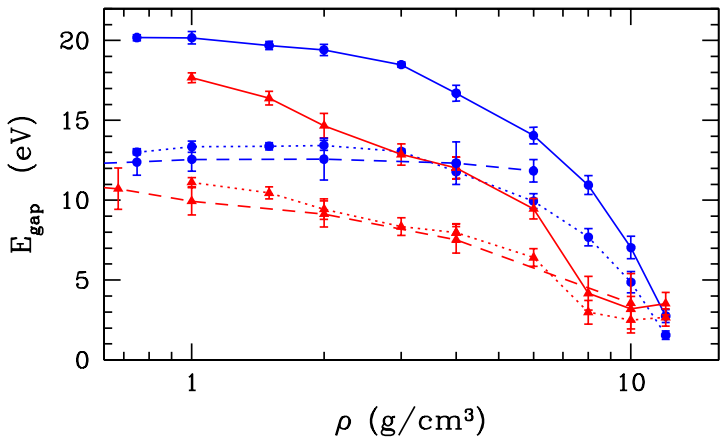

Figure 28: GGA and GW-corrected band gaps for $T = 0.5\,\mathrm{eV}$ (lower curves, red) and $1.5\,\mathrm{eV}$ (upper curves, blue). The ABINIT GGA calculations are shown by the dashed curves, and the GW-corrected band gap by the solid curves. Each point is the average of corrections computed for 9 different ion configurations obtained from classical MC simulations (see text). The dotted lines show the VASP GGA band gap of Fig. 27.

QMD-VASP simulations. This agreement reflects the fact that the He-He effective pair potential gives a very good description of helium up to densities of $\sim 2\,\mathrm{g/cm^3}$. The use of the classical MC configurations as the input for the ABINIT code is validated by the good agreement (better than $1\,\mathrm{eV}$) we obtain for the GGA band gap with that obtained from full QMD simulations conducted with VASP (Fig. 28). Note that the two GGA calculations use different functionals: PBE for ABINIT and PW91 for VASP.

Our GW calculation follows the standard implementation in ABINIT with the PBE functional (GGA). The number of orbitals and the size of the plane wave basis were adjusted to ensure convergence of the PBE-GW band gap to within $0.1\,\mathrm{eV}$. The new band gap at $T = 0.5$ and $1.5\,\mathrm{eV}$ are shown on Fig. 28. At low densities the GW correction is $\sim 6 - 7\,\mathrm{eV}$, and the band gap approaches the correct value for an isolated He atom, $19.82\,\mathrm{eV}$. The band gap with GW correction is $\sim 50\%$ larger than the KS band gap at all densities, which is consistent with the results of similar GGA+GW calculations for semiconductors (Johnson & Ashcroft, 1998). For insulators like helium, the wider

gap results in a lower number density of electrons in the conduction band, approximatelly given by

$$\frac{n_e^{GGA+GW}}{n_e^{GGA}} = \exp\left(\frac{-\Delta E}{2k_B T}\right), \tag{154}$$

where $\Delta E = E_{\rm gap}^{GGA+GW} - E_{\rm gap}^{GGA}$. For the physical conditions of Fig. 26, the number density of conducting electrons is reduced by a factor of $\sim 10^{-3}$ at $T = 6000\,\mathrm{K}$ and $\sim 10^{-9}$ at $T = 2000\,\mathrm{K}$. When corrected by these factors, the QMD-DFT opacities shown in Fig. 26 still differ from the He^- ff opacity commonly used in white dwarf atmosphere models.

6.3 Chemical Model

Ab initio simulations are powerful tools to tackle complex problems that have no other known method of solution. However, they are computationally very expensive, and the simulations presented here represent the most exhaustive such study of He conducted to date. Yet, it is not sufficient to compute atmosphere models. The alternative method to compute thermodynamics and the populations of species needed to compute the opacity is a chemical model. All stellar atmosphere codes use some implementation of a chemical model, where the existence of definite species of atoms, ions, and molecules is assumed a priori. While chemical models are not based on fundamental particles (nuclei and electrons) and interactions (Coulomb), they are very versatile, computationally inexpensive, and can eventually be adjusted to fit data or *ab initio* results. In addition, the very low-ionization regime in the atmospheres pushes the QMD-DFT method to its limit of reliability for computing opacities.

6.3.1 Ionization Equilibrium of Fluid Helium

For these reasons, we developed a chemical model for the ionization of He in the limit of very low ionization fraction ($\lesssim 0.1\%$). This condition is satisfied for $T \lesssim 1.5\,\mathrm{eV}$ and $\rho \lesssim 1.6 - 2.0\,\mathrm{g/cm^3}$ (depends of T). The chemical model includes the contributions from the species He, He^+, He_2^+, and e.

For given T and ρ, the chemical equilibrium abundances are subject to the constraints of charge

neutrality

$$n_e = n_{\mathrm{He}^+} + n_{\mathrm{He}_2^+} \tag{155}$$

and mass conservation

$$\rho = \sum_i n_i m_i. \tag{156}$$

For our system of 4 species, the chemistry can be described by 2 reactions

$$\mathrm{He} \leftrightarrow \mathrm{He}^+ + e \tag{157}$$

and

$$\mathrm{He}_2^+ \leftrightarrow \mathrm{He} + \mathrm{He}^+. \tag{158}$$

Chemical equilibrium is obtained when (§3.4)

$$\mu_{\mathrm{He}} = \mu_{\mathrm{He}}^+ + \mu_e \tag{159}$$

and

$$\mu_{\mathrm{He}_2}^+ = \mu_{\mathrm{He}} + \mu_{\mathrm{He}}^+. \tag{160}$$

Using explicit expressions for the μ_i, Eqs. (159– 160) lead to

$$\frac{n_{\mathrm{He}}}{n_{\mathrm{He}}^+ n_e} = \frac{Z_{\mathrm{He}}}{2Z_{\mathrm{He}^+}} \left(\frac{2\pi\hbar^2}{kT}\right)^{3/2} \left(\frac{m_{\mathrm{He}}}{m_e m_{\mathrm{He}^+}}\right)^{3/2} \exp\left(\beta[I_1 - \mu_{\mathrm{He}}^{nid} + \mu_{\mathrm{He}^+}^{nid} + \mu_e^{nid}]\right) \tag{161}$$

and

$$\frac{n_{\mathrm{He}_2}^+}{n_{\mathrm{He}}^+ n_{\mathrm{He}}} = \frac{Z_{\mathrm{He}_2^+}}{Z_{\mathrm{He}^+} Z_{\mathrm{He}}} \left(\frac{2\pi\hbar^2}{kT}\right)^{3/2} \left(\frac{m_{\mathrm{He}_2^+}}{m_{\mathrm{He}} m_{\mathrm{He}^+}}\right) \exp\left(\beta[I_1 - I_2 - \mu_{\mathrm{He}\ 2}^{nid+} + \mu_{\mathrm{He}^+}^{nid} + \mu_{\mathrm{He}}^{nid}],\right) \tag{162}$$

respectively, where $\beta = 1/kT$.

Because of the very high-ionization energies of He and He^+ compared to our temperature range of $T \lesssim 1\,\mathrm{eV}$, their internal partition functions are very well approximated by their ground states only

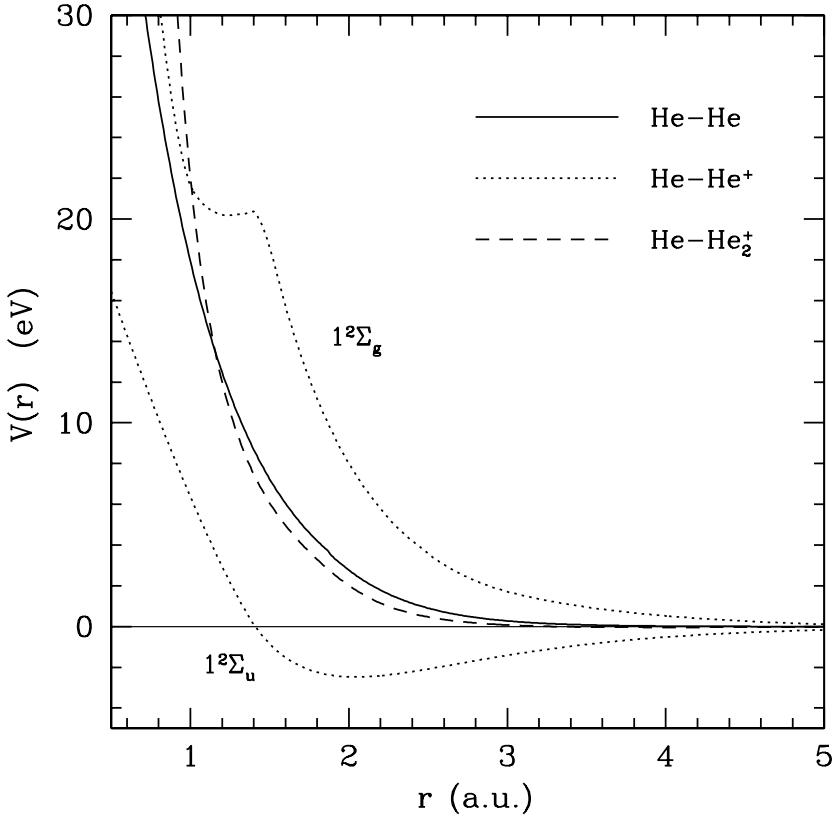

Figure 29: Pair potentials used in the chemical model. For the He – He^+ potential, both the bonding ($1^2\Sigma_u$) and the antibonding ($1^2\Sigma_g$) states are shown.

($Z_{\rm He} = 1$ and $Z_{\rm He^+} = 2$). For He_2^+, we use the partition function of Stancil (1994). The energy of the ground state of each species relative to that of He is $I_1 = 24.5874\,$eV for He^+ and $I_2 = 22.222\,$eV for He_2^+ (Huber & Herzberg, 1979).

For a given pair interaction potentials between the species He, He^+, He_2^+ and He, the pair distribution function, the excess chemical potential, and other thermodynamic quantities are obtained by solving the Ornstein-Zernike equation in the Percus-Yevick approximation (§3.2).

6.3.2 Interaction Potentials

The He-He interactions, which dominate the thermodynamics of the chemical model, are described by an effective pair potential (Ross & Young, 1986), as in our previous calculations. The

He–He_2^+ pair potential is based on *ab initio* quantum mechanical calculations (Scifoni et al., 2004) and a spherical average of its angular dependence is performed prior to calculating $\mu^{nid}_{He_2^+}$. The pair potentials are shown in Fig. 29. The remaining two interaction potentials that enter the chemical model require more attention.

He–He^+

Quantum mechanical calculations of the He–He^+ dimer show that there are two interaction curves that lead to ground state He and He^+ at large separations, the $1^2\Sigma_u$ state (bonding) and $1^2\Sigma_g$ state (antibonding). Both states have a multiplicity of 2. Scattering experiments (Marchi & Smith, 1965; Olson et al., 1967) show that averaging the two potentials is representative of the interaction only for $T > 1\,\mathrm{keV}$, well above the regime of interest. At lower temperatures, both potentials must be considered for the He–He^+ interaction. We have therefore modeled the interaction of a He^+ ion surrounded by He atoms by considering that 1/2 of the He atoms will interact with the $1^2\Sigma_u$ potential curve and 1/2 with the $1^2\Sigma_g$ potential curve (Fig. 29).

The $He - He^+$ interaction potential should be corrected at high densities for many-body effects, such as those that lead to the effective $He - He$ potential (see also the discussion in §5.1.2). Because the $He - He^+$ is stronger than the other pair interactions in the system (Fig. 29), we can expect the many-body correction to be larger. Unfortunately, there are no experimental data or calculations to estimate the softening of the $He - He^+$ potential at high densities and the only choice at present is to use the *ab initio* potentials for isolated pairs.

He-e

It is common practice in chemical models to describe the interaction between electrons and atoms with a polarization potential (Kraeft et al., 1986), which is attractive at long range. A hard cutoff may be introduced to provide short range repulsion (Ebeling et al., 1988; Saumon & Chabrier, 1992; Winisdoerffer et al., 2005). While the polarization potential is adequate at low densities and large separations, low-energy scattering experiments (Kestner et al., 1965) show that the effective local He–e potential, while repulsive at short range, is more complex than a simple repulsive wall.

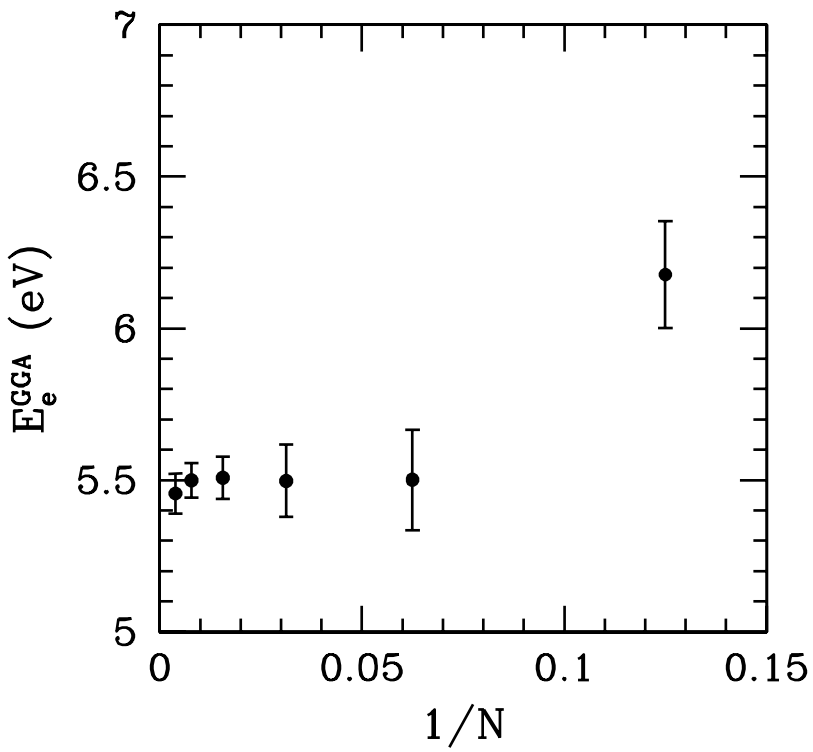

Figure 30: Convergence of the electron energy E_e in dense helium as a function of the number of He atoms N in the simulation. The calculation shown is for $T = 0.5\,\mathrm{eV}$ and $\rho = 1\,\mathrm{g/cm^3}$.

Furthermore, in the low-temperature, high-density regime of interest the electron interactions cannot be treated classically because its thermal wavelength overlaps several He atoms. In view of these difficulties, we have opted for computing the interaction energy of an electron in dense helium with ab initio simulations. For this purpose, we use the density functional theory to compute the electronic structure (§3.5) for a distribution of nuclei from classical Monte Carlo simulations (§3.3.2). We compute the energy difference between two electronic ground state calculations of a simulation box that contains $2N+1$ electrons and one than contains $2N$ electrons, where N is the number of helium nuclei in the box in a fixed configuration.

For this purpose, we generated classical Monte Carlo configurations of $N = 32$ He atoms with the same effective He–He potential as for the input configurations for the GW calculation in §6.2.4.

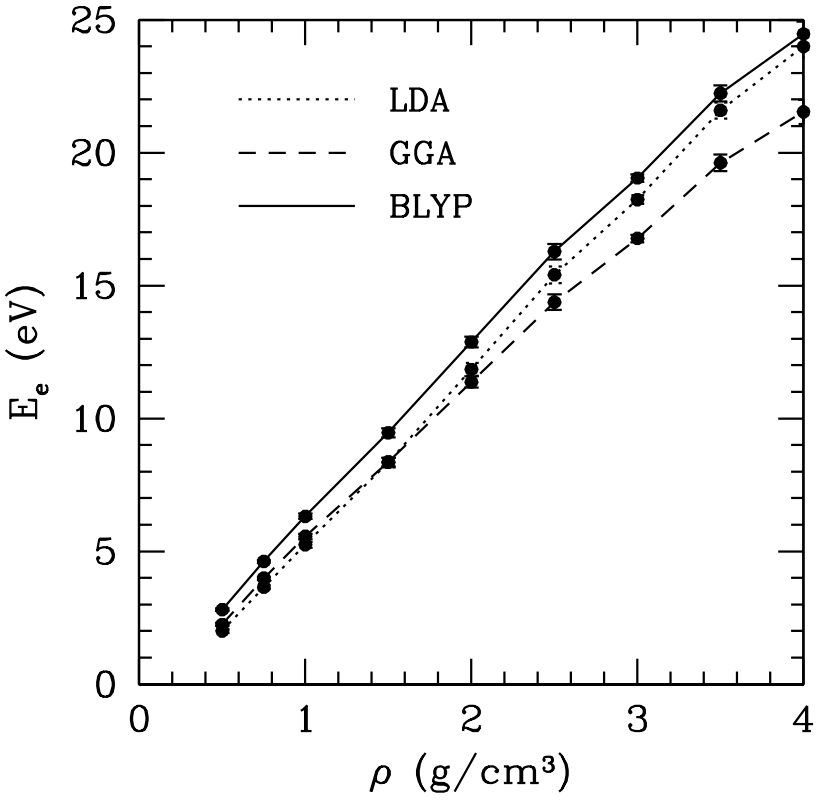

Figure 31: Energy of an electron in dense helium based on DFT calculations. Each curve corresponds to a different calculation: ESPRESSO (BLPY), ABINIT (GGA-PBE) and ABINIT (LDA). All three curves are for $T = 0.5$ eV.

For a fixed configuration of ions, the electronic ground state energy $E_e(2N)$ of the $2N$ electrons is solved with the DFT using periodic boundary conditions. The energy of a free electron in a bath of helium is then given by $E_e = E_e(2N+1) - E_e(2N)$. We take the average of E_e from 9 ion configurations at each temperature and density point. We have verified that $N = 32$ ions give a converged value of E_e to within ~ 0.1 eV by running simulations up to $N = 256$ (Fig. 30). The DFT calculations of E_e were performed with the ABINIT code (Gonze et al., 2002, 2005) with both the LDA and GGA (PBE) density functionals, as well as the ESPRESSO code (Baroni et al., 2006) with the GGA (BLYP) functional, for densities between 0.5 and 4 g/cm^3 and $T = 0$ to 1 eV. All three calculations show that E_e is a linear function of the density of He atoms (Fig. 31). Linear

least squares fits to the three simulations show that they have the same slope within the statistical uncertainties of the simulations. The BLYP functional is known to give better results for electron affinities (Tschumper & Schaefer, 1997). Our calculation with the BLYP functional is the most consistent with the experimental data of Broomall et al. (1976) (obtained at $\rho < 0.2\,\mathrm{g/cm^3}$ and $T < 100\,\mathrm{K}$) and we consider the BLPY calculation as our best estimate of the energy of an electron in dense fluid He.

Finally, we have performed a few full MD-DFT test simulations with VASP to allow the ion configuration to relax in the $2N+1$ electron calculation. The results for E_e agree with the ABINIT-PBE (GGA) calculation to within 0.2 eV. This test also shows that the presence of the additional electron does not affect the configuration of the atoms in this regime, and therefore the excess entropy of the free electron is small compared to the interaction energy. This result is consistent with the interpretation of measurements of the electron mobility in cryogenic helium, where the electron does not form a cavity by repulsion of the He atoms (Schwarz, 1978), which would otherwise result in an entropy term.

The BLPY calculation of $E_e(T, n(\mathrm{He}))$ has been fitted with a linear functional form for $\rho_{\mathrm{He}} > 0.05\,\mathrm{g/cm^3}$. At low densities the energy of an electron in helium is given by the Lenz formula (Tankersley et al., 1973; Broomall et al., 1976)

$$E_{\mathrm{el}}^{\mathrm{Lenz}} = \frac{2\pi\hbar^2 n_{\mathrm{He}} a_{\mathrm{He}}}{m_e} = C_{\mathrm{L}}\rho_{\mathrm{He}}, \tag{163}$$

where $a_{\mathrm{He}} = 0.63\,\text{Å}$ is the e-He scattering length of O'Marley et al. (1978) that reproduces the scattering experiment of Yuan (1988) for $T < 1\,\mathrm{eV}$. Corrections to the Lenz formula are expected for moderate densities of $\sim 0.05\,\mathrm{g\,cm^{-3}}$ (Broomall et al., 1976) so we use a quadratic form that recovers the Lenz formula at very low density and smoothly joins the fit of the DFT-BLYP calculation of $E_e(T, n_{\mathrm{He}})$. The final result is

$$E_e(\rho, T) = 10\alpha(T)\rho^2 + C_{\mathrm{L}}\rho \qquad \rho < \rho_0 \tag{164}$$

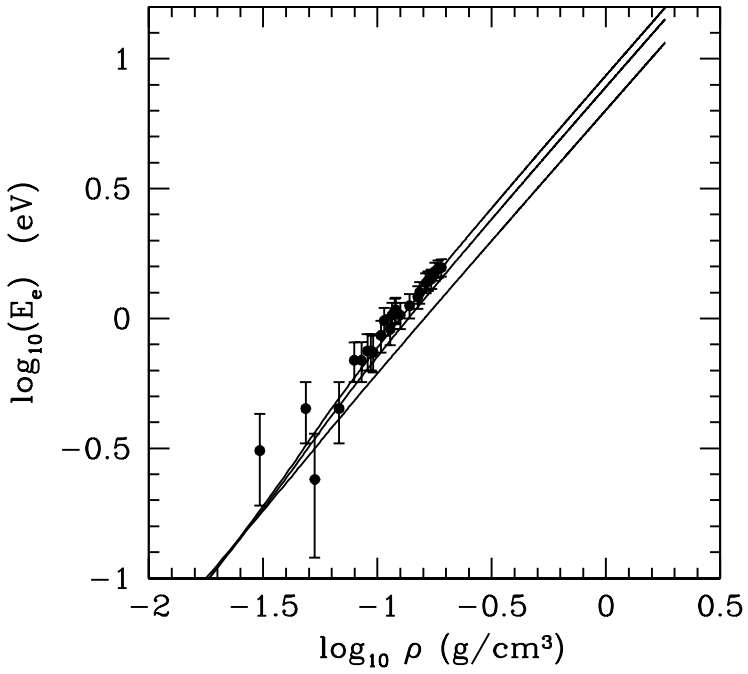

Figure 32: Energy of an electron in helium as a function of density (Eqns. 164 and 165). Each curve corresponds to an isotherm with $T = 10$, 5000, and 10^4 K (from top to bottom). The experimental data was taken in the 10–100 K range (Broomall et al., 1976).

and

$$E_e(\rho, T) = \alpha(T)\rho + 10\alpha(T)\rho_0^2 + (C_{\rm L} - \alpha(T))\rho_0 \qquad \rho \geq \rho_0, \tag{165}$$

where

$$\alpha(T) = a_1 e^{(a_2 T + a_3 T^2)} \sum_{i=0}^{5} b_i T^i. \tag{166}$$

E_e and T are in eV, ρ is in g/cm^3 and the coefficients are given in Table 2.

Isotherms of E_e are shown in Fig. 32. The agreement with the low-temperature data of Broomall et al. (1976) is excellent and the T dependence is weak. We find that E_e is always positive and becomes large for $\rho \gtrsim 0.1\,{\rm g/cm^3}$, which is consistent with the calculations of Boltjes et al. (1993).

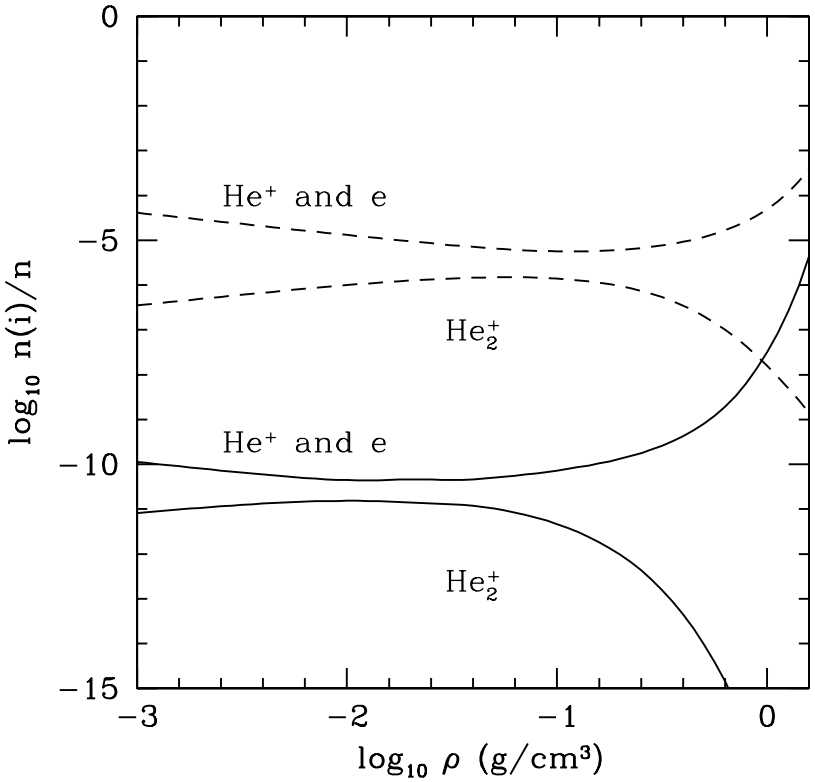

Figure 33: Abundances from the chemical model. The mole fractions n_i/n, where $n = \sum_i n_i$, are shown as a function of density for $T = 0.5$ eV (solid curves) and $T = 1$ eV (dashed curves). Because the electron mole fraction is given by $n_e = n_{\mathrm{He}^+} + n_{\mathrm{He}_2^+}$ and that $n_{\mathrm{He}_2^+} << n_{\mathrm{He}^+}$, the electron mole fraction is indistinguishable from the He^+ curves.

The He–e interaction thus tends to inhibit the pressure ionization of He. Because the presence of free electrons does not affect the distribution of ions, $\mu_e^{nid} \sim E_e$ in Eq. (161).

6.3.3 Abundances and Thermodynamics from the Chemical Model

With the non ideal contributions to the chemical potentials μ_i^{nid} derived above, the chemical equilibrium abundances of each species are obtained by solving Eqs. (155), (156), (159), (160), and all the thermodynamics quantities of interest follow directly. The composition of this interacting helium fluid model is shown in Fig. 33 for two temperatures. The mole fraction of He_2^+ remains below 10^{-6} for $T < 1$ eV. Thus, He_2^+ plays a minor role in the ionization balance of helium, which is

dominated by He^+. The configuration contributions, which are responsible for pressure ionization, become noticeable for $\rho \gtrsim 0.3\,\mathrm{g/cm^3}$. The ionization fraction rises rapidly at higher densities but remains below 0.1% even up to $\rho = 1.5 - 2\,\mathrm{g/cm^3}$ (depending on the temperature). At higher temperatures or densities, the Coulomb interactions between e and He^+ that we have neglected become important and electron degeneracy is no longer negligible.

On the other hand, the thermodynamics of the chemical model is in excellent agreement with the QMD-DFT simulations up to $\rho = 2\,\mathrm{g/cm^3}$. The first and second-shock Hugoniots also agree very well with the experimental data (Fig. 25), and with the QMD-DFT simulations. This result is not surprising because the effective He–He pair potential was adjusted to reproduce the shock data (Ross & Young, 1986). Clearly, in the limit of low ionization for which this model was developed, the thermodynamics is dominated by the contribution of atomic He.

6.3.4 Conductivities from the Chemical Model

Given the ionization equilibrium of the He fluid computed by chemical model, we calculate its electrical conductivity with a simple Drude model

$$\sigma_{\mathrm{DC}} = n_e e^2 / m_e \nu_{\mathrm{eff}}, \tag{167}$$

where the effective collision frequency ν_{eff}, corrected for density effects, is estimated with (Schwarz, 1978; Fortov & Iakubov, 2000)

$$\nu_{\mathrm{eff}} = \nu_{\mathrm{class}}(1 + 2\lambda_{\mathrm{th}}\sigma_{\mathrm{id}} n_{\mathrm{He}}), \tag{168}$$

where

$$\nu_{\mathrm{class}} = \sqrt{\frac{3kT}{m_e}}\sigma_{\mathrm{id}} S(0) n_{\mathrm{He}}, \tag{169}$$

λ_{th} is the thermal de Broglie wavelength of the electrons, $\sigma_{\mathrm{id}} \sim 6\,\mathrm{\AA}^2$ is the $\mathrm{e} - \mathrm{He}$ scattering cross section for the dilute gas (Yuan, 1988), and $S(0)$ is the He–He structure factor to account for correlations (Fortov & Iakubov, 2000; Iglesias et al., 2002).

The term $(1 + 2\lambda_{\mathrm{th}}\sigma n)$ accounts for multiple scattering in a dense medium and is validated by experiments (Schwarz, 1978; Fortov & Iakubov, 2000). Equation (167) is of marginal validity at the

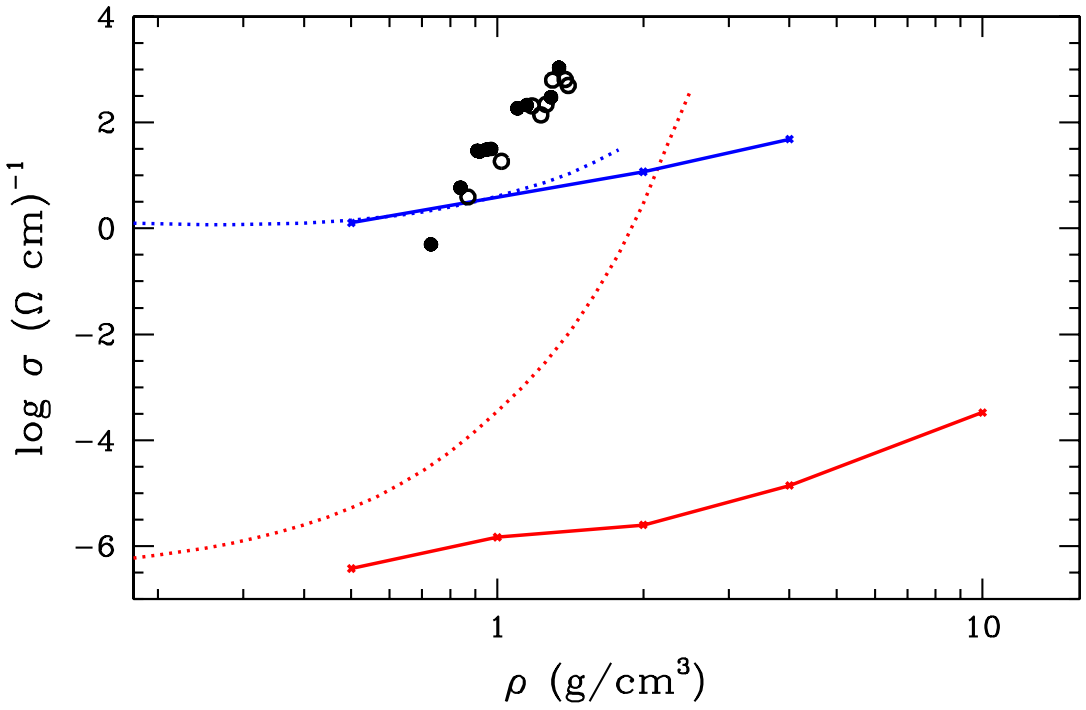

Figure 34: Conductivities from the chemical model (dotted lines) and QMD simulations (solid lines) for $T = 0.5\,\mathrm{eV}$ (red) and $T = 1.5\,\mathrm{eV}$ (blue). Dots represent the measurements of Fortov et al. (2003) at $T < 1.5\,\mathrm{eV}$ (open circles) and $T > 1.5\,\mathrm{eV}$ (filled circles). The experimental uncertainties are $\pm 50\%$ in conductivities and $\pm 10\%$ in densities. Note the lack of correlation between σ and T in the data.

highest densities of interest here. The multiple scattering correction and the $S(0)$ correction become quite large for $\rho \gtrsim 1\,\mathrm{g/cm^3}$, each affecting σ_{DC} by an order of magnitude, but in opposite directions. Other expressions for ν_{eff} in dense fluids are of a heuristic nature and cannot be validated because of the lack of experimental data at these densities.

6.4 A Comparison of Conductivities with Experimental Data

The only measurement of optical properties of helium under conditions similar to those encountered in helium atmospheres are the conductivities of Fortov et al. (2003) obtained under multiple shock compression. We compare experimental conductivities with those computed from QMD simulations and chemical model.

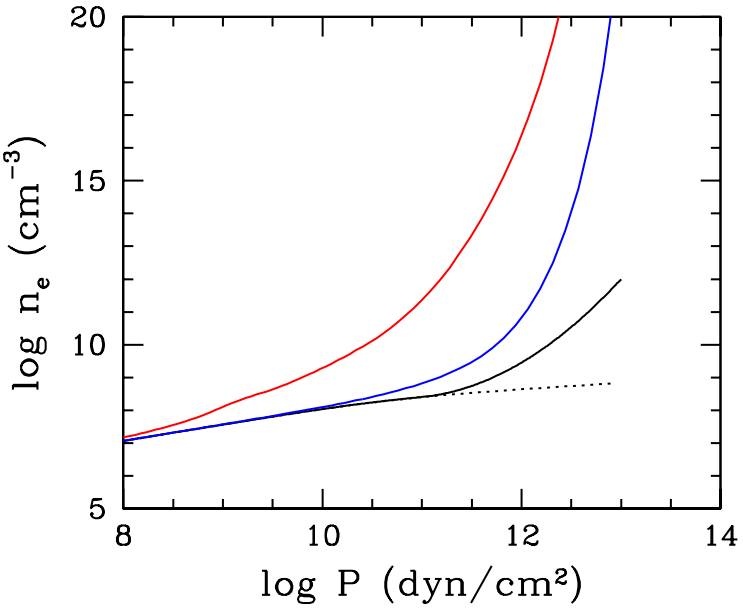

Figure 35: Abundance of free electrons in dense helium at $T = 4500\,\mathrm{K}$ from different models: ideal gas (Saha, dotted), Bergeron et al. (1995a) (black), corrected model of Bergeron et al. (1995a) (blue), and our chemical model (red).

The experimental conductivities cannot be reconciled neither with the *ab initio* QMD nor with the chemical model calculations (Fig. 34). There is a striking disagreement in their density and temperature dependence. The QMD-DFT conductivities show a strong dependence on temperature and a weak dependence on density because the band gap in the QMD simulations remains much larger than $k_B T$ in the regime of interest (Fig. 28).

The differences between the data, the QMD simulations and the chemical model arise principally from the different implied values for the density where pressure ionization occurs in helium. The experimental results can be understood only if the pressure ionization (alternatively, the closing of the band gap) occurs at $\rho \sim 1.4\,\mathrm{g/cm^3}$. The QMD simulations show that the band gap is 15–20 eV at this density (depending on temperature) and helium does not pressure ionizes until much higher densities $\rho \gtrsim 10\,\mathrm{g/cm^3}$. Extrapolating the chemical model conductivities to densities beyond its

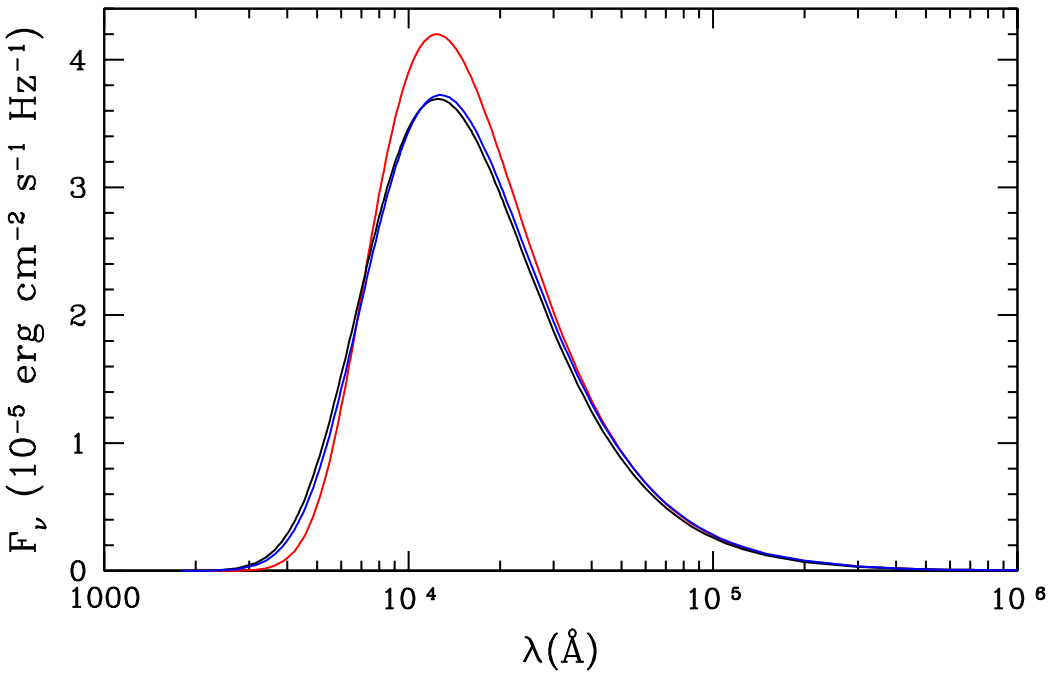

Figure 36: Spectrum of a pure helium atmosphere model of $T_{\rm eff} = 4000\,{\rm K}$ and $\log g = 8$ (blue), of Bergeron et al. (1995a) with the same parameters (red), and of a $T = 4000\,{\rm K}$ black body (black).

region of validity suggests that pressure ionization of He occurs at $\rho \sim 2 - 3\,{\rm g/cm^3}$; about twice the value implied by the experiments, but well below the QMD-DFT predictions.

While the calculations performed here provide useful information for physical models to describe He at conditions found in white dwarf atmospheres, the significant disagreement with the currently available conductivity data calls for additional measurements to firmly establish the ionization fraction of fluid helium and the density where helium becomes pressure ionized. We can use the range of conductivities obtained from our two models as a conservative estimate of the remaining theoretical uncertainty in this difficult regime.

6.5 Implications for White Dwarf Atmosphere Models

In Fig. 35 we present the number density of free electrons calculated by our chemical model compared to the model of Bergeron et al. (1995a), which is typical of models used in current white

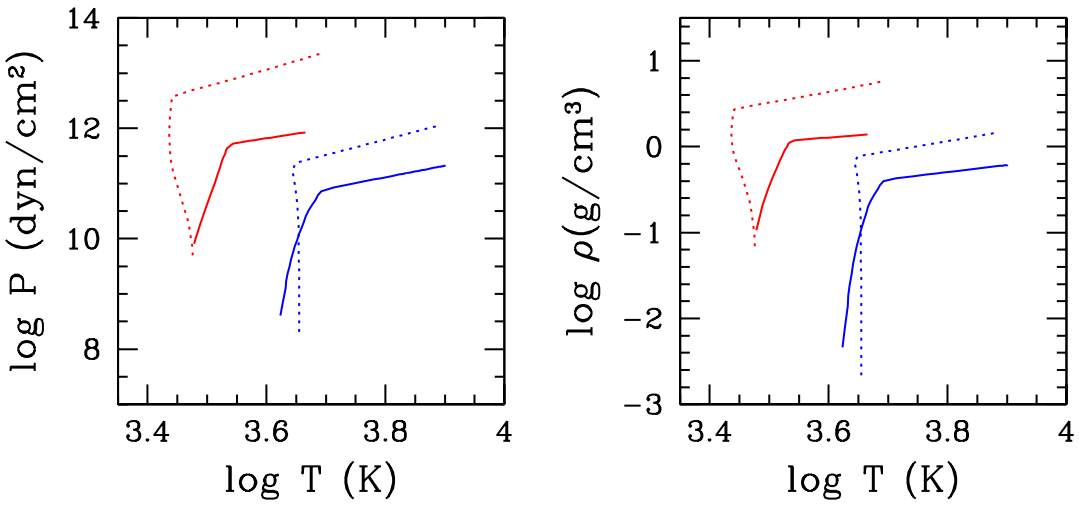

Figure 37: $P-T$ and $\rho-T$ atmosphere profiles of pure He models of $T_{\rm eff}=4000\,{\rm K}$ (red) and $T_{\rm eff}=6000\,{\rm K}$ (blue). Solid lines represents our models while dotted lines are the models of Bergeron et al. (1995a). The gravity is $\log g=8$.

dwarf atmospheres. Bergeron et al. (1995a) use a chemical model similar to ours except that it only includes He – He interactions. This model gives the correct thermodynamics but neglects the strong He – e and He – He^+ interactions that greatly affect the ionization balance. As a result, the abundance of free electrons is a few orders of magnitude larger in our model. Our work has also revealed an error in the implementation of the Bergeron et al. (1995a) chemical model, which further reduces n_e in their models.

Despite our extensive work on the He^- ff opacity of He, its value remains uncertain by $1-2$ orders of magnitude in the regime of interest for cool He atmospheres. Additional experimental data is very desirable, especially in view of the disagreements with both of our models (Fig. 34). On the other hand, a solid conclusion can be reached. The QMD-DFT simulations, the chemical model and the experimental data show that n_e and therefore the He^- ff opacity is orders of magnitude larger than what is used in current atmosphere models (Bergeron et al. (1995a), Fig. 35). Rayleigh scattering becomes negligible in comparison and the nearly grey He^- ff (Fig. 26) is the only opacity that matters. Grey atmospheres have spectra close to black bodies (Fig. 36) that depend only

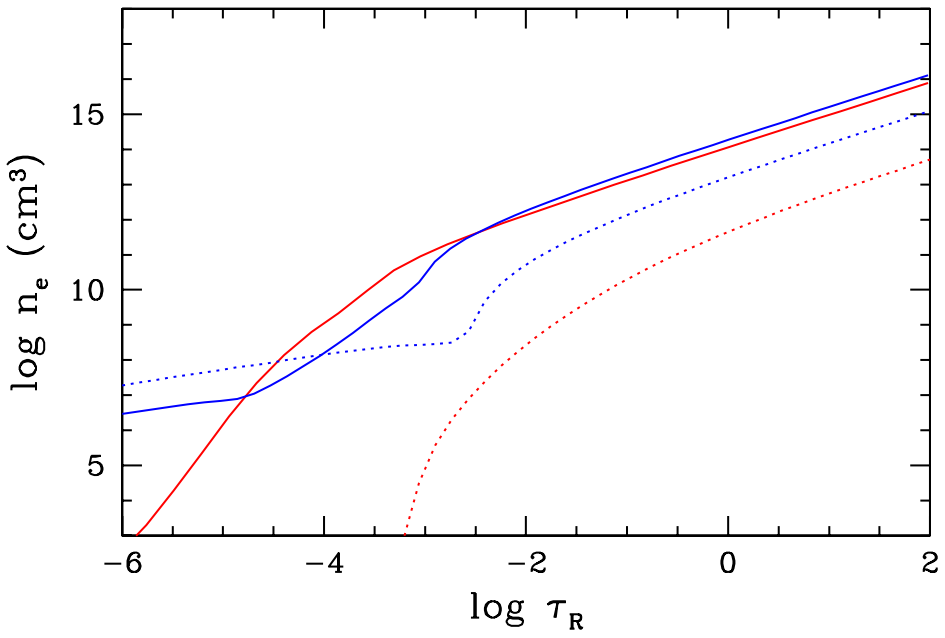

Figure 38: Number density of electrons in the models of figure 37. Colors and line types match those of Fig 37.

on $T_{\rm eff}$, not on gravity. This result is different from the models of Bergeron et al. (1995a), where strong Rayleigh scattering at $\lambda \lesssim 5000$ Å causes redistribution of flux towards longer wavelengths and a significant deviation from a black body spectrum (Fig. 36). Once He^- ff dominates the other opacities, further increases in n_e (i.e. He^- ff) will not affect the emergent spectrum. On the other hand, the $T-P$ structure of the model will depend on the opacity through the equation of hydrostatic equilibrium (Eq. 3). The pressure in a model increases with gravity and decreases with the opacity (see discussion of Fig. 24), which affects the surface boundary condition used in evolutionary calculations of cool white dwarfs and their cooling time scale. Figure 37 shows the $P-T$ and $\rho-T$ profiles in our models and those of Bergeron et al. (1995a). Because the number of free electrons and therefore the He^- ff opacity are significantly larger in our models (Fig. 38), the pressure in our pure-He atmospheres models is about one order of magnitude lower and densities are much smaller.

In our models we use the chemical model for calculating the chemistry of helium. It ensures that we recover the ideal gas limit at low densities and allows for computation of equilibrium chemistry in atmospheres where hydrogen species are also present. For the Rayleigh scattering and He^- ff cross sections, we apply the Iglesias et al. (2002) corrections as described in §6.1.

Table 2. Table of coefficients for the electron affinity (Eqs. 164, 165, 166).

coefficient	value
ρ_0	$0.05\,\mathrm{g\,cm^{-3}}$
C_L	$4.5382\,\mathrm{eV\,cm^3\,g^{-1}}$
a_1	$8.60384\,\mathrm{eV\,cm^3\,g^{-1}}$
a_2	$-4.83886\,\mathrm{eV}^{-1}$
a_3	$1.97586\,\mathrm{eV}^{-2}$
b_0	1.0313
b_1	$2.99678\,\mathrm{eV}^{-1}$
b_2	$10.3747\,\mathrm{eV}^{-2}$
b_3	$2.99498\,\mathrm{eV}^{-3}$
b_4	$-1.27844\,\mathrm{eV}^{-4}$
b_5	$-3.10191\,\mathrm{eV}^{-5}$

CHAPTER VII

STABILITY OF THE NEGATIVE HYDROGEN ION IN DENSE HELIUM

The H^- ion is weakly bound, with an ionization energy of $I^0_{H^-} = 0.754\,\mathrm{eV}$. Its bound-free opacity is the main absorption mechanism at optical wavelengths in white dwarfs atmospheres that are sufficiently enriched in hydrogen (He/H $\lesssim 100$, Fig. 6). It has been suggested that the negative hydrogen ion may be destroyed by pressure ionization in dense helium (Bergeron et al., 1997). In this chapter we address this issue by computing the non ideal ionization equilibrium of H^- using a statistical physics approach (§3.4). The calculations are performed in the same fashion as our solution for the dissociation equilibrium of H_2 (Chapter V) and the ionization equilibrium of helium (§6.3).

7.1 The Non ideal Ionization Equilibrium of H^-

The ionization reaction of the negative hydrogen ion is

$$H^- \leftrightarrow H + e \tag{170}$$

and the ionization equilibrium is given by (§3.4)

$$\mu_{H^-} = \mu_H + \mu_e. \tag{171}$$

Including non ideal effects, Eq. (171) leads to a modified Saha equation

$$\frac{n_{H^-}}{n_H n_e} = \frac{Z_{H^-}}{2Z_H}\left[\frac{h^2}{2\pi m_e k_B T}\right]^{\frac{3}{2}} e^{(I^0_{H^-}-\Delta I)/k_B T} \tag{172}$$

where

$$\Delta I = \mu^{nid}_{H^-} - \mu^{nid}_H - \mu^{nid}_e. \tag{173}$$

For the internal partition functions that enter Eq. (172), we use the ground state values, $Z_H = 2$

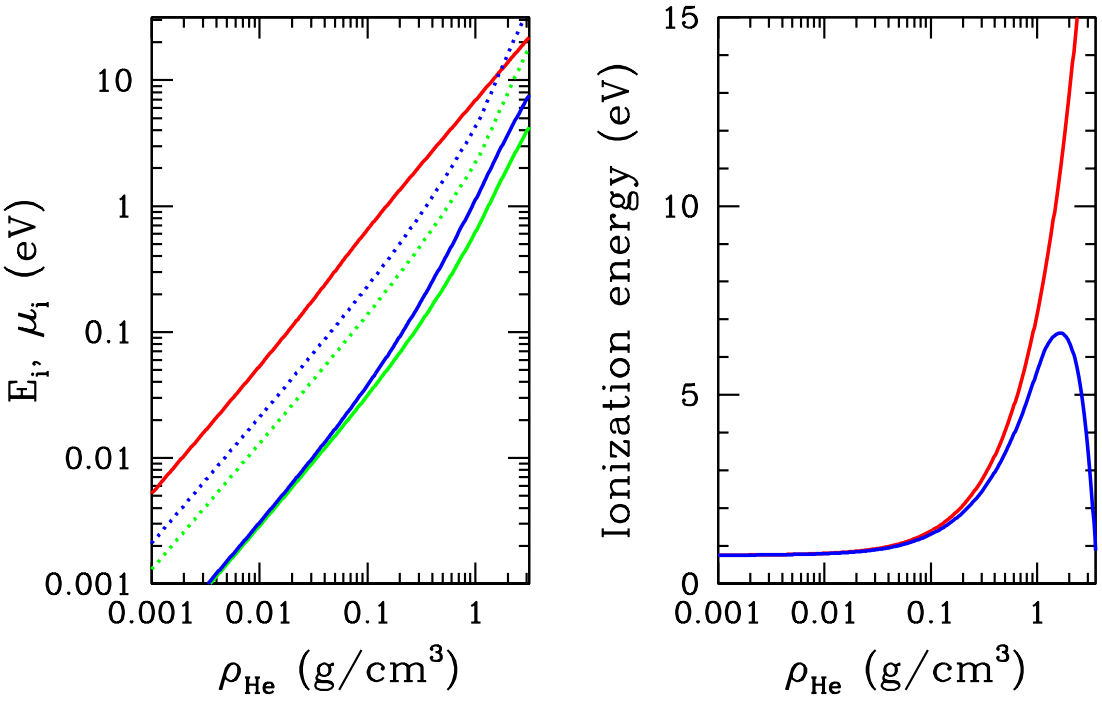

Figure 39: Left panel: The energies (solid lines) and chemical potentials (dotted line) of H (green), H^- (blue), and e (red) in dense helium at $T = 4000\,\mathrm{K}$. Right panel: The effective ionization energy (red) and the photo-ionization energy (blue) of H^- in dense helium.

and $Z_{H^-} = 1$. The calculation of the non ideal chemical potential of electron, μ_e^{id}, was described in §6.3.2. The non ideal chemical potentials of H^- and H are obtained by solving the Ornstein-Zernike equation (Eq. 91) in the PY approximation (§3.2) with *ab initio* interaction potentials for H – He (Kolos & Wolniewicz, 1965) and H^- – He (Shalabi et al., 1998). The term $I^0_{H^-} - \Delta I$ in Eq. (172) can be interpreted as the effective ionization energy that depends on the helium density (Fig. 39). It rises with density, making H^- more stable in fluid helium. The abundance of H^- in a medium of composition He/H = 100 as a function of density is shown in Fig. 40. The non ideal effects on the abundance of H^- increases significantly for $\rho \gtrsim 0.05\,\mathrm{g/cm^3}$. The abundance of H^- is also affected by chemical reactions involving other hydrogen-bearing species and electrons through mass

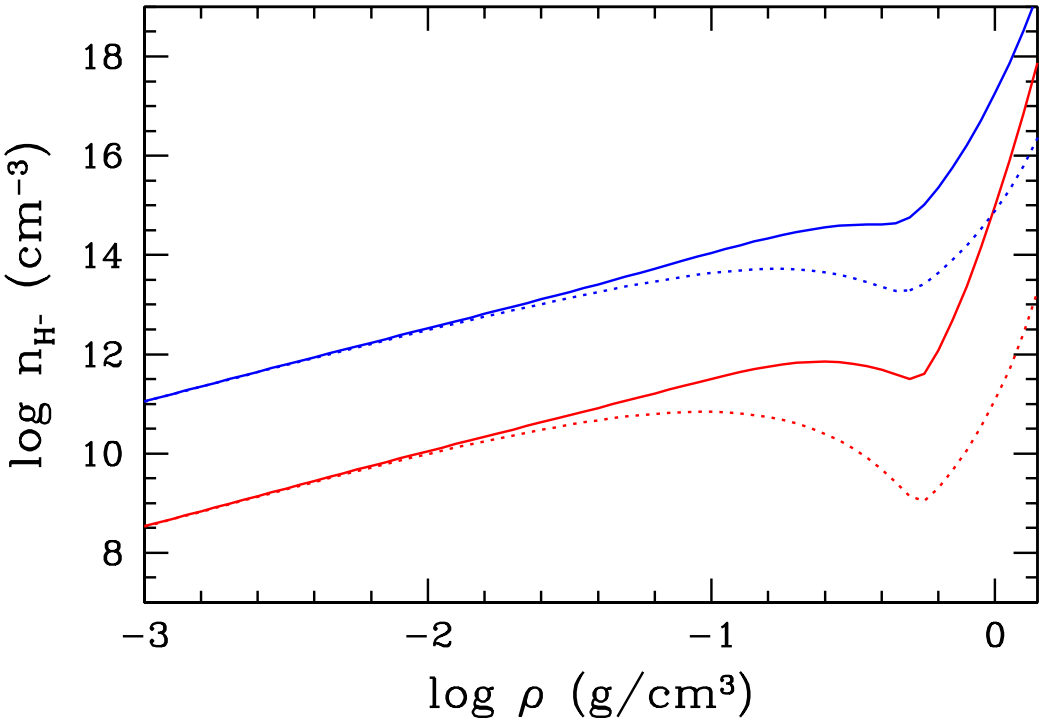

Figure 40: Abundance of H^- in a helium-rich fluid (He/H = 100) for $T = 4000\,K$ (red) and $T = 6000\,K$ (blue). The lines represent the abundances of H^- calculated with (solid) and without (dotted) the non ideal ionization equilibrium of H^-.

and charge conservation. The drop in n_{H^-} with increased density is an effect of non ideal dissociation equilibrium of H_2 that results in a decrease in n_H (Chapter V). The increase at higher densities is caused by the increase in n_e, due to the onset of pressure ionization in helium (Chapter VI).

Bergeron et al. (1997) argued that the weak binding energy and greater spatial extent of the H^- wave function (compared to that of the H atom) should result in the pressure ionization of H^- at relatively low density. The fact that the non ideal effects on H^- are greater than those on H is borne out by our calculation ($\mu^{nid}_{H^-} > \mu^{nid}_H$, Fig. 39). In dense He, the second electron tends to stay bound in H^- because a free electron possesses a large, positive energy that equals μ_e (Fig. 32, see also §6.3.2). This increased stability of H^- in fluid helium is rather counter-intuitive. To verify this result, we have modeled H^- in dense helium with DFT calculations (§3.5), using the ABINIT code

(Gonze et al., 2002, 2005) with the PBE functional, by solving for electronic density in systems of 31 helium nuclei, 1 proton, and 64 electrons. A charge analysis around the proton was conducted using the method of Hirshfeld (1977) as implemented in the ABINIT code. For densities up to $4\,\mathrm{g/cm^3}$ and $T = 5800\,\mathrm{K}$ the two electrons are always localized at the proton. This result confirms that $\mathrm{H^-}$ is stable in dense helium, even at high densities.

7.2 The Bound-free Absorption Cross Section of $\mathrm{H^-}$

The dense fluid environment affects not only the chemistry, but also the photo-ionization barrier of $\mathrm{H^-}$. The photo-ionization energy, $I_{\mathrm{H^-}}$ is given by

$$I_{\mathrm{H^-}} = I^0_{\mathrm{H^-}} - E_{\mathrm{H^-}} + E_{\mathrm{H}} + E_e, \tag{174}$$

where $E_{\mathrm{H^-}}$, E_{H}, and E_e are the excess internal energies of species that arise from the interactions in fluids. These energies for $\mathrm{H^-}$ and H are represented by the second term in Eq. (98) and E_e is the energy of a free electron in fluid helium (§6.3.2). $\mathrm{H^-}$ bf dominates at optical wavelengths even in mixed composition atmospheres up to $\mathrm{He/H} \sim 100$, where $\mathrm{He^-}$ ff becomes dominant. For this composition, the photospheric density is $\lesssim 0.3\,\mathrm{g/cm^3}$ (Fig. 18) and $\Delta I_{\mathrm{H^-}} = I_{\mathrm{H^-}} - I^0_{\mathrm{H^-}} \lesssim 2.1\,\mathrm{eV}$ or $\lesssim 15\%$ of $E^0_{\mathrm{H^-}}$ (Fig. 39). For the less extreme cases, this correction quickly drops below a few percent. Under such conditions, the bound state of $\mathrm{H^-}$ can be described by perturbation theory, where the change in the state energy is of first order and the change in the wave function of second order in the perturbation (Davydov, 1965). We therefore neglect changes in the wave functions. The $\mathrm{H^-}$ bound-free cross section is proportional to the frequency of the absorbed radiation ν, the momentum of the ejected electron $\hbar k$ and the transition dipole moment (Chandrasekhar, 1945)

$$\sigma(\nu) \propto \nu\hbar k |\langle \Psi_{\mathrm{H^-}}(\vec{r}_1,\vec{r}_2)|\vec{d}|\Psi_{\mathrm{f}}(\vec{r}_1,\vec{r}_2,k)\rangle| \propto \nu\sqrt{h\nu - I_{\mathrm{H^-}}}\,|\langle \Psi_{\mathrm{H^-}}(\vec{r}_1,\vec{r}_2)|\vec{d}|\Psi_{\mathrm{f}}(\vec{r}_1,\vec{r}_2,k)\rangle|, \tag{175}$$

where $\Psi_{\mathrm{H^-}}$ is the wave functions of $\mathrm{H^-}$, Ψ_{f} is the wave function of the hydrogen atom and the ejected electron, and $\vec{r}_1$ and $\vec{r}_2$ are the positions vectors of the electrons. Accounting for the change

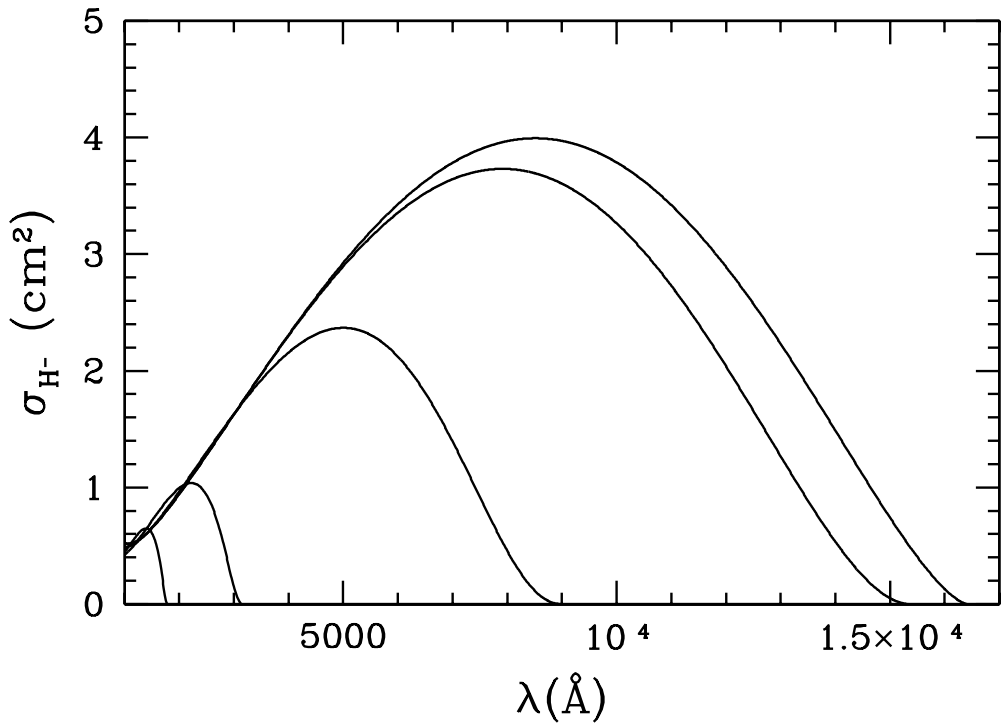

Figure 41: The photo-ionization (bf) cross section of H^- in dense helium for $T = 5000\,\mathrm{K}$ and $\rho_{\mathrm{He}} =$ 0, 0.01, 0.1, 0.5 and 1 g/cm^3 from right to left.

in the ionization energy, the new bf cross-section reads

$$\sigma_{\mathrm{bf}}(\nu) = \sqrt{\frac{h\nu - I_{\mathrm{H}^-}}{h\nu - I^0_{\mathrm{H}^-}}}\,\sigma^0_{\mathrm{bf}}(\nu_0) \quad \text{for} \quad h\nu > I_{\mathrm{H}^-}, \tag{176}$$

where σ^0_{bf} is the bf absorption cross-section of an isolated H^- ion (John, 1988) and

$$\nu_0 = \frac{h\nu - I_{\mathrm{H}^-} + I^0_{\mathrm{H}^-}}{h}. \tag{177}$$

The resulting bf cross-section for selected densities is shown in Fig. 41. The bound-free edge moves from 16436 Å for an isolated H^- ion, to shorter wavelengths and its value decreases with increasing density.

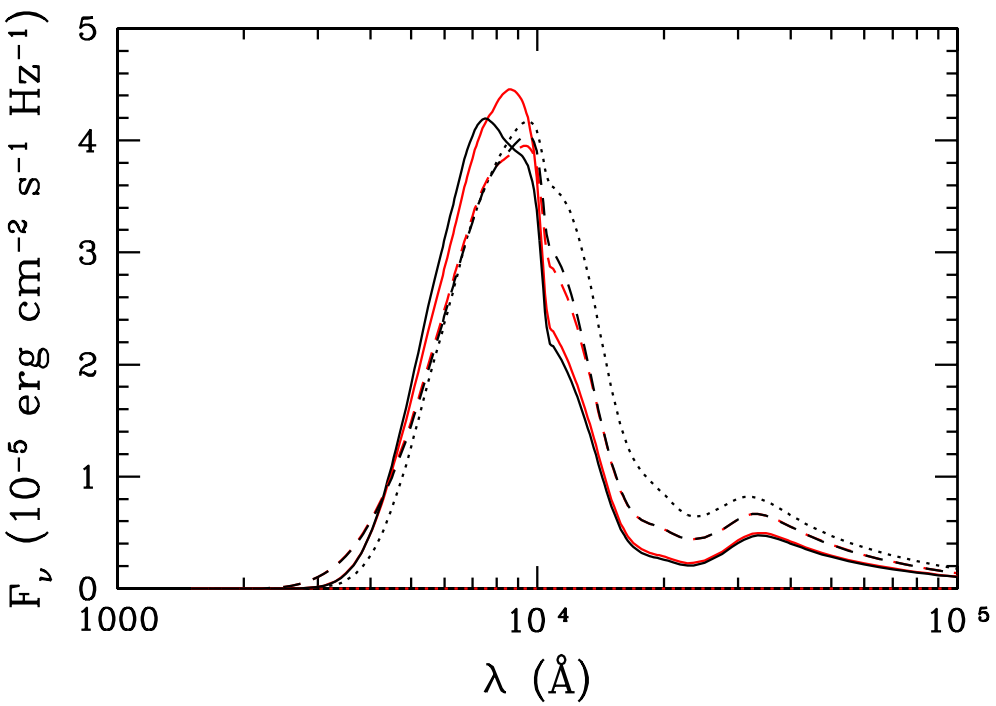

Figure 42: Model spectra for $T_{\rm eff} = 4000\,{\rm K}$, $\log g = 8$ and He/H compositions of 1 (dotted) 10 (solid) and 10^4 (dashed), with (red) and without (black) non ideal ionization equilibrium of H^-.

7.3 Importance in Atmosphere Models

The H^- bf absorption is a dominant source of opacity in white dwarfs atmospheres with He/H $\lesssim$ 100. At higher abundances of helium, He^- ff dominates. The effect of the non ideal chemistry on the H^- abundance and of the change in the bf cross-section, on model spectra is shown in Fig. 42. There is no effect on spectra of model with He/H = 1, as the density at the photosphere is low ($\rho \sim 0.025\,{\rm g/cm^3}$, Fig. 18). The increase in $n_{\rm H^-}$ and the change in the bf cross section results in a redistribution of flux around $1\,\mu$m in the spectra of model with He/H = 10. For higher helium abundances, He^- dominates and the effect becomes negligible. As the density at the photosphere in the atmosphere model of He/H = 10, the most extreme case, is still not so high ($\rho \sim 0.1\,{\rm g/cm^3}$, Fig.

18), the non ideal ionization equilibrium of H^- has a moderate effect on the spectrum. The overall effect is not as significant as that of the non ideal chemistry of molecular hydrogen (chapter IV).

7.4 Computation of the Chemical Equilibrium in the Models

This completes our study of non ideal effects in He/H mixtures. In calculating the chemistry and thermodynamics for the atmosphere models, we consider the following species: H, H_2, H^-, H^+, H_2^+, H_3^+, He, He^+, He_2^+, HeH^+, and e. Non ideal effects are introduced for the most abundant and the most spectroscopically important species: H, H^-, H_2, He, e, He^+, and He_2^+ all interacting with the He only (Chapters V, VI and VIII). We do not consider Coulomb interactions between charged species or electron degeneracy, both being negligible if the ionization fraction remains low ($\lesssim 0.1\%$). We consider the following reactions

$$H \leftrightarrow H^+ + e \tag{178}$$

$$H^- \leftrightarrow H + e \tag{179}$$

$$H_2 \leftrightarrow 2H \tag{180}$$

$$H_2^+ \leftrightarrow H + H^+ \tag{181}$$

$$H_3^+ \leftrightarrow 2H + H^+ \tag{182}$$

$$He \leftrightarrow He^+ + e \tag{183}$$

$$He_2^+ \leftrightarrow He + He^+ \tag{184}$$

$$HeH^+ \leftrightarrow H^+ + He \tag{185}$$

and the chemical equilibrium (Eq. 112) for each of them. When complemented with the conditions of charge conservation

$$n_{H^+} + n_{H_2^+} + n_{H_3^+} + n_{He^+} + n_{He_2^+} + n_{HeH^+} = n_{H^-} + n_e \tag{186}$$

and mass conservation

$$m_{\rm H} n_{\rm H} + m_{\rm H^-} n_{\rm H^-} + m_{\rm H_2} n_{\rm H_2} + m_{\rm H^+} n_{\rm H^+} + m_{\rm H_2^+} n_{\rm H_2^+} + m_{\rm H_3^+} n_{\rm H_3^+} + 0.2 m_{\rm HeH^+} n_{\rm HeH^+} = \frac{1}{1+y}\rho \quad (187)$$

$$m_{\rm He} n_{\rm He} + m_{\rm He^+} n_{\rm He^+} + m_{\rm He_2^+} n_{\rm He_2^+} + 0.8 m_{\rm HeH^+} n_{\rm HeH^+} = \frac{y}{1+y}\rho, \quad (188)$$

where $y = {\rm He/H}$, the set of equation (178)–(188) is solved self-consistently at a given T and P, using the linearization method of Mihalas (1978).

CHAPTER VIII

THE PSEUDO-CONTINUUM BOUND-FREE OPACITY OF HYDROGEN

About a decade ago, the analysis of a large sample of cool white dwarfs with what were then state-of-the-art atmosphere models revealed a systematic blue flux excess in cool H-rich models (Bergeron et al., 1997). This disagreement, which has not been resolved, has been attributed to an extension of the bound-free (bf) opacity of H in its ground state beyond the Lyman edge– the so-called pseudo-continuum bf opacity (Bergeron et al., 1997, 2001; Bergeron, 2001) – or to the red wing of the Ly α line (Wolff et al., 2002). Both effects arise from the perturbations of H atoms due to interactions with other particles. We have developed new, physically realistic models for both absorption processes and applied them to cool white dwarf atmospheres. Notably, these two models have no free parameters. In this chapter we model the pseudo-continuum bf opacity of hydrogen (Kowalski, 2006b). Pressure broadening of the Ly α line is the subject of chapter IX.

8.1 Origin of the Problem

An important advance in modeling the equation of state and opacities of stellar atmosphere and envelopes was a formal implementation of the occupation probability formalism (Hummer & Mihalas, 1988; Seaton et al., 1994). An extension of this EOS model by Däppen et al. (1987) (hereafter DAM) allows the calculation of the pseudo-continuum opacity, i.e., the pressure-broadening of the Lyman bf edge. However, when the DAM model is used to calculate this source of opacity with the occupation probabilities of Hummer & Mihalas (1988, hereafter HM) it dominates all other absorption processes at optical wavelengths for white dwarfs with $T_{\rm eff} < 17000\,{\rm K}$. Such a strong absorption is completely unrealistic and is not observed (Bergeron, 2001; Bergeron et al., 1997). Nonetheless, this process may still be significant in white dwarf atmospheres. Exploring this idea further, Bergeron (2001) introduced an arbitrary damping function to the DAM pseudo-continuum opacity to obtain good fits of the photometry of a few stars. However, the damping function must be adjusted for each

star, indicating how unsuitable the DAM model is. As a result, the pseudo-continuum bound-free opacity of hydrogen atoms is ignored in the modeling of cool white dwarf atmospheres.

The pseudo-continuum bound-free opacity results from the perturbation of hydrogen atoms in their ground state by their interaction with other particles in a dense medium (Däppen et al., 1987). Such perturbations result in a lowering of the ionization barrier of some of the hydrogen atoms, and the possibility of a bound-free transition caused by photons with energies that are smaller than the ionization potential of the isolated hydrogen atom. This effect is loosely called "lowering of the continuum." DAM considered this process in the framework of the occupation probability formalism proposed by HM and constructed a simple model for the optical properties of an interacting, partially ionized hydrogen fluid. HM assumed that in a non ideal fluid, the excited states of atoms are most strongly affected by interactions with their neighbors because of their weaker binding energies and greater extent of their wave functions (greater sizes). They directly related the strength of such interactions with the sizes of atoms (excluded volume interaction model). The DAM and HM models are not very precise, as they treat the inter-particle interactions and the associated lowering of the ionization potential only in terms of the average sizes of the particles. We will show that a quantum mechanical description of the interactions between hydrogen atoms and perturbers, absent in the simple DAM model, is necessary to obtain a physically realistic value of the pseudo-continuum opacity of hydrogen atoms in the atmospheres of white dwarf stars.

8.2 The Pseudo-continuum Opacity Model of Däppen-Anderson-Mihalas

The DAM model is based on the occupation probability formalism introduced by HM for calculating thermodynamical properties of a non ideal gas. HM treat the non ideal effects on the equation of state by introducing a state occupation probability in the internal partition functions of bound species. The modified partition function of the hydrogen atom is given by

$$Z_{\rm int} = \sum_i g_i \omega_i e^{-\epsilon_i / k_B T} = \sum_i \omega_i \gamma_i, \tag{189}$$

where i indicates the atomic level, g_i is the statistical weight, ϵ_i is the energy state i with respect to the ground state level ($i = 0$), and ω_i is the occupation probability. In the HM model, $0 \leq \omega_i \leq 1$ is

the probability that level i is occupied, given that the interactions eventually destroy the bound level. The HM formalism provides a self-consistent way to compute ω_i for a given interaction model. In a non interacting gas, all $\omega_i = 1$, which leads to the usual divergence of the internal partition function $Z_{\rm int}$ (Eq. 189). In an interacting gas, the upper levels are generally more strongly affected by the interactions and ω_i decreases monotonically, providing a finite $Z_{\rm int}$. For the physical conditions found inside weakly ionized cool white dwarf atmospheres interactions are primarily with neutral particles (Bergeron et al., 1991) and are repulsive at short range. In the HM model, this is described with a simple excluded volume interactions model and ω_i decreases rapidly for higher principal quantum number (HM, Equation 3.4). The number of hydrogen atoms in state i is expressed as

$$\frac{n_i}{n_{tot}} = \frac{\omega_i \gamma_i}{Z_{\rm H}}, \tag{190}$$

where n_{tot} is the total number density of atomic hydrogen.

DAM extended this model for the calculation of the optical properties of hydrogen atoms in partially ionized plasmas. They interpreted the factor $1 - \omega_i$ as the fraction of hydrogen atoms with atomic level i is being "dissolved," i.e., sufficiently perturbed to describe an unbound electron and ion. They assigned this value to the fraction of free-electrons states available for a bound-free transition to level i. DAM used this interpretation to derive that for the absorption of a photon associated with the transition from level i to level j, the probability that level j is bound (i.e. the transition is bound-bound), is $\omega_j/\omega_i < 1$. Therefore, the probability of having a bound-free transition is

$$P_{bf} = 1 - \frac{\omega_j}{\omega_i}. \tag{191}$$

To describe the pseudo-continuum absorption to the continuum energy levels localized between two discrete but "dissolved" levels of the hydrogen atom, DAM introduced the pseudo-level n^* with occupation probability ω_{n^*}. The latter is calculated by interpolating between the ω_i's. Therefore, the probability that, during the i to n^* transition, the absorbing electron goes into the continuum

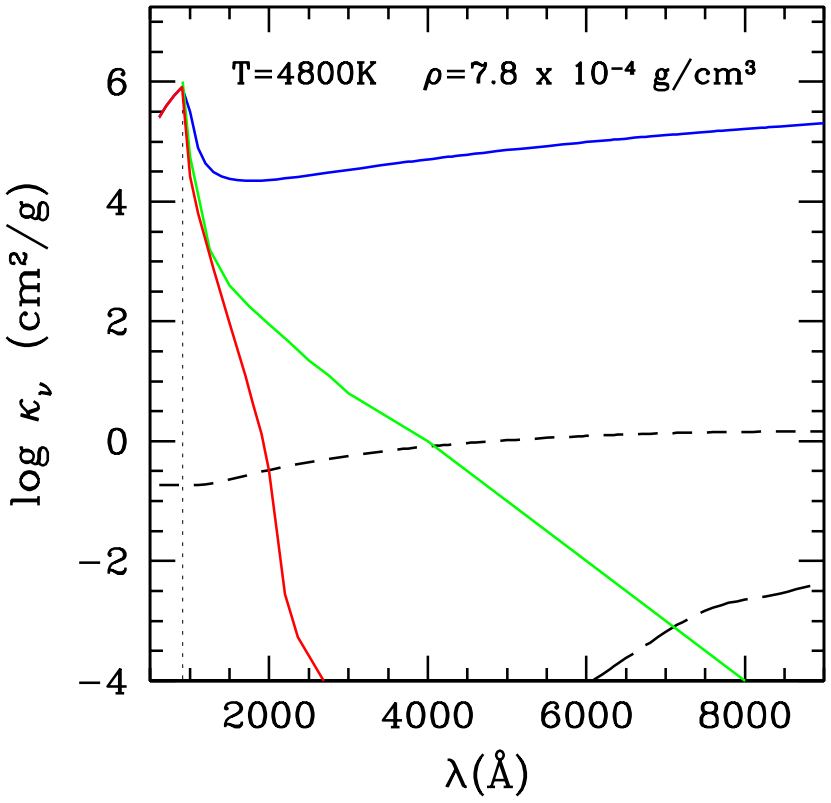

Figure 43: The most important sources of opacity at the photosphere of a pure hydrogen model atmosphere with $T_{\rm eff}$ = 4600K and $\log g$ = 7.75 (cgs) – the atmospheric parameters of the white dwarf star LP 380-5 (WD 1345+238) presented on Fig. 4 of Bergeron (2001). The lines represent our calculation of the pseudo-continuum opacity (red), the pseudo-continuum opacity from the DAM model (blue), the H^- bound-free opacity (dashed), the H_2 CIA opacity (long dashed), and the pseudo-continuum opacity derived by Bergeron (2001) to fit the spectrum of this star (green). The vertical dotted line is the Lyman bf edge for an isolated H atom.

is given by (Eq. 32 of DAM)

$$P_{bf} = 1 - \frac{\omega_{n^*}}{\omega_i}. \tag{192}$$

In Fig. 43 we present the main opacity sources at the photosphere of the white dwarf LP 380-5 which Bergeron (2001) used as an example to study the role of the pseudo-continuum opacity. After a rapid decrease beyond the Lyman bf edge the DAM pseudo-continuum opacity rises again and dominates all other opacity sources (including the Balmer lines) by orders of magnitude in the entire optical spectral range. This result is unrealistic and simply not observed. The DAM model greatly

overestimates the pseudo-continuum bound-free absorption in the atmospheres of cool white dwarf stars. In view of the difficulty with this application of the DAM model of the pseudo-continuum opacity, we developed a more realistic approach to calculate this source of absorption.

8.3 A New Model for the Pseudo-continuum Opacity of H

The bound-free absorption process results in the ionization of a hydrogen atom. The lowering of the hydrogen ionization potential arises from the interaction of the hydrogen atom with neighboring particles (Däppen et al., 1987). However, we are interested in the pseudo-continuum opacity far from the Lyman edge, i.e. $\lambda \gtrsim 1500\,\text{Å}$. A significant lowering of the hydrogen ionization barrier ($\gtrsim 5\,\text{eV}$) is required for bound-free absorption at these wavelengths. Such a situation occurs during rare, close collisions for which the inter-particle collision distances, r_c, are small enough that the probability (P_c) of finding a colliding pair with an inter-particle separation smaller than r_c is much smaller than unity. In this case, multi-particle collisions are insignificant, as the probability of having a close N-particle collision is roughly $\sim P_c^{N-1}$. Therefore, it is sufficient to consider the interaction between a H atom and its closest neighbor only. Allard et al. (2004) used this approximation to successfully explain the complex shape of the Lyman α line wings detected in the spectra of white dwarfs with $T_{\rm eff} \sim 12000\,\text{K}$.

For a given colliding pair, the change in the ionization energy results from the formation of a temporary dimer whose ionization energy differs from that of the isolated hydrogen atom, $I_0 = 13.598\,\text{eV}$. This modified ionization barrier I_p is given by the ionization energy of a dimer calculated at a fixed inter-particle separation r_c

$$I_p(r_c) = \Phi_{\text{H}^+-\text{pert}}(r_c) - \Phi_{\text{H}-\text{pert}}(r_c), \tag{193}$$

where $\Phi_{\text{H}-\text{pert}}(r_c)$ and $\Phi_{\text{H}^+-\text{pert}}(r_c)$ are the energies of the neutral and singly ionized dimers, respectively. This picture is in the spirit of the Franck-Condon principle, which states that as a result of the large difference between the mass of the absorbing electron and the nuclear mass, the nuclei remain fixed during the absorption/emission of a photon (Davydov, 1965). The differential probability of finding such a dimer with an inter-particle separation between r_c and $r_c + dr_c$ is directly

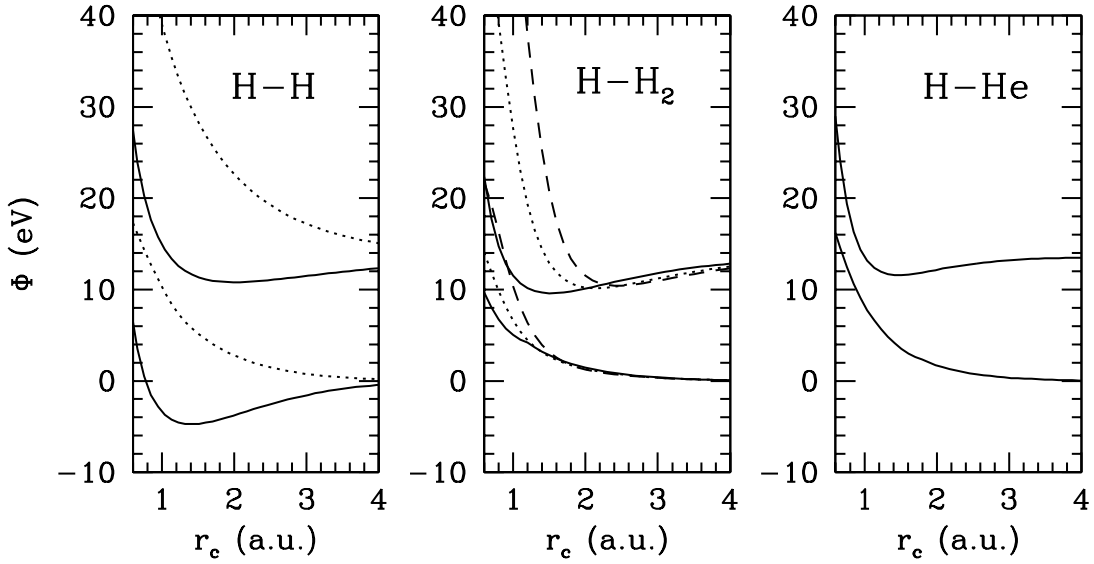

Figure 44: The interaction energy curves as a function of separation for neutral dimers (lower curves) and the corresponding singly-ionized dimers (upper curves). The two sets of curves for the $H-H$ interaction are for the *bound* (solid line) and *anti-bound* (dotted line) interaction potentials for $H-H$ and $H-H^+$. The different energy curves for the $H-H_2$ interaction are for different orientations of the molecule, with the angle defined between the line connecting the perturber to the center of H_2 and the molecular axis. Interactions for the following angles are shown: 90^o (solid), 45^o (dotted), and 0^o (dashed).

related to the two particle distribution function (Eq. 84)

$$dP(r_c) = n_{pert} r_c^2 dr_c \left(\int_{\theta,\phi} g(r_c,\theta,\phi) \sin\theta d\theta d\phi \right), \tag{194}$$

where in a low density medium ($\rho \lesssim 0.1\,\mathrm{g/cm^3}$)

$$g(r_c,\theta,\phi) = \exp(-\Phi_{\mathrm{H-pert}}(r_c,\theta,\phi)/k_BT + \omega(r_c,\theta,\phi)) \sim \exp(-\Phi_{\mathrm{H-pert}}(r_c,\theta,\phi)/k_BT) \tag{195}$$

In Eqs (194)–(195), n_{pert} is a number density of perturbers, $\Phi_{\mathrm{H-pert}}$ is the interaction energy between a hydrogen atom and the perturber localized at the position (r_c,θ,ϕ) in relation to the hydrogen atom, which is assumed to be at the origin of the coordinate system. Here, we have retained the angular dependence of the potential Φ, which can be anisotropic (e.g., $H-H_2$ dimer).

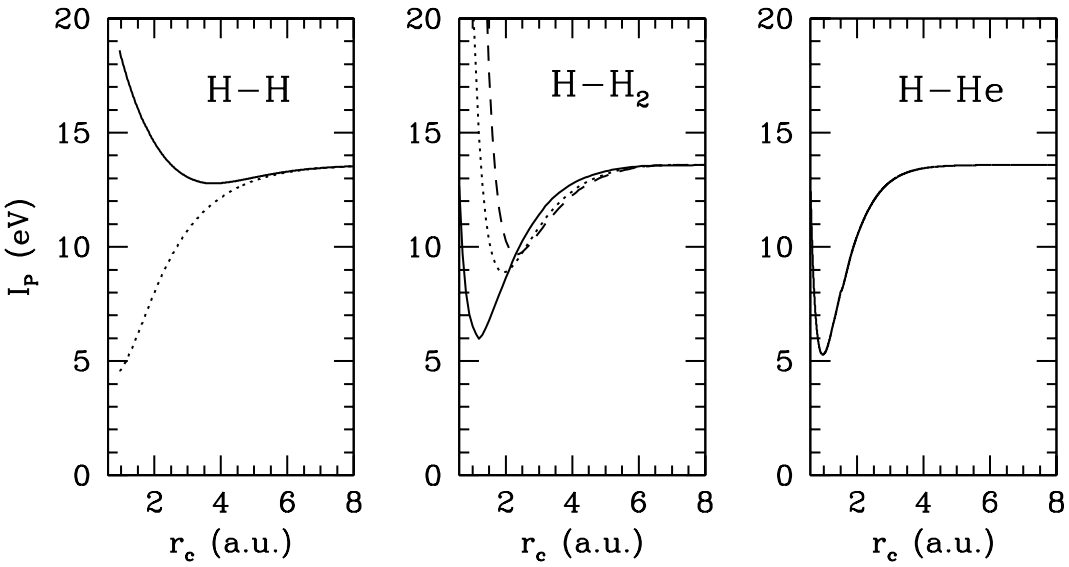

Figure 45: The ionization energy of dimers as a function of the inter-particle distance. See Fig. 44 for legend.

The main perturbers in the atmospheres of cool white dwarfs are the most abundant species H, H_2, and He. The sources for the interaction potentials are: $H - H$ [Kolos & Wolniewicz (1965)], $H - H_2$ [Broothroyd et al. (1991)], and $H - He$ [Shalabi et al. (1998)]. The corresponding potential curves for the singly ionized dimers are: H_2^+ [Bates & Reid (1968)], H_3^+ [Prosmiti et al. (1997)], and HeH^+ [Green et al. (1974)]. These potentials are plotted on Fig. 44. As a result of the *gerade/ungerade* symmetry in the $H - H$ interaction, we have to consider both the *bound* and the *anti-bound* $H - H$ potential energy curves. For the singly ionized dimers we chose the ground state potential energy curves because the upper energy curves (like the *anti-bound* state of H_2^+, Fig. 44.) would result in a much smaller decrease in the ionization energy for a given r_c. Because $dP_c \sim \exp(-\Phi(r_c)/k_B T)$, this decrease occurs with a much smaller probability than the same change in the ionization potential that results from the ionic ground states at a much larger r_c, and therefore can be neglected. The resulting ionization energy $I_p(r_c)$ for a given dimer as a function of the collision distance are plotted on Fig. 45. The ionization energy can decrease to $\sim 5\,\mathrm{eV}$, which occurs for very small r_c. Due to the strong repulsion in the neutral dimer at short separation (Fig. 44), such a large lowering

of the ionization energy occurs with very small probability, as for small r_c the Boltzmann factor $\exp(-\Phi_{\mathrm{H-pert}}/k_BT) << 1$ in Eq. (194). Moreover, in the case of the H − H interaction, only the *anti-bound* potential leads to a significant decrease of the ionization barrier (Fig. 44).

The probability of a hydrogen atom having an ionization energy I_p sufficiently small for photo-ionization to be caused by a photon of frequency ν is

$$P(\nu) = \sum_{\mathrm{k}} \int_{I_p(r_c)<h\nu} dP(r_c), \tag{196}$$

where sum is over the perturber species (H, H_2 and He) and the integration is performed over the range of separations r_c such that $I_p(r_c) < h\nu$. The resulting probabilities, as a function of wavelength of having a bound-free transition for H for two temperatures and three different compositions are shown in Fig. 46. The corresponding probabilities from the DAM model are several orders of magnitude larger. We find that for a given density, collisions with H_2 are most effective at lowering the ionization energy of H. This result is because, for a given value of $I_p(r_c)$, the interaction potential $\Phi_{\mathrm{H-H_2}}(r_c)$ computed for the orientation angle ~ 90 (see caption of Fig 44. for definition) is much less repulsive than $\Phi_{\mathrm{H-H}}(r_c)$ and $\Phi_{\mathrm{H-He}}(r_c)$. The pseudo-continuum bf opacity extends to larger wavelengths at higher T because close-range collisions are more frequent at higher kinetic energies ($dP \sim \exp -\Phi(r_c)/k_BT$).

The pseudo-continuum opacity is then obtained with

$$\kappa_{\mathrm{bf}}(\nu) = \frac{n_H}{\rho} P(\nu) \sigma^0_{bf}(\nu) \quad (h\nu < 13.598\,\mathrm{eV}), \tag{197}$$

where

$$\sigma^0_{\mathrm{bf}}(\nu) = \frac{2.815 \times 10^{29}}{\nu} \left[0.9916 + \left(2.719 \times 10^{13} - \frac{2.268 \times 10^{30}}{\nu} \right) \frac{1}{\nu} \right] \tag{198}$$

is the bound-free cross section of the isolated hydrogen atom (Karsas & Lather, 1961; Kurucz, 1970) extrapolated beyond the Lyman edge (DAM). A proper calculation would consider the bound-free cross section of the dimer as a function of inter-particle separation. To our knowledge this information is not available. However, as the photo-ionization cross sections for H (Palenius et al.,

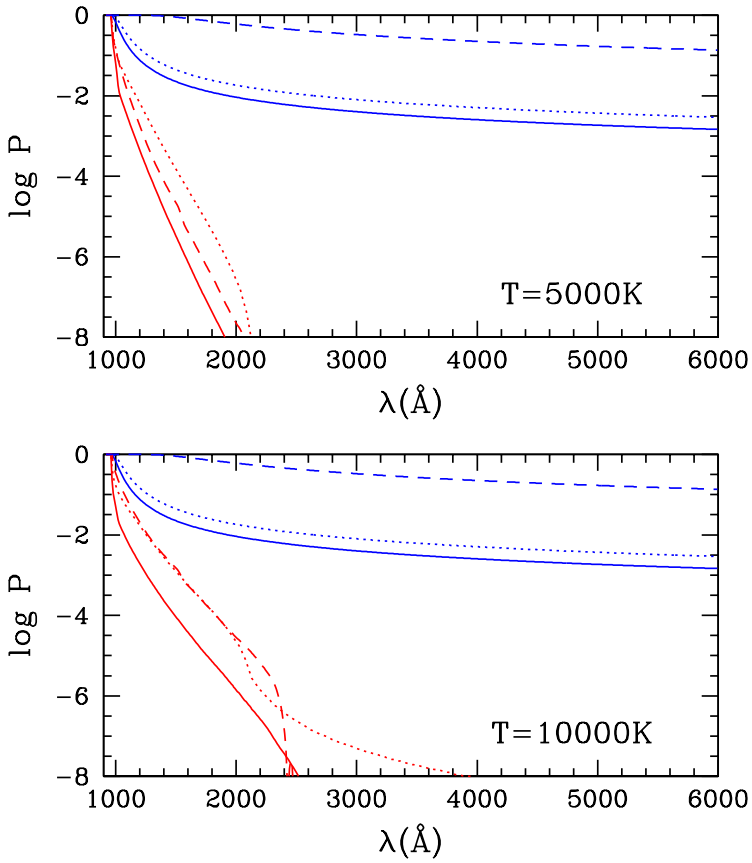

Figure 46: The probability of lowering the bound-free continuum from our model (red lines), and the DAM model (blue lines), as a function of wavelength for selected temperatures. Calculations for the following compositions are shown: (1) $n_{\rm H} = 10^{21}$ cm^{-3} (solid line), (2) $n_{\rm H} = n_{\rm H_2} = 10^{21}$ cm^{-3} (dotted line), and (3) $n_{\rm He} = 10^{23}$ cm^{-3} (dashed line).

1975) and H_2 (Ford et al., 1974) differ by less than a factor of 3, we estimate that the extrapolation of the bound-free cross-section of the isolated hydrogen atom beyond Lyman edge introduces an uncertainty no larger than an order of magnitude on $\kappa_{bf}(\nu)$ calculated by Eq. (197). In view of the very rapid decrease of $P(\lambda)$ as λ increases, the extrapolation of σ^0_{bf} far beyond the Lyman edge is of little consequence. In helium-rich atmospheres, where the density can be as high as $2-3\,{\rm g/cm^3}$, the full two particle distribution function should be used in Eq. (194), i.e., we cannot neglect the partial thermal potentials, $\omega_{\rm H-pert}$. Solving the Ornstein-Zernike equation in the Percus-Yevick approximation (§2.2) for fluid He, we have verified that in the helium-rich atmospheres of cool white

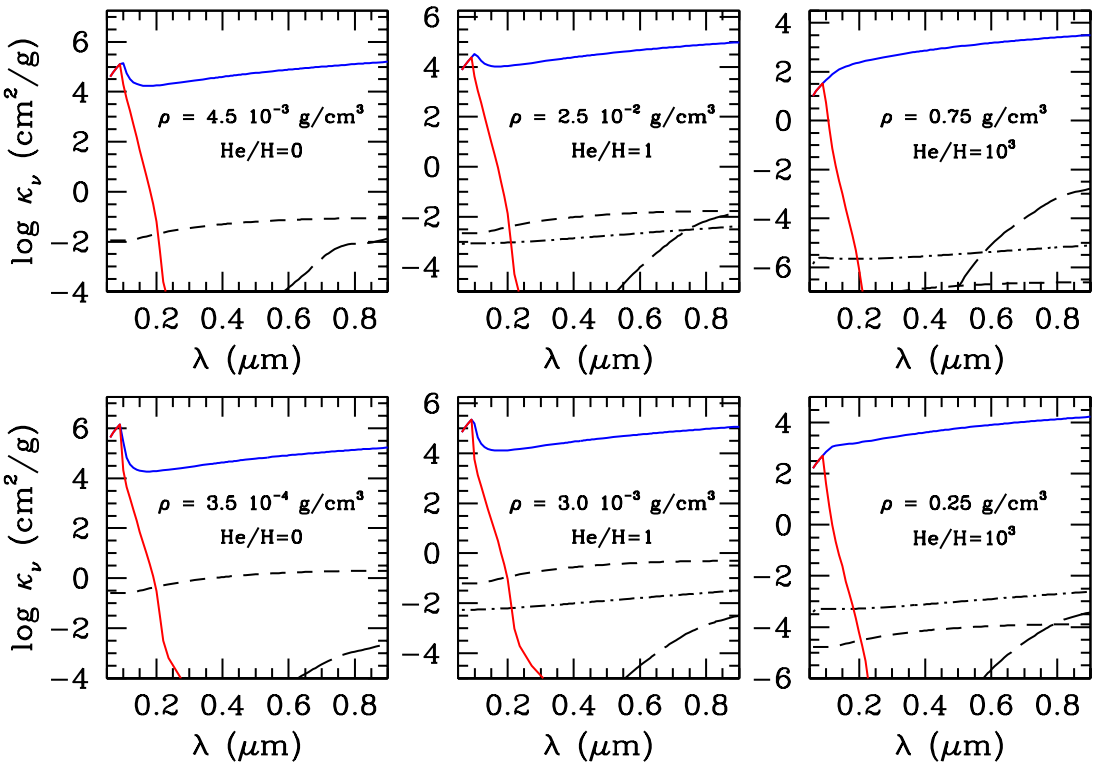

Figure 47: The most relevant sources of opacity for representative physical conditions at the photosphere of cool white dwarf stars. Upper panels: $T = 4000\,\mathrm{K}$, lower panels: $T = 5000\,\mathrm{K}$. The lines represent the pseudo-continuum opacity calculated here (red solid), the pseudo-continuum opacity of DAM (blue solid), the H^- bound-free opacity (dashed), the H_2 CIA opacity (long dashed), and the He^- free-free opacity (dash-dotted).

dwarfs, $\exp(\omega_{\mathrm{H-pert}}(r_c, \theta, \phi)) < 100$. Therefore, in the most extreme case, ignoring the correlations in Eq. (197) leads to an underestimate of κ_{bf} of no more than two orders of magnitude. We will see below that this does not affect our conclusions.

8.4 Importance of the Pseudo-continuum Opacity in Cool White Dwarf Atmospheres

Our goal is to determine whether the pseudo-continuum bound-free absorption by atomic hydrogen beyond the Lyman edge may be the missing source of opacity in the atmosphere models of cool white dwarfs ($T_{\mathrm{eff}} \lesssim 6000\,\mathrm{K}$). For this purpose, we have computed opacities for temperatures, densities, and He/H composition that are representative of the photospheres of these stars.

The pseudo-continuum opacity calculated with our model dominates all other sources of opacity at wavelengths shorter than $\sim$ 2000 Å (Fig. 47). For these cool stars the flux at these wavelengths is extremely small and completely negligible (see Fig. 47 of Bergeron (2001)). We also note that the uncertainty in the photo-ionization cross section and our neglect of the correlations in dense helium-rich atmospheres do not alter the pseudo-continuum opacity enough to make it important at $\lambda > 2000$ Å.

Finally, we compare our pseudo-continuum opacity with that derived by Bergeron (2001) to fit the blue spectrum of white dwarf LP 380-5 in Fig. 43. Our new models show that it is completely insignificant at $\lambda > 2000$ Å and is far too small to explain the model flux excess in the blue. Therefore, the pseudo-continuum opacity is not the missing source of absorption in model spectra of cool white dwarfs and we ignore it in our models.

CHAPTER IX

PRESSURE-BROADENING OF THE LYMAN α LINE OF HYDROGEN

In Chapter VIII, we showed that the pseudo-continuum bf opacity of hydrogen can not reduce the flux excess seen at blue wavelengths in cool, hydrogen-rich models. In this chapter we consider the possibility that the missing opacity is the red wing of the pressure-broadened Lyman α line of hydrogen. This absorption mechanism results from the perturbations of hydrogen atoms by their interaction with other particles, primarily H and H_2. Such perturbations result in the lowering of the Ly α transition energy and the possibility of a bound-bound transition for photon energies that are smaller than that of an isolated hydrogen atom. We present a new, semi-classical calculation of this process that is similar to the one we developed for the pseudo-continuum bf absorption in Chapter VIII. The model has no free parameters and relies on accurate quantum mechanical calculations (Kowalski & Saumon, 2006).

9.1 Theoretical Approach

We are interested in the Ly α opacity far from the line center, at wavelengths $\lambda \gtrsim 2500\,\text{Å}$. A lowering of the Ly α transition energy by more than $\sim 5\,\text{eV}$ is required for a bound-bound absorption from the ground state of hydrogen atom at these wavelengths. Following the same arguments we used for constructing the model for the pseudo-continuum opacity (§8.3), we consider the interaction between a H atom and its closest neighbor only. This approach was used to explain successfully the complex shape of the Lyman α line wings detected in the spectra of white dwarfs with $T_{\rm eff} \sim 12000\,\text{K}$ (Allard et al., 2004), the UV flux deficiency observed in the white dwarf star L745 – 46A (Koester & Wolff, 2000), and to model resonance broadening of the Ly α line in the solar spectrum (Sando et al., 1969).

For a given colliding pair, the change in the Ly α transition energy results from the formation of a temporary dimer, whose first transition energy E_{12} differs from that of an isolated hydrogen atom, $E_{12}^0 = 10.2\,\text{eV} \equiv 1216\,\text{Å}$. E_{12} is given by the differences in the energies of the ground state and

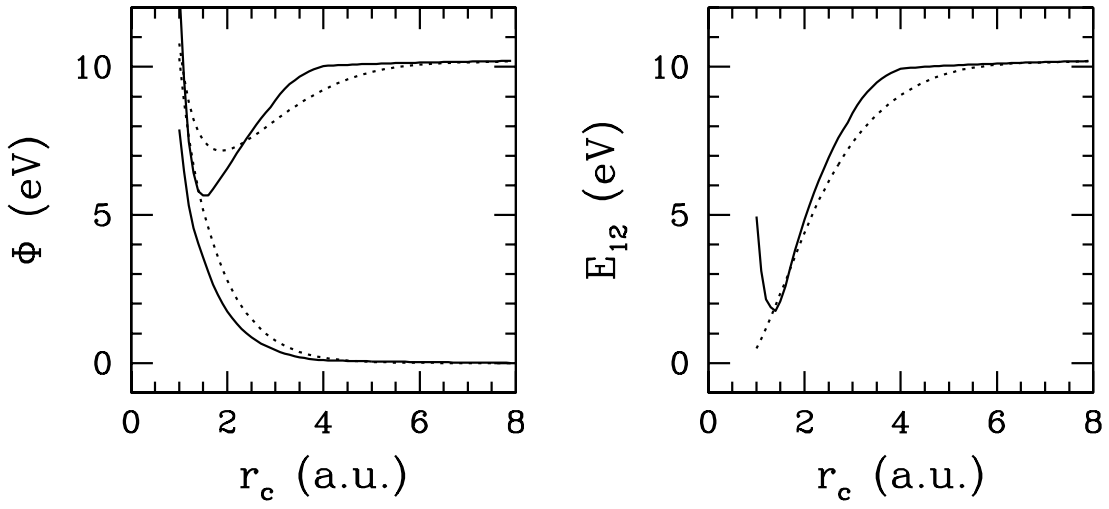

Figure 48: The interaction energy curves for the ground state (lower curves) and the first excited Rydberg state (upper curves)(left panel) and the first transition energy E_{12} (right panel) as a function of the inter-particle collision distance of $H - H_2$ (solid) and $H - H$ (dotted) dimers. For $H - H_2$ the energy curves shown are for a collision angle of 90^o, where the collision angle is defined between the line connecting the H atom to the center of H_2 and the molecular axis.

first excited Rydberg state of a H-perturber dimer calculated at a fixed inter-particle separation r_c: $E_{12}(r_c) = E_2(r_c) - E_1(r_c) = h\nu_{12}$, where ν_{12} is the frequency of the absorbed photon (Fig. 48). For large separation ($r_c \gtrsim 5\, a.u.$), $E_{12}(r_2) \rightarrow E^0_{12}$, the isolated atom value (Fig. 48). The differential probability of finding such a dimer with an inter-particle separation between r_c and $r_c + dr_c$ is given by Eq. (194). The potential for the interaction of a hydrogen atom with H ($H - H$ dimer) is from Kolos & Wolniewicz (1965) and that for perturbations by H_2 ($H - H_2$ dimer) is from Broothroyd et al. (1996, 1991) (Fig. 48). For the $H - H$ dimer, the allowed bound-bound transition from the ground state with the smallest transition energy (i.e., greatest broadening) at all values of r_c is from the molecular state $b\,^3\Sigma_u^+\, 2p\sigma$ to the $a\,^3\Sigma_g^+\, 2s\sigma$ state. Satellite features (Allard et al., 1994) do not appear for this transition because the difference between the two energy curves has no extrema (dotted line on Fig. 48). Contributions from transitions to other (higher) excited levels of the $H - H$ dimer (such as $h\,^3\Sigma_g^+\, 3s\sigma$ and $i\,^3\Pi_g\, 3d\pi$) are negligible in the far red wing ($\lambda \gtrsim 2000\,$Å) because they always lie above the $a\,^3\Sigma_g^+$ state by at least 2.5 eV in the relevant range of r_c and hence only

provide absorption for photons with higher energies than the $a\,^3\Sigma_g^+$ state. For the same reason, transitions from the binding H − H ground state ($X\,^1\Sigma_g^+(1s\sigma)^2$) are also negligible in the far red wing. We use the $a\,^3\Sigma_g^+$ $2s\sigma$ energy curve from Staszewska & Wolniewicz (1999). For the energy of the first excited Rydberg state of the $H - H_2$ system, we used the H_3 calculations of Broothroyd et al. (1996). To obtain the H – H_2 potential from the H_3 potential surface, we assumed a fixed internuclear separation for H_2 of 1.4 a.u. This approach is justified by the fact that the atoms in H_2 vibrating in the ground state spend most of the time at the equilibrium internuclear separation. At the temperatures of interest ($T \lesssim 6000\,K$), the vibrational excitation is small, and so is the amplitude of vibration ($\lesssim 0.4$ a.u.). We have verified that such a small change in the intermolecular separation does not affect our results significantly.

The line profile is calculated in the quasi-static approximation, which is suitable for a calculation of the far line wings perturbed by classical particles (Allard & Kielkopf, 1982). The profile of the line $\alpha(\nu)$ is given by (Allard & Kielkopf (1982), Eqs. 13 & 61)

$$\alpha_\nu d\nu \sim \sum_k dP_c(r_c(\nu)) \frac{|\langle 2|\vec{d}|1\rangle|^2}{|\vec{d}^0_{12,\mathrm{H}}|^2}, \tag{199}$$

where sum is over the perturber species (H, H_2), $\langle 2|\vec{d}|1\rangle$ is the transition dipole moment between the ground state and the first excited Rydberg state of the colliding pair, and $|\vec{d}^0_{12,\mathrm{H}}|$ is the transition dipole moment of the isolated hydrogen atom. The dipole transition moments, which vary with separation r_c, are from Staszewska & Wolniewicz (1999) for H − H and Peng et al. (1995) for $H - H_2$. Equation (199) guarantees that the line profile is normalized as in the core of the line $\alpha_\nu d\nu \sim \sum_k dP_c$ and the differential probability $\sum_k dP_c$ integrates to 1 in frequency. The absorption cross section is $\sigma_\nu(\mathrm{cm}^2) = \pi \mathrm{e}^2 \mathrm{f}_{12} \alpha_\nu / \mathrm{mc}$, where f_{12} is the oscillator strength for the Ly α transition, and is a linear function of density of perturbers (as $dP_c \propto n_{\mathrm{pert}}$). In Fig. 49 we present the absorption cross sections for the red wing of Ly α broadened by collisions with H and H_2. For a given Ly α transition energy, the $H - H_2$ ground state interaction is much less repulsive than the H − H ground state interaction (Fig. 48), and the probability of a close $H - H_2$ interaction is larger than that of a close H − H interaction ($dP_c(H - H_2) >> dP_c(H - H)$). Hence, the $H - H_2$ collisions are the dominant

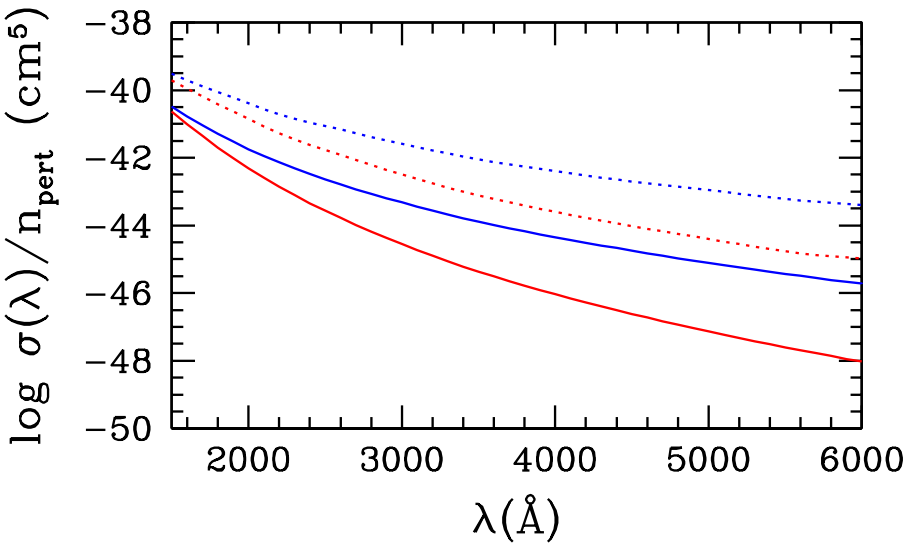

Figure 49: The absorption cross-section of the Ly α line pressure broadened by collisions with H (solid lines) and H_2 (dotted lines) for T equal 6000 K (blue) and 4000 K (red).

contributors to the Ly α line red wing opacity in the atmospheres of cool H-rich white dwarfs with a significant abundance of H_2 ($T_{\rm eff} < 6000$ K).

9.2 Applications to Pure Hydrogen Atmospheres

9.2.1 The Spectral Energy Distribution of Cool DAs

BPM 4729 (WD 0752−676) is the only cool DA white dwarf observed in the near UV (Wolff et al., 2002). When complemented with the $BVRIJHK$ photometry of Bergeron et al. (2001) and the U magnitude (McCook & Sion, 1999), the complete spectral energy distribution (SED) of this cool white dwarf is obtained. The UV spectrum extends well into the wing of the Ly α line and thus provides an excellent measure of the strength and profile of the line. Our fit of a pure H model ($T_{\rm eff} = 5820$ K, $\log g = 8.30$) to the entire SED of BPM 4729 is excellent (Fig. 50). These values of $T_{\rm eff}$ and g agree with the values of Bergeron et al. (2001) for this star at the 1σ level. The high quality of the fit of the UV spectrum demonstrates the validity of our model for the far red wing of the Ly α line under the conditions encountered in BPM 4729. At the photosphere, the composition is

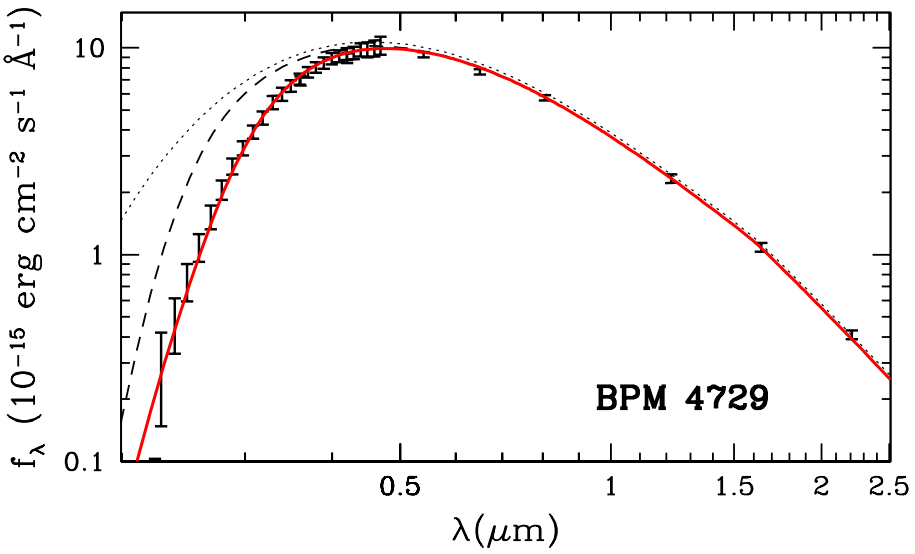

Figure 50: The spectral energy distribution of the DA white dwarf BPM 4729 (WD 0752−676). The UV spectrum of Wolff et al. (2002) extends up to 4500 Å. Additional measurements are broadband fluxes from U (McCook & Sion, 1999) and $BVRIJHK$ (Bergeron, 2001) photometry. The red solid and black dotted lines represent the pure hydrogen models with and without the opacity from the red wing of the Ly α line, respectively. The fit parameters are $T_{\rm eff} = 5820$ K and $\log g = 8.30$. The dashed line represent the spectrum obtained when only H − H collisions are considered in the Ly α opacity calculation. All model spectra shown are computed from the same atmospheric structure.

$\log n_{\rm H} = 19.8$ and $\log n_{\rm H_2} = 19.0$. Despite the lower abundance of H_2, it is an important contributor to the Ly α line opacity in the far red wing (Fig. 50). Wolff et al. (2002) obtained a good fit of the UV and blue spectrum with a He-rich model with H/He $= 3 \times 10^{-5}$. They point out that such a low-H abundance fails to reproduce the Balmer lines of BPM 4729, however. Wolff et al. (2002) required a large amount of He to match the UV spectrum because the broadening of Ly α by collisions with He is weaker than with H or H_2 (Fig. 51). They also considered a pure hydrogen model but its Ly α line extends only up to ~ 2400 Å, corresponding to $E_{12} = 5.16$ eV in Fig. 48. In view of the difference between the potential curves for the $b\,^3\Sigma_u^+$ to $a\,^3\Sigma_g^+$ states of the H − H dimer (Fig. 48) this indicates that this particular transition was not included in the model of Wolff et al. (2002). The main reason for our success with a pure H model is our inclusion of the broadening of Ly α line by collisions with H_2 and using the $b^3\Sigma_u^+ \rightarrow a^3\Sigma_g^+$ transition for the H − H dimer.

We have also fitted $BVRIJHK$ photometry of most of the coolest hydrogen white dwarfs in the

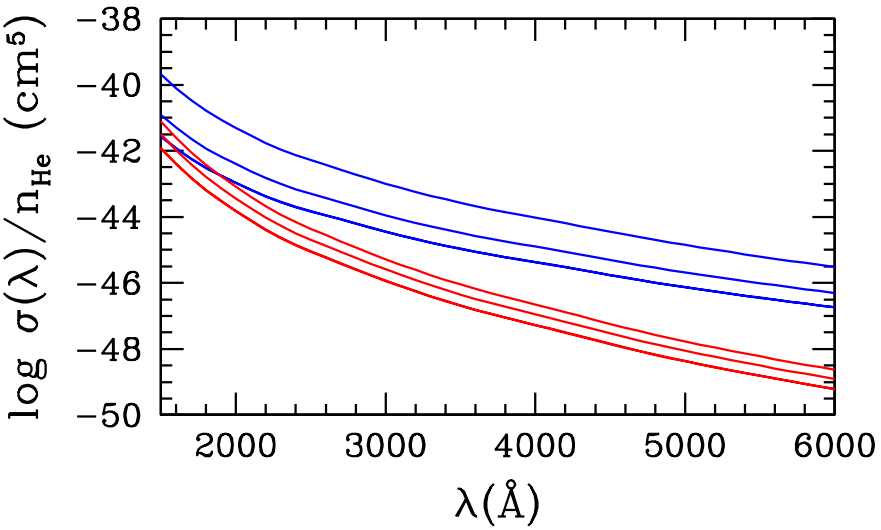

Figure 51: The absorption cross section of the Ly α line pressure broadened by collisions with He. Colors indicate the different T, where T equals, 6000 K (blue) and 4000 K (red). The sequence of curves is for $\rho = 0.1$, 0.5 and 1 g/cm^3 (from bottom to top). The low-density limit, where cross section is linear in $n_{\rm He}$, is recovered at $\rho \lesssim 0.1$ g/cm^3.

Bergeron et al. (2001) sample (chapter X). Two typical least-squares fits are shown in Fig. 52. Our models have no difficulty in reproducing the observed B flux and excellent fits are obtained. The importance of the Ly α line opacity in the models is revealed by comparing with fits of models that exclude this opacity source. The improvement in fitting the B flux with our Ly α opacity model is clearly visible. The success of the pure H models indicates that the Ly α red wing opacity is the missing blue opacity source in models of cool H-rich white dwarf atmospheres.

9.3 Ly α Red Wing Opacity in Dense Helium

The previous discussion has focused on Ly α broadening in pure H atmosphere. Broadening by collision with He may be significant in mixed He/H atmospheres rich in He, which can reach high densities (Koester & Wolff, 2000; Wolff et al., 2002). We applied the same formalism as described in §9.1, with the potential curves and dipole moments for the ground state and first excited state of the H – He dimer of Theodorakopoulos et al. (1987). In fluid He-rich atmospheres, we can no longer ignore correlations and we need to use the full $g(r)$ with partial thermal potential (Eq. 84) in the

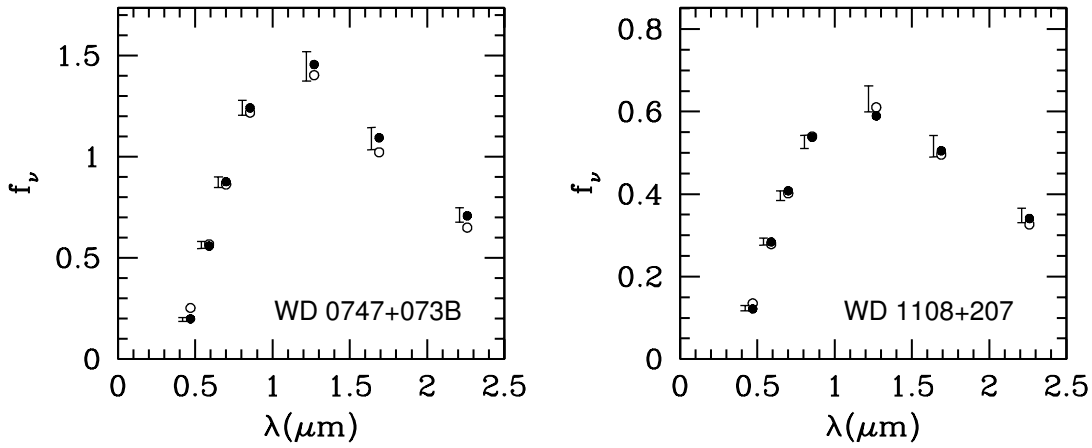

Figure 52: Fits to the spectral energy distributions of two very cool white dwarfs from the sample of Bergeron (2001). Bars represent the observed $BVRIJHK$ fluxes with $\pm 1\sigma$ errors (Bergeron, 2001). Circles (shifted by $+0.05\,\mu$m for clarity, represent the best fitting pure hydrogen models. Models with the Ly α opacity (filled circles) give the following ($T_{\rm eff}$, $\log g$): (4255, 7.78) for WD 0747+073B and (4708, 8.16) for WD 1108+207. Models computed *without* the Ly α opacity (open circles) give (4240, 7.75) for WD 0747+073B and (4584, 8.05) for WD 1108+207. The units of flux are $10^{-26}\,{\rm erg\,cm^{-2}\,s^{-1}\,Hz^{-1}}$.

calculation of dP_c (Eq. 194). As a consequence, the cross-section of Ly α pressure broadened by collisions with He atoms is no longer linear in $n_{\rm He}$. In this instance we computed the pair distribution function $g(r)$ by solving Ornstein-Zernike Eq. (91) in the PY approximation (§3.2). Fig. 51 shows the temperature and density dependence of the Ly α profile broadened by He. As partial thermal potentials in $g(r)$ tends to increase its value, dP_c increases and the absorption coefficient becomes larger at high densities. However, comparing results in Fig. 51 with those in Fig. 49, it is clear that the broadening by He is weaker than by H or H_2. Significant amounts of helium in the atmosphere is required (He/H $> 10^2$) for broadening by He to be dominant.

CHAPTER X

MODELS AND APPLICATIONS

The research effort presented so far aimed to model new dense matter physics to implement in cool white dwarfs atmospheres and spectra. In this chapter, we present the resulting atmosphere models and their application to an analysis of the samples of cool white dwarfs of Bergeron et al. (2001) and Bergeron et al. (2005). We also investigate the recent data from the Sloan Digital Sky Survey (SDSS) of Kilic et al. (2006) and Harris et al. (2006). Our analysis reveals a new picture for the evolution of their atmospheres.

10.1 Cool White Dwarf Atmosphere Models

We have included all the effects discussed in Chapters II–IX in our white dwarf atmosphere code, and calculated grids of $T - P$ profiles and spectra. Full sequences were calculated for pure H, He/H = 1, and pure He compositions. A sequence covers $T_{\rm eff}$ from 6000 K to 3000 K in steps of 250 K and the gravity, $\log g$, varies from 7.0 to 9.0 in steps of 0.5. In Figs. (53) and (54) we present the atmosphere profiles. The profiles have two distinct parts characterized by their temperature gradients, $\nabla = d\ln T/d\ln P$ (the inverse of the slope in the $\log P$ vs. $\log T$ figures). In the deeper part of the models, ∇ is large and this corresponds to the convective zone, where $\nabla \sim \nabla_{\rm ad}$ (§2.3). The photosphere is always localized deep in the convective zone. The outer part of the models (lower P and ρ) is always radiative and it is characterized by a smaller temperature gradient ($\nabla < \nabla_{\rm ad}$). Compared with the pure helium models of Bergeron et al. (1995a), our models have a much higher ionization fraction (and therefore, much higher opacity) resulting in much lower P and ρ. Our pure He models do not reach conditions as extreme as those found in previous models that motivated part of our work. Nevertheless, the models reach $P \sim 1$ Mbar and $\rho = 1\,{\rm g/cm^3}$, where the fluid effects we have modeled remain important.

In the radiative zone, as a consequence of the refraction, ∇ remains finite rather than decreasing to zero as in the Bergeron et al. (1995a) models or in the hydrogen-rich models. This result is an effect of total internal reflection (Chapter IV).

Adding hydrogen, which is more opaque than helium, the atmospheric pressure and density drops significantly below that of pure He models. The bump visible in the profile for the model with $T_{\rm eff} = 5000$ K and He/H = 1 is related to the existence of multiple solutions to the equation of radiative equilibrium in a narrow region of ($T_{\rm eff}$,g,He/H) parameter space. This bump also occurs in the models of Bergeron et al.

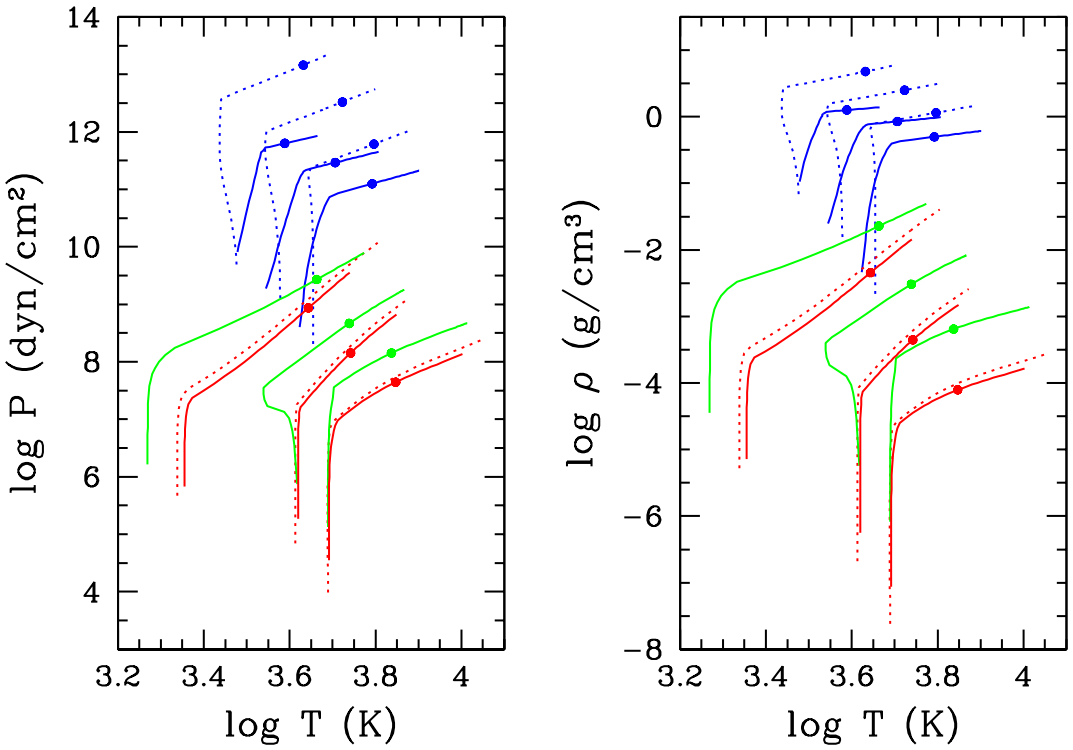

Figure 53: Structures of atmosphere models with $T_{\rm eff}$ = 6000 K, 5000 K, and 4000 K (from right to left), and compositions: pure H (red), He/H = 1 (green), and pure He (blue). The gravity is $\log g = 8$. The dotted lines represent the models of Bergeron et al. (1995a). Filled circles indicate the position of the photosphere ($\tau_{\rm R} = 2/3$).

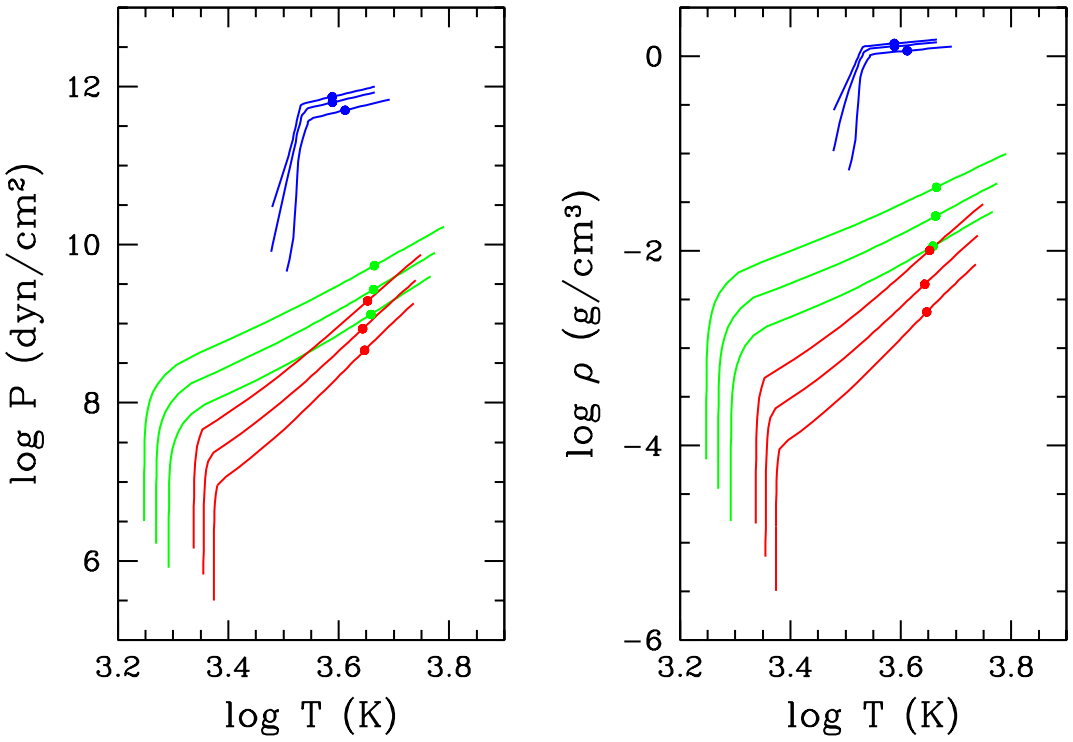

Figure 54: Structures of atmosphere models with $T_{\rm eff} = 4000\,{\rm K}$, compositions: pure H (red), He/H = 1 (green), and pure He (blue), and gravity, $\log g = 7.5$, 8, and 8.5 from right to left. Filled circles indicate the position of the photosphere ($\tau_{\rm R} = 2/3$).

(1995a) who discuss this problem extensively. However, as this jump between solution occurs well above the photosphere ($\tau_{\rm R} < 10^{-4}$) it has no effect on the spectrum. The non ideal corrections in dense helium become significant for $\rho \gtrsim 0.1\,{\rm g/cm^3}$. Such physical conditions are reached in models with He/H > 10 (Fig. 18). On the other hand, the pure H models are not very different from those of Bergeron et al. (1995a). All models have somewhat lower pressures and densities, that is a result of the introduction of the Ly α opacity.

The dependence of the profiles on gravity is shown in Fig. (54). As a consequence of the hydrostatic equilibrium (Eq. 3), a higher gravity results in higher pressures and densities. The pure helium models are less sensitive to increases in gravity as even a small increase in density results in a significant increase in the opacity (He^- ff) because of the onset of pressure ionization in the chemical model for helium (§6.5).

We now turn to the impact of the new physics on the synthetic spectra of cool white dwarfs. In Figs. (55)–(58), we present how the spectrum changes with the He/H ratio. At $T_{\rm eff} = 4000\,{\rm K}$ the synthetic flux of atmospheres with hydrogen is redistributed to the shorter wavelengths because of the strong collision induced absorption (CIA) of molecular hydrogen in the infrared, present even in atmospheres that are highly enriched in helium (e.g. He/H $= 10^4$). The flux suppression at $\sim 2.3\,\mu$m, where the CIA opacity is strongest (Fig. 59), is a signature of this absorption mechanism. The spectra of pure He models are close to those of black bodies because the nearly grey He^- ff opacity dominates at all wavelengths (Chapter VI, Fig. 59). At $T_{\rm eff}$ of 5000 K and 6000 K, the flux suppression in the infrared decreases as H_2 dissociates. The suppression of flux around $0.3\,\mu$m compared to the black body is caused by strong absorption in the red wing of Lyman α (Chapter IX).

Figure (58) shows how the spectra change with gravity. There is no effect on the spectra of pure-He models. Higher gravity leads to higher densities, more pressure ionization, and a larger He^- ff opacity. Because the frequency dependence of the opacity is not affected, the emergent spectrum remains the same. This result means that the gravity of a pure He atmospheres of white dwarfs can not be determined from its spectrum alone. On the other hand, in models with hydrogen, a higher gravity increases the abundance of H_2 and the CIA opacity in the infrared. Therefore, the suppression of flux at long wavelengths is larger with increased gravity.

The most important aspect of this work is the application of the new models to the analysis of the data. In the rest of this chapter we present our reexamination of samples of cool white dwarfs.

10.2 Analysis of Data

10.2.1 Color-color Diagrams

Color-color diagrams allow a broad comparison of our models with large samples of stars to identify trends. For this purpose, we computed magnitudes and colors in the Johnson-Cousins and the SDSS AB magnitude systems from the synthetic spectra following the method given in Appendix B. Figures (60)–(62) show the samples of cool white dwarfs of Bergeron et al. (2001), and a combination of two samples culled from the Sloan Digital Sky Survey (SDSS) (Kilic et al., 2006; Harris et al., 2006). The atmospheric composition of the stars in the first sample, as determined by Bergeron et al. (2001), is also indicated. Because we are concerned with atmospheres composed of H and He only, we have kept only the DA and DC stars from these samples. In the BVI (Fig. 60) and ugz (Fig. 62) diagrams, cool white dwarfs form a well-defined sequence that is very well reproduced by our pure H models. No sequence is apparent in the JHK data (Fig. 61) but these is a generally better agreement with the pure H sequence. These three diagrams indicate that there are no pure He star with $T_{\rm eff} \lesssim 4500\,{\rm K}$. All other color-color diagrams involving the $BVRIJHK$ and $ugriz$ colors also lead to that conclusion. On the other hand, the sequence of pure helium models of Bergeron et al. (1995a) used in the analysis of Bergeron et al. (1997, 2001, 2005) reproduces the observed sequence in the BVI color-color diagram.

The pure He models of Bergeron et al. (1995a) are based on a simpler model for the ionization of helium that predicts a much lower ionization fraction and $\rm He^-$ ff opacity (Fig. 35). Consequently, Rayleigh scattering is a significant source of opacity in their models at short wavelengths ($\sigma_\nu \sim \nu^4$) that mimics the opacity from the red wing of the Ly α line in our H models. The net result is that the Bergeron et al. (1995a) helium sequence follows the BVI data (and our H sequence) down to $T_{\rm eff} \sim 4000\,{\rm K}$. In our pure He models, $\rm He^-$ ff dominates all other sources of opacity, a firm conclusion from our extensive study of the ionization balance of helium and our corrections to the Rayleigh scattering cross section (Chapter VI). The colors of the pure H sequence are close to those of black bodies and deviate from the observed white dwarf sequence.

On the basis of the location of the pure H and pure He model sequences in the color-color diagrams (Figs. (60)-(62)) it appears that white dwarfs cooler than $T_{\rm eff} < 5000\,{\rm K}$ have either pure H or H-rich atmospheres.

10.2.2 Fits to the SED

Color-color diagrams only involve three points along the SED of a star and are not very rigorous tools for the analysis of stars. To determine the composition, effective temperature and gravity of individual stars,

we fit the entire optical and near infrared SED following the method of Bergeron et al. (1997). We fitted magnitudes synthesized from our model spectra to the observed $BVRIJHK$ photometry of Bergeron et al. (2001) and Bergeron et al. (2005). The synthetic magnitudes, $m_{\rm syn}$ are computed at the surface of the star and are related to the apparent magnitudes, m by

$$m = m_{\rm syn} + m_{\rm c}. \tag{200}$$

For each star, the constant m_c – obtained by a least-square fit of the photometry – and is related to the distance to the star D and its radius R by

$$m_{\rm c} = 5 \log \frac{D}{R}. \tag{201}$$

The distance D is obtained from the parallax. The radius is then calculated from the fitted value of m_c. The corresponding gravity is obtained from white dwarf evolution sequences which provide a $g(R, T_{\rm eff})$ relation. The fitting procedure goes in the following way. For a given g, the $BVRIJHK$ magnitudes are least-squares fitted for the parameters $T_{\rm eff}$, He/H composition and $m_{\rm c}$. For fits with either the pure H or the pure He models we keep the He/H ratio constant, and fit $T_{\rm eff}$ and m_c only. Then using Eq. (201) and the distance D, we obtain R and a new gravity g. The procedure is repeated until it has converged on a value of g, which usually requires 5 to 10 iterations. Uncertainties in the fitted parameters come mostly from the uncertainties in the parallax measurements and should be similar to those of Bergeron et al. (2001, 2005), typically $\pm 100\,$K in $T_{\rm eff}$, and ± 0.1 in $\log g$. In the fits with mixed composition uncertainty in He/H ratio is ± 0.1. For stars with unknown parallax we assume a fixed gravity $\log g = 8$. We use cooling sequences kindly provided by G. Fontaine for white dwarfs with a core composition of C/O = 1, $M_{\rm He} = 10^{-2} M$, and $M_{\rm H} = 0$ and $10^{-4} M$ (Fontaine et al., 2001) for fits with the pure He and the pure H atmospheres, respectively. For stars with mixed composition we use the cooling sequence with $M_{\rm H} = 10^{-4} M$, which is appropriate for the compositions we find (He/H $\sim$ 1).

Fits to the SED of selected stars from the samples of Bergeron et al. (2001) and Bergeron et al. (2005) are presented in Figures (63–65) and Tables 3–5. Figures (63) and (65) shows fits of several stars assigned pure H composition by Bergeron et al. (2001) and Bergeron et al. (2005) that span $T_{\rm eff} = 5820\,$K to $3970\,$K. Best fits of models with and without the Ly α opacity are shown, again demonstrating the much improved quality of the fits to the B band flux ($0.43\,\mu$m) when the Ly α opacity is included (Fig. 49). We obtain

very good fits to all the stars assigned a H composition by Bergeron et al. (2001, 2005), in all cases we also find that a pure H composition provides the best fit, as suggested by the color-color diagrams (Figs. 60–62). Figures (64) and (65), we show fits of stars that were fitted with pure He models ("He-rich") by Bergeron et al. (2001) and Bergeron et al. (2005). We are unable to fit them with either pure H or pure He models, except for WD 0651−479, WD 2316−064 and WD 0222+648, which can be fit with pure H atmospheres. We obtain good fits of the SED of the other stars with models of mixed He/H composition [1] and find that they all have modest mixing ratios of He/H < 2. This result is not surprising as the stars follow the pure-hydrogen sequence at color-color diagrams (Fig. 60-62). The parameters of our best fits to all the DA and DC stars in both samples are given in Table 5.

Figures (66) and (67) show how our determinations of $T_{\rm eff}$ and gravity compare with those of Bergeron et al. (2001). We first discuss the pure H stars. The agreement in $T_{\rm eff}$ is excellent and no systematic difference is seen. Our gravities agree within the uncertainties with those of Bergeron et al. (2001) for individual stars, but show a systematic shift toward higher values by ~ 0.04 dex. As our $T_{\rm eff}$ agree very well with those of Bergeron et al. (2001), this difference may be a result of a recent update in the calibration spectrum of Vega used to calculate the synthetic magnitudes (Appendix B).

For the stars previously thought to have helium atmospheres (Bergeron et al., 2001) fits give a systematically lower $T_{\rm eff}$ (by $\sim 200-300$ K) and lower gravities (~ 0.2 dex). This disagreement is a direct consequence of the change in composition from pure He to pure H or He/H ~ 1 (for $T_{\rm eff}$) and the corresponding change in the cooling sequences from stars with He envelope to stars with H envelope for the gravity.

10.3 Implications

The most important conclusion of our analysis is that there are no stars with pure He atmospheres below 6000 K in the samples we analyzed. All the stars have pure H atmospheres, except for $\sim 25\%$ that have mixed composition atmospheres with He/H ~ 1, a different picture, than those deducted by Bergeron et al. (2001). This result we show in Figs. 68 and 69, where we present the effective temperature distribution of white dwarfs with different compositions as determined by us, and by Bergeron et al. (2001), and the updated BVI color-color diagram. DB stars with pure helium atmospheres exist at $T_{\rm eff} > 12000$ K, yet we find no single white dwarf below 4500 K. Evidently, the atmospheric composition of a single white dwarf can change from helium to hydrogen as it cools. This change may occur by the accretion of hydrogen from the

[1] We have found that for modest He/H ratios ($0 \leq$ He/H $\lesssim 2$), the synthetic magnitudes are linear in He/H. To reduce the computational burden of generating grids of models for many different compositions, we use such linear relations to estimate the magnitudes of mixed composition models other than He/H = 0 and 1.

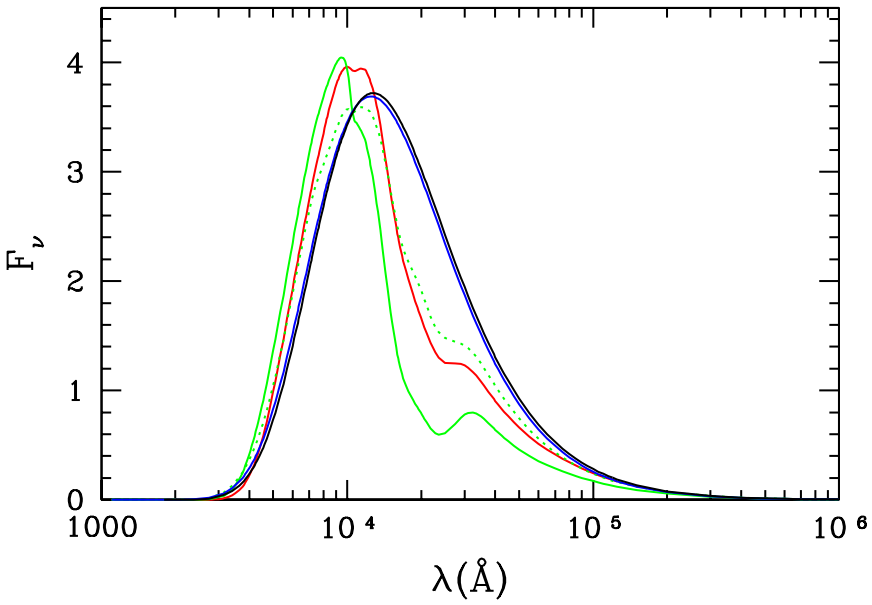

Figure 55: Model spectra with $T_{\rm eff} = 4000\,{\rm K}$, $\log g = 8$, and various compositions: pure H (red), He/H = 1 (solid green), He/H = 10^4 (dotted green), pure He (blue), and black body (black). The units of flux are $10^{-26}\,{\rm erg\,cm^{-2}\,s^{-1}\,Hz^{-1}}$.

Table 3. Best fit pure H models parameters for the stars in Fig. (63) and (65).

WD	$T_{\rm eff}$ (K)	$\log g$ (cgs)	$T_{\rm eff}$ (K)	$\log g$ (cgs)
	models with Ly α		models without Ly α	
2347+292	5820	7.88	5890	7.87
0503−174	5310	7.67	5330	7.64
0657+320	4830	8.03	4700	7.90
1820+609	4760	7.87	4610	7.72
1300+263	4290	8.10	4330	8.11
1247+550	3960	7.55	4070	7.65
2346−550	5240	8.00	5170	8.00
0011−399	4530	8.00	4400	8.00
0343−363	4250	8.00	4230	8.00

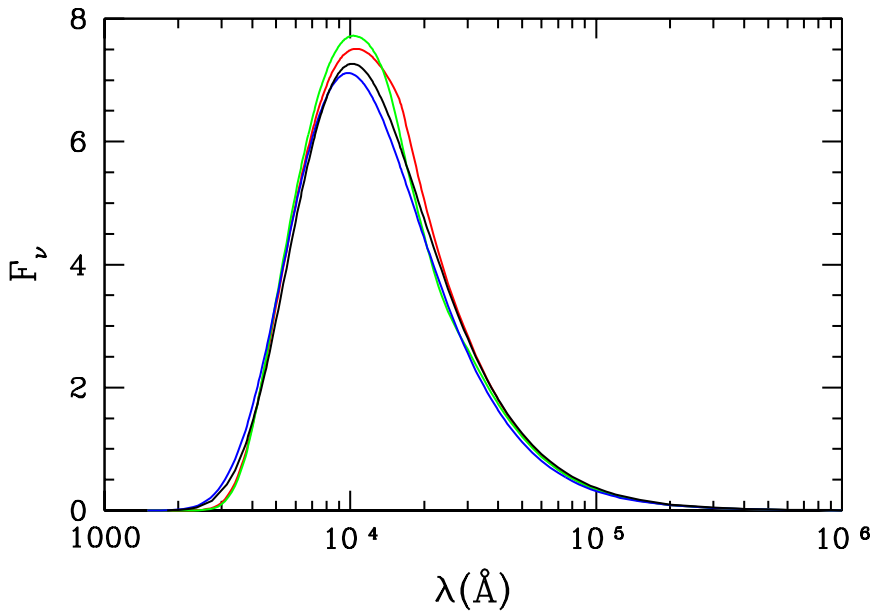

Figure 56: Model spectra with $T_{\rm eff} = 5000\,{\rm K}$, $\log g = 8$, and various compositions: pure H (red), He/H = 1 (green), pure He (blue), and black body (black). The units of flux are $10^{-26}\,{\rm erg\,cm^{-2}\,s^{-1}\,Hz^{-1}}$.

Table 4. Parameters of the best fitting models in Fig. 64 and 65. In all cases the best fit is with mixed He/H composition.

WD	$T_{\rm eff}$ (K)	$\log g$ (cgs)	$T_{\rm eff}$	$\log g$	He/H	$T_{\rm eff}$	$\log g$
	H models		He/H models			He models	
2345−447	5670	8.85	5560	8.82	1.82	5480	8.74
0552−041	5170	8.40	5070	8.34	1.35	5020	8.27
1444+174	5060	8.46	4980	8.42	0.76	4930	8.35
0747+073A	4730	7.98	4730	7.99	0.44	4690	7.91
0651−479	4290	7.76	4320	7.79	0.05	4440	7.84
0222+648	4260	7.84	4260	7.84	0.00	4260	7.79
0042−064	5140	8.00	5110	8.00	1.39	4960	8.00
0120−280	4810	8.00	4810	8.00	0.41	4710	8.00
2316−064	4510	8.00	4520	8.00	0.04	4510	8.00

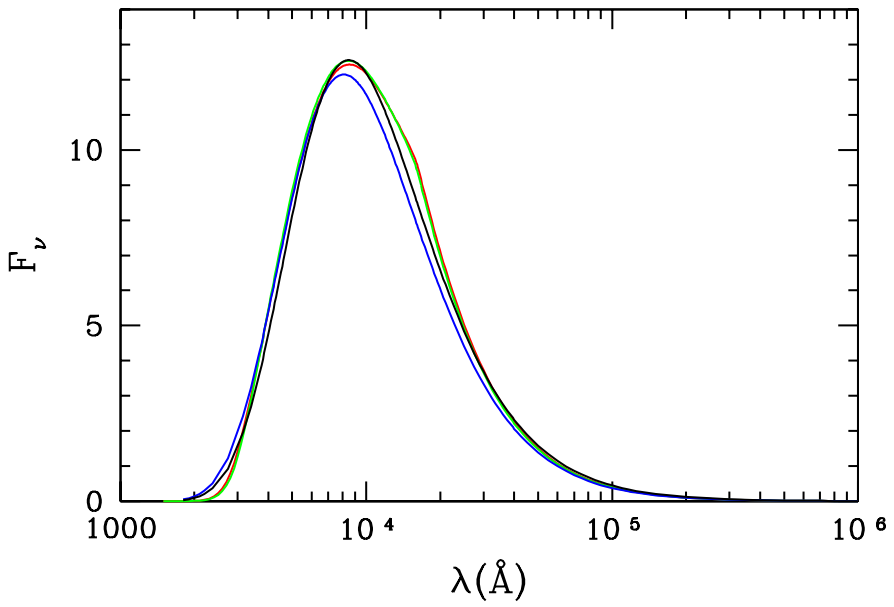

Figure 57: Model spectra with $T_{\rm eff} = 6000\,{\rm K}$, $\log g = 8$, and various compositions: pure H (red), He/H = 1 (green), pure He (blue), and black body (black). The units of flux are $10^{-26}\,{\rm erg\,cm^{-2}\,s^{-1}\,Hz^{-1}}$.

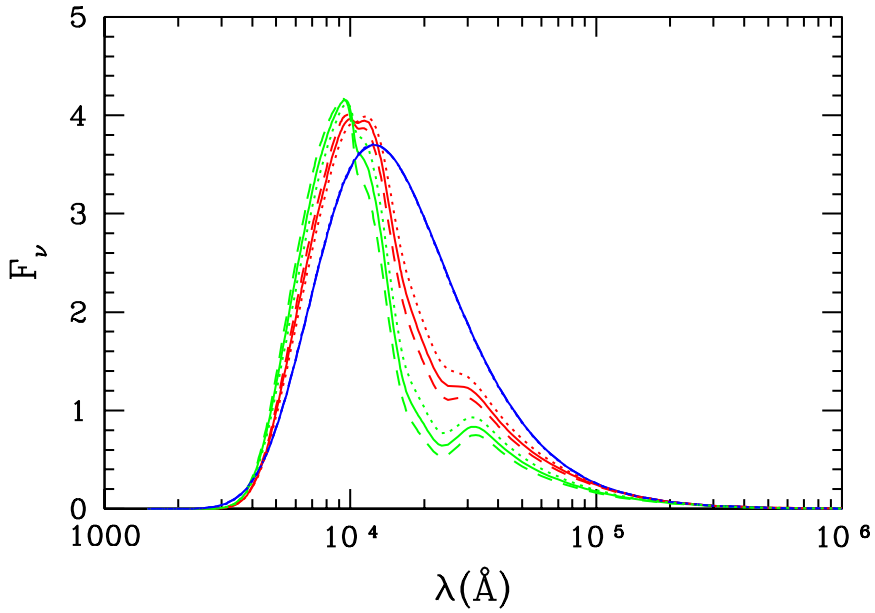

Figure 58: Model spectra of white dwarfs with $T_{\rm eff} = 4000\,{\rm K}$ (solid), various compositions: pure H (red), He/H = 1 (green), pure He (blue), and gravities $\log g = 7.5$ (dotted), 8 (solid), and 8.5 (dashed). The units of flux are $10^{-26}\,{\rm erg\,cm^{-2}\,s^{-1}\,Hz^{-1}}$.

Table 5. Fits to the DA and DC white dwarfs of Bergeron et al. (2001) and Bergeron et al. (2005).

WD	$T_{\rm eff}$ (K)	$\log g$ (cgs)	He/H	WD	$T_{\rm eff}$	$\log g$	He/H
0011−399	4530	8.00	0.00	0657+320	4830	8.03	0.00
0029−032	4620	8.00	0.17	0743−340	4430	7.78	0.29
0038−345	6330	8.43	0.00	0747+073A	4730	7.99	0.44
0041−286	4500	8.00	0.37	0747+073B	4250	7.78	0.00
0042−064	5110	8.00	1.39	0752−676	5760	8.28	0.00
0042−337	4020	8.00	0.00	1108+207	4710	8.17	0.00
0115−270	4910	8.00	0.00	1136−286	4550	9.10	0.00
0117−145	5090	7.78	0.00	1247+550	3960	7.55	0.00
0120−280	4810	8.00	0.41	1257+037	5630	8.23	0.00
0133−548	4640	8.00	0.00	1300+263	4290	8.10	0.00
0202−055	4110	8.00	0.00	1310−472	4100	8.09	0.00
0212−420	4820	8.00	0.42	1313−198	5340	8.39	1.76
0222+648	4260	7.84	0.00	1334+039	4960	7.97	0.00
0225−446	4680	8.00	0.00	1345+238	4520	7.78	0.00
0230−144	5490	8.18	0.00	1444−174	4980	8.42	0.76
0245+541	5060	8.22	0.00	1656−062	5550	8.10	0.00
0338−331	4390	8.00	0.00	1820+609	4760	7.87	0.00
0343−363	4250	8.00	0.00	2002−110	4640	8.25	0.41
0350−566	3830	8.00	0.00	2054−050	4260	7.84	0.00
0357+081	5490	8.09	0.00	2107−216	5890	8.48	0.00
0433+270	5650	8.21	0.00	2239−199	5220	8.00	0.13
0503−174	5310	7.67	0.00	2256−467	4820	8.00	0.00
0551+468	5270	8.01	0.00	2316−064	4520	8.00	0.04
0552−041	5070	8.34	1.35	2345−447	5560	8.82	1.82
0553+053	5800	8.26	0.00	2346−550	5240	8.00	0.00
0618+067	5940	8.32	0.00	2347+292	5820	7.88	0.00
0651−479	4320	7.79	0.05	2354−211	4140	8.00	0.00

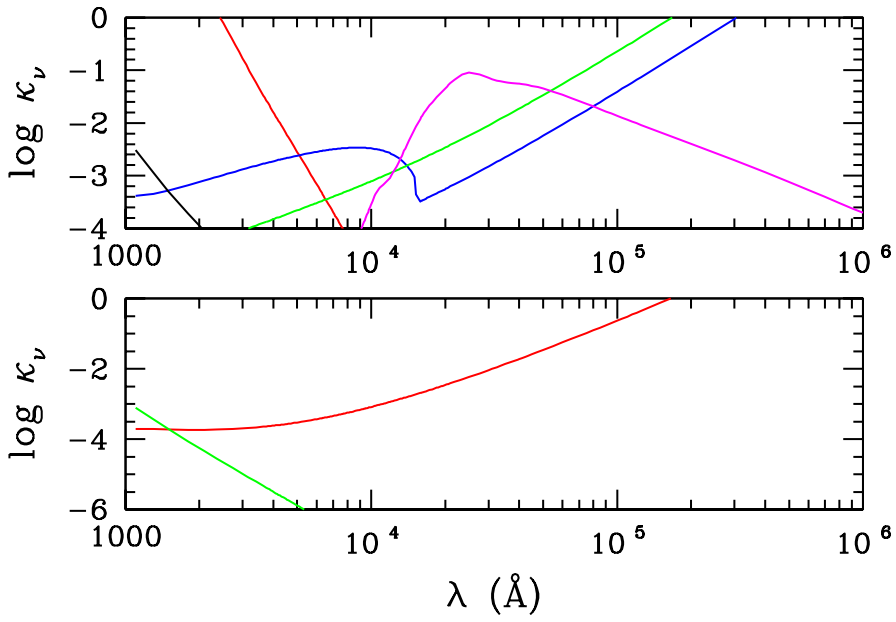

Figure 59: The most important sources of opacity at the photosphere of pure hydrogen (upper panel) and pure helium (lower panel) white dwarf atmosphere models of $T_{\rm eff} = 4000\,{\rm K}$ and $\log g = 8$. Upper panel: H Ly α red wing (red), H^- bb & bf (blue), H_2 CIA (magenta), H_2^- ff (green), and Rayleigh scattering of H_2 and H (black). Lower panel: He^- ff (red) and Rayleigh scattering from He atoms (green). The units of κ_ν are $\rm cm^2/g$.

interstellar medium (Bergeron et al., 1997). Figure 70 shows the He/H ratio versus $T_{\rm eff}$ for stars with mixed composition. There is a striking correlation where the He/H ratio decreases with decreasing $T_{\rm eff}$, with all stars turning to pure H composition at $T_{\rm eff} \sim 4500\,{\rm K}$. The possibility that this correlation is an artifact of the models is a concern. We note that over the entire range of $T_{\rm eff}$ shown in Fig. 70 there are many more stars that are fitted very well with our pure H models. On the other hand, the fits with the mixed composition models tend to overestimate the flux in the B band (Fig. 61 and 62), which points to the modeling of the Ly α profile as a possible culprit. The fact that we fit very well stars with pure H atmospheres over the same range of $T_{\rm eff}$ demonstrates the validity of our model for Ly α broadening by H and H_2 under these conditions. In mixed composition models, broadening by collisions with He also contributes but this is relatively easy to model. Furthermore, models with He/H ~ 1 reach densities of at most $0.03\,{\rm g/cm^3}$ (Fig. 18) where our model should work well. Perhaps this result is caused by inadequate CIA opacities in the mixed composition models. For the rest of the discussion, we consider that the correlation between composition and $T_{\rm eff}$ is

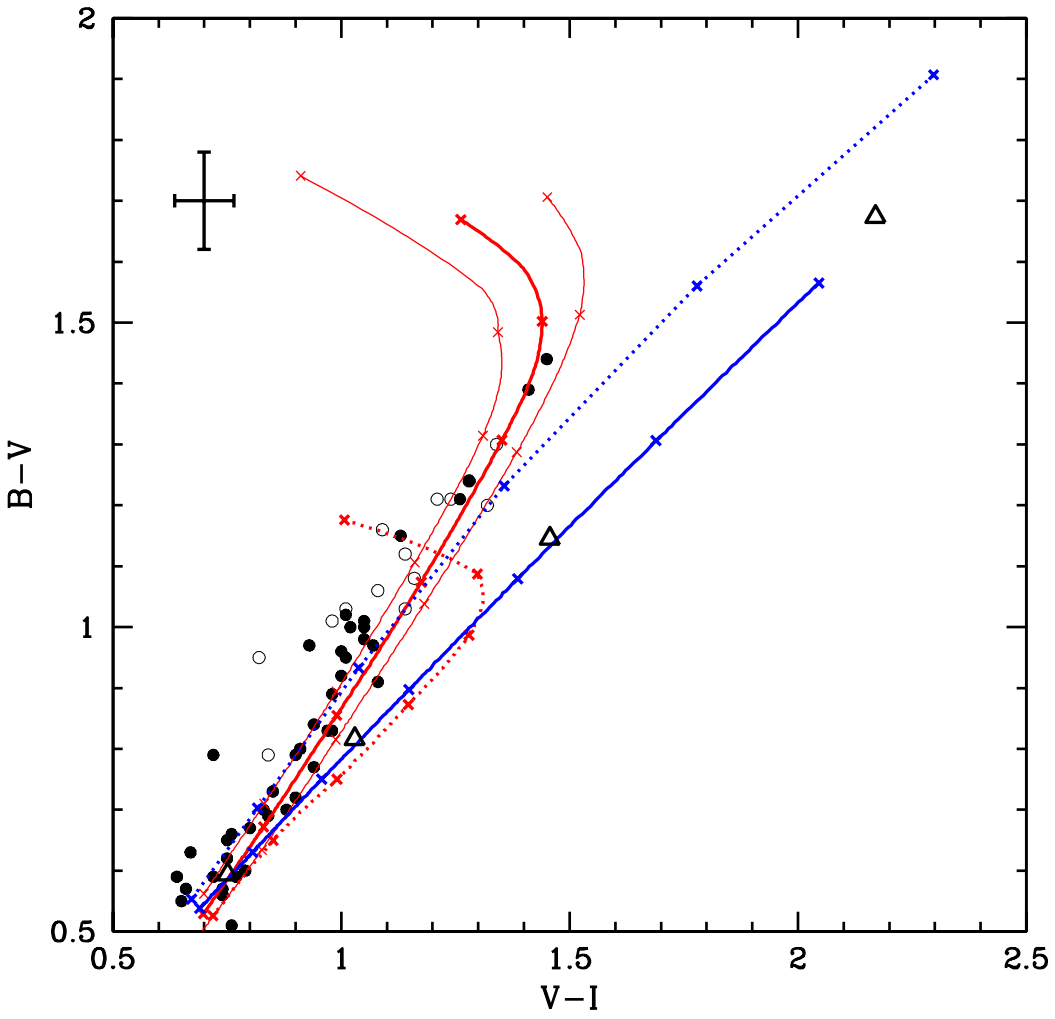

Figure 60: Color-color diagram in optical photometry for cool white dwarfs from the sample of Bergeron et al. (2001). The composition as determined by Bergeron et al. (2001) is shown by filled circles (hydrogen-rich) and open circles (helium-rich), and the photometric uncertainties are shown by the error bar in the upper left. The lines represent the synthetic colors of the models: pure hydrogen with the Ly α line opacity (red, solid) and without (red, dotted), our pure He sequence (blue, solid line), and the pure He models of Bergeron et al. (1995a) (blue, dotted). The $T_{\rm eff}$ along each curve is indicated by crosses at 6000 to 3000 K from bottom to top, in steps of 500 K. All models shown by thick lines have $\log g = 8$. The thin red lines indicate the new pure hydrogen models of $\log g = 7$ (right) and $\log g = 9$ (left). The corresponding colors of black bodies are shown by open triangles (in steps of 1000 K). DQ, DZ, and known or suspected double degenerates stars have been removed from the samples.

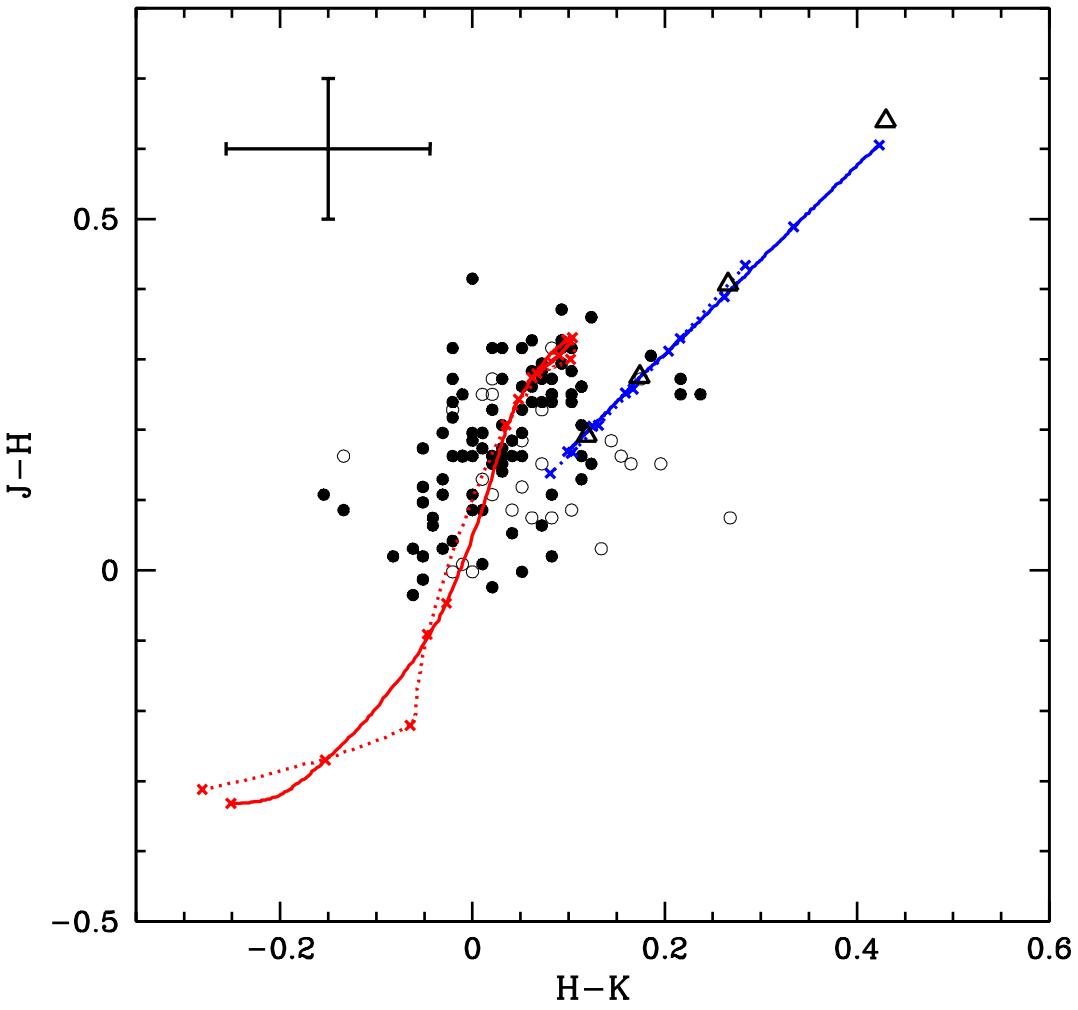

Figure 61: Infrared color-color diagram for cool white dwarfs from the sample of Bergeron et al. (2001). The composition as determined by Bergeron et al. (2001) is shown by filled circles (hydrogen-rich) and open circles (helium-rich) and the photometric uncertainties are shown by the error bar in the upper left. The lines represent the synthetic colors of the models: pure hydrogen with the Ly α line opacity (red, solid) and without (red, dotted), our pure He sequence (blue, solid line), and the pure He models of Bergeron et al. (1995a) (blue, dotted). The $T_{\rm eff}$ along each curve is indicated by crosses at 6000 to 3000 K in steps of 500 K from top to bottom for the pure hydrogen sequences, and from bottom to top for the pure helium sequence. All models have $\log g = 8$. The corresponding colors of black bodies are shown by open triangles (in steps of 1000 K). DQ, DZ, and known or suspected double degenerates stars have been removed from the samples.

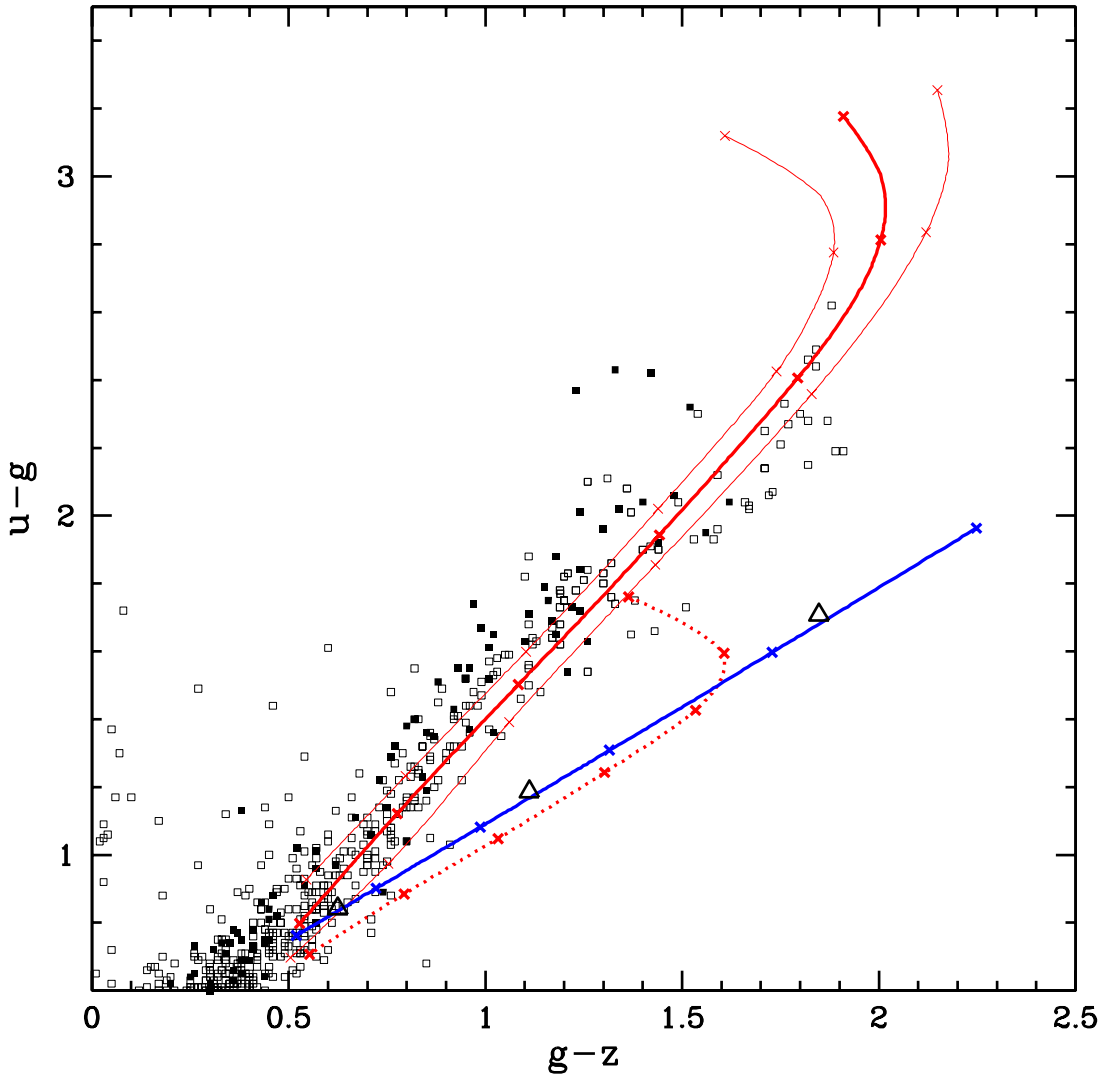

Figure 62: Color-color diagrams for cool white dwarfs for the SDSS white dwarfs sample of Kilic et al. (2006) (filled squares) and Harris et al. (2006) (open squares). The photometric error bars vary widely from star to star in these two samples and are not shown. The lines represent the synthetic colors of the models: pure hydrogen with the Ly α line opacity (red, solid) and without (red, dotted), our pure He sequence (blue, solid line), and the pure He models of Bergeron et al. (1995a) (blue, dotted). The $T_{\rm eff}$ along each curve is indicated by crosses at 6000 to 3000 K from bottom to top, in steps of 500 K. All models shown by thick lines have $\log g = 8$. The thin red lines indicate the new pure hydrogen models of $\log g = 7$ (right) and $\log g = 9$ (left). The corresponding colors of black bodies are shown by open triangles. DQ and DZ stars have been removed from the samples.

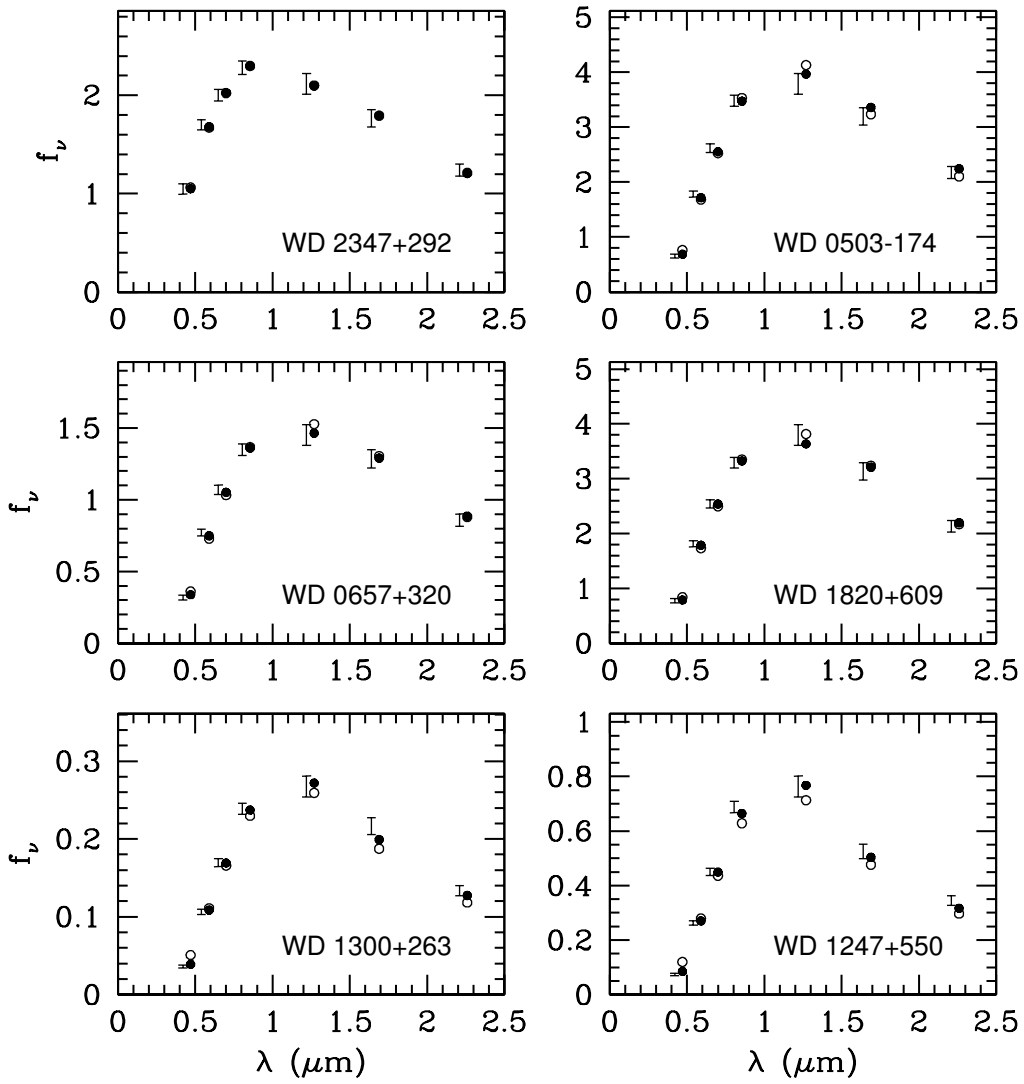

Figure 63: Fits with pure H models with (filled circles) and without (open circles) Lyman α opacity (Chapter IX) to the spectral energy distribution of cool white dwarfs classified as stars with hydrogen atmospheres by Bergeron et al. (2001). The parameters of the fits are given in Table 3. The units of flux are $10^{-26}\,\mathrm{erg\,cm^{-2}\,s^{-1}\,Hz^{-1}}$. The data are represented by $\pm 1\sigma$ error bars. The synthetic colors are shown shifted by $0.05\,\mu$m to the right for clarity.

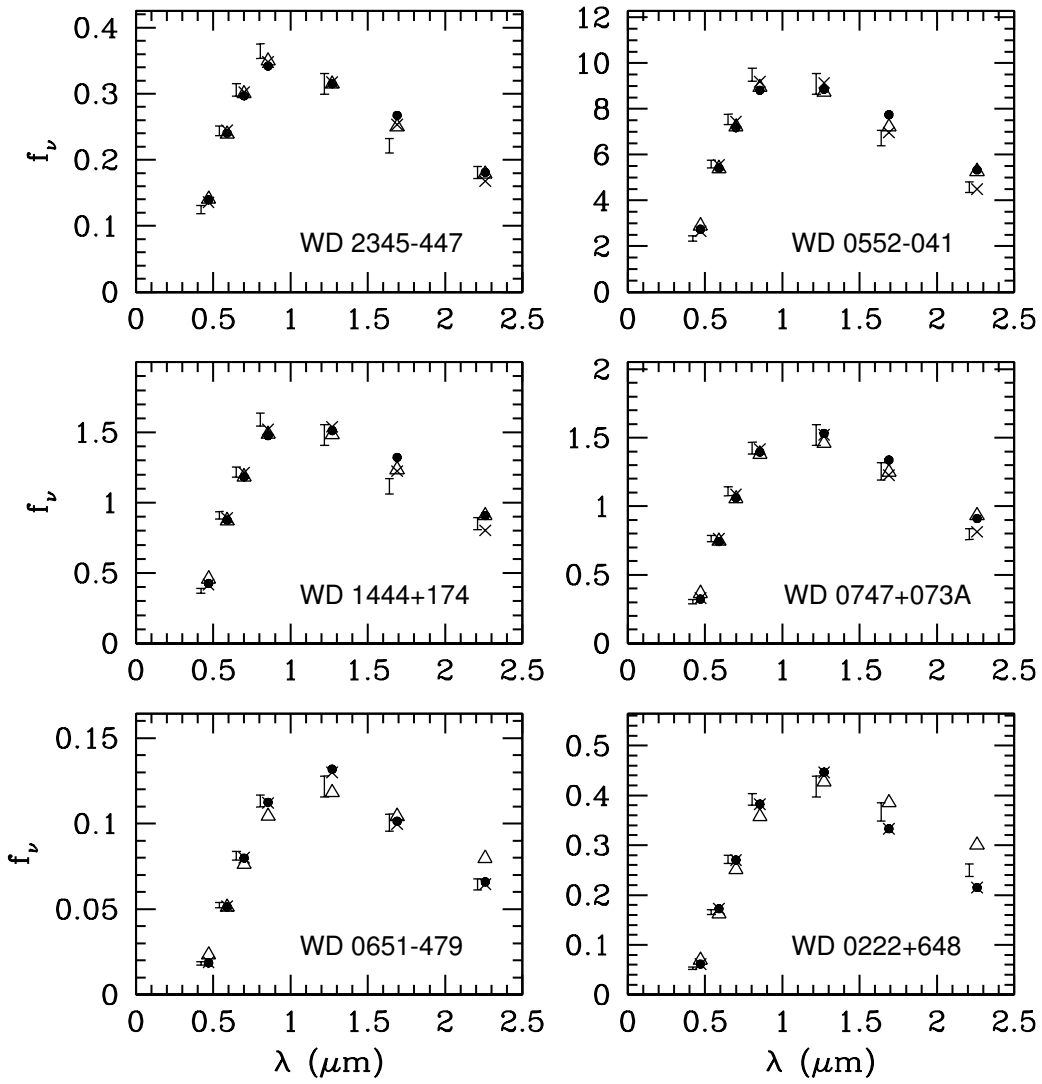

Figure 64: Fits with pure H (filled circles), mixed He/H composition (crosses), and pure He (open triangles) models, to the spectral energy distribution of cool white dwarfs classified as stars with helium atmospheres by Bergeron et al. (2001). The parameters of the fits are given in Table 4.The units of flux are $10^{-26}\,\mathrm{erg\,cm^{-2}\,s^{-1}\,Hz^{-1}}$. The data are represented by $\pm 1\sigma$ error bars. The synthetic colors are shown shifted by 0.05 μm to the right for clarity.

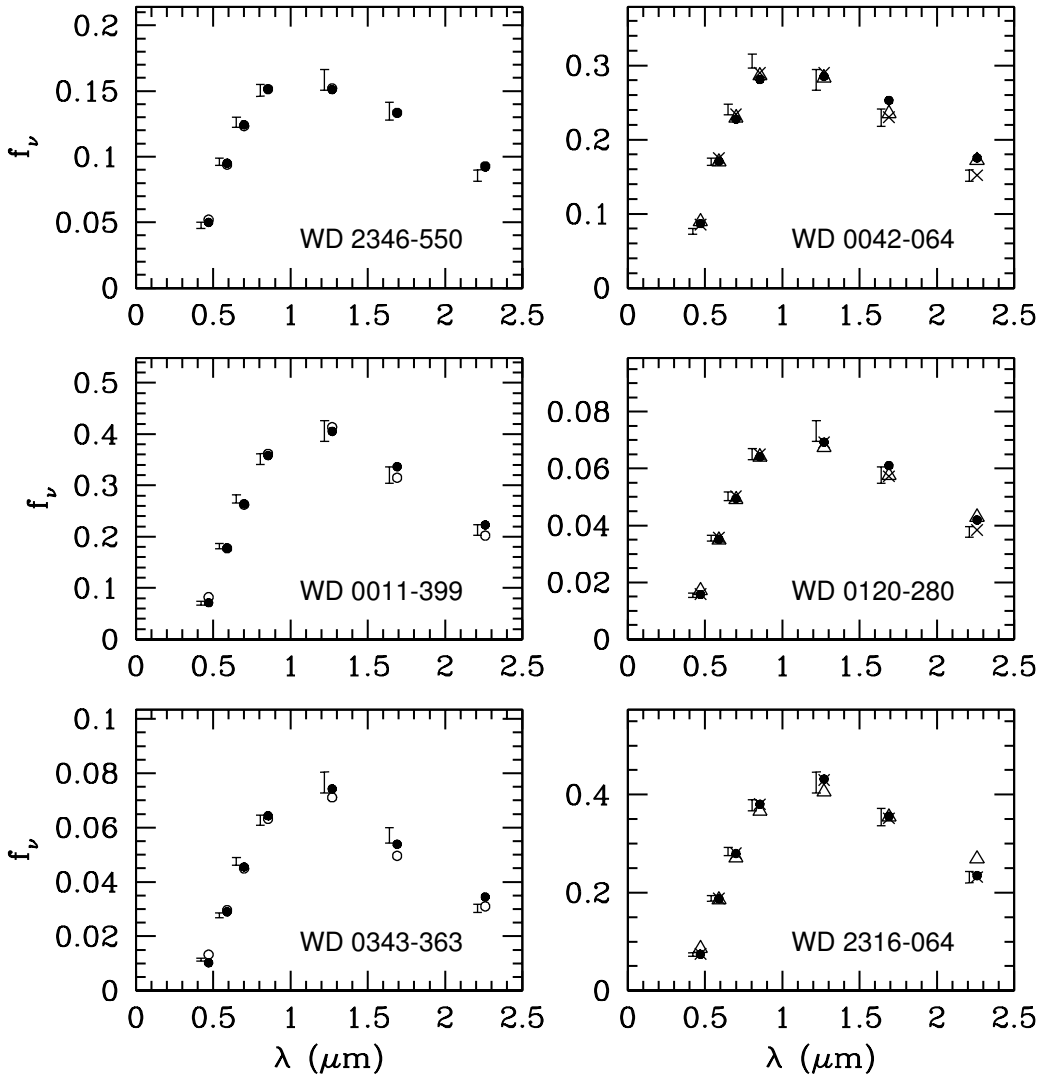

Figure 65: Left panels: Fits with pure H models with (filled circles) and without (open circles) Lyman α opacity (Chapter IX) to the spectral energy distribution of cool white dwarfs classified as stars with hydrogen atmospheres by Bergeron et al. (2005). Parameters of the fits are given in Table 3. Right panels: Fits with pure H with Ly α (filled circles), mixed He/H composition (crosses), and pure He (open triangles) models, to the spectral energy distribution of cool white dwarfs classified as stars with helium atmospheres by Bergeron et al. (2005). The parameters of the fits are given in Table 4. The units of flux are $10^{-26}\,\mathrm{erg\,cm^{-2}\,s^{-1}\,Hz^{-1}}$. The data are represented by $\pm 1\sigma$ error bars. The synthetic colors are shown shifted by $0.05\,\mu$m to the right for clarify.

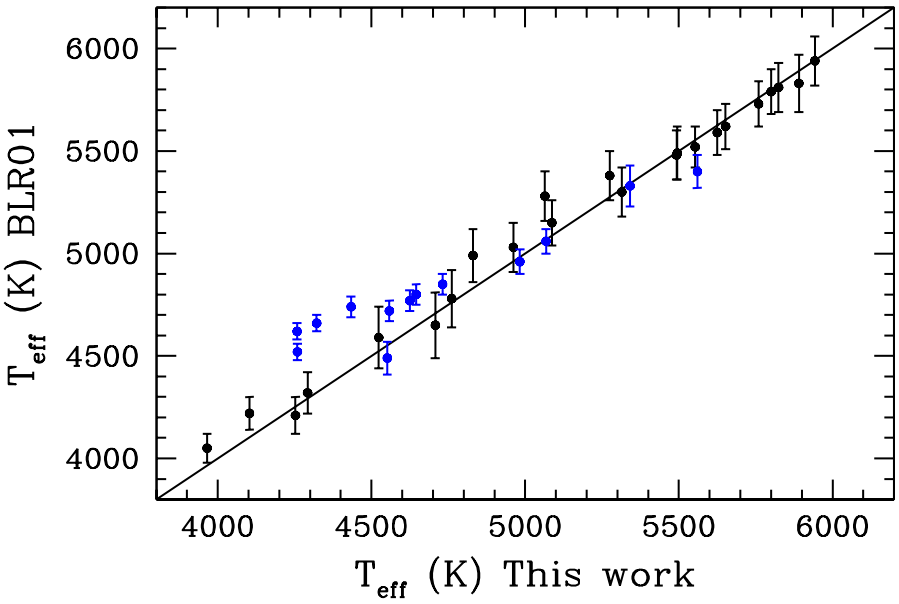

Figure 66: Comparison of $T_{\rm eff}$ obtained by fits of our models and those obtained by Bergeron et al. (2001) (BLR01) for stars with H-rich (black) and He-rich (blue) atmospheres as determined by Bergeron et al. (2001). The uncertainties calculated by Bergeron et al. (2001) are shown and are representative of those in our work.

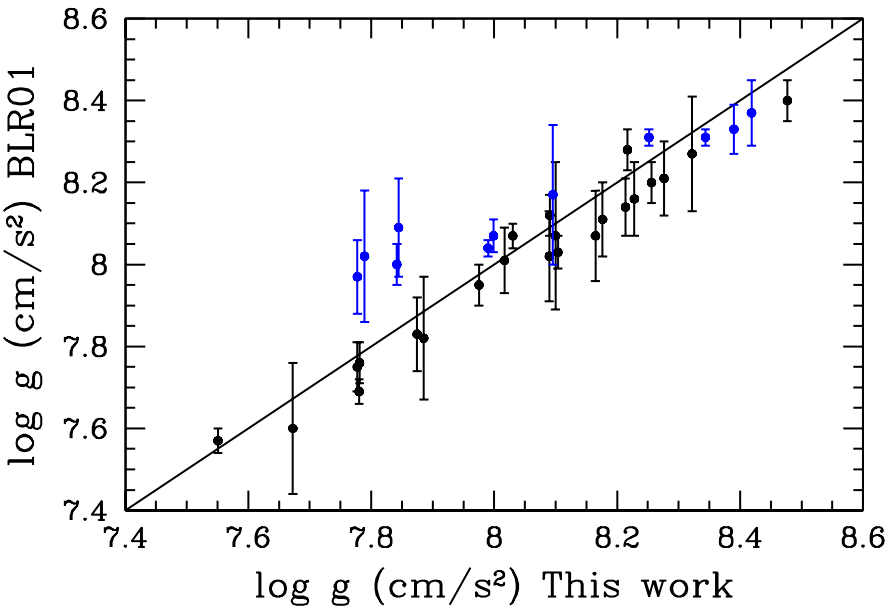

Figure 67: Comparison of gravities, g obtained by fits of our models and those obtained by Bergeron et al. (2001) (BLR01) for stars with H-rich (black) and He-rich (blue) atmospheres as classified by Bergeron et al. (2001). The uncertainties calculated by Bergeron et al. (2001) are shown and are representative of those in our work.

real. This correlation seems likely as it can be explained by a simple model of accretion from the interstellar medium.

Lets consider a single white dwarf accreting gas from the interstellar medium during its evolution at a constant accretion rate. The accreted gas has a composition of He/H $\sim$ 0.1. White dwarfs without a surface hydrogen layer have a helium convection zone that extends from the atmosphere down to $\sim 10^{-6}M$ for $T_{\rm eff} < 11000\,{\rm K}$ (Tassoul et al., 1990). The accreted gas will mix uniformly within the convection zone, where the H/He ratio will gradually increase. This change in composition could be expected to affect the depth of the convection zone. However, white dwarf models with a surface layer of hydrogen also have a convection zone that extends to $10^{-6}M$ once the star has cooled below 6000 K (Tassoul et al., 1990). It is therefore reasonable to assume that the surface convection zone has a thickness of $\sim 10^{-6}M$ for $T_{\rm eff} < 6000\,{\rm K}$, regardless of the surface composition. Then, the evolution of the composition of the atmosphere follows that of the surface convection zone and is approximately

$$\mathrm{He/H} \sim \frac{10^{-6} - \dot{M}t_{\rm WD}}{\dot{M}t_{\rm WD}}, \tag{202}$$

where $\dot{M}$ is the accretion rate and $t_{\rm WD}$ is the age of the white dwarf. The age $t_{\rm WD}$ is related to $T_{\rm eff}$ by the cooling sequence of Fontaine et al. (2001) with a surface hydrogen layer ($M_{\rm H} = 10^{-4}M$), and assuming a single white dwarf mass of $0.6\,M_{\odot}$. The evolution of the atmosphere composition from this simple model is shown in Fig. 70. An accretion rate of $\dot{M} = 6 \times 10^{-17} M_{\odot}/\mathrm{year}$ gives a good agreement with our results. This accretion rate is consistent with the Bondi-Hoyle model of accretion (Bondi & Hoyle, 1944; Hansen, 2004)

$$\dot{M} \sim \pi \frac{(GM)^2 \rho}{V^3} \sim 10^{-17} M_{\odot}\, yr^{-1} \left(\frac{V}{30\,{\rm km\,s^{-1}}}\right) n, \tag{203}$$

where V is the space velocity of the star, and n is the gas number density, which is typically $\sim 1\,cm^{-3}$ for the interstellar medium. Interestingly, we find that a variation of less than a factor of 2 in $\dot{M}$ is sufficient to account for the composition pattern we find. Our result for the composition of very cool white dwarfs strongly supports the idea that accretion from the interstellar medium coupled with convective mixing is a process that largely determines their spectral evolution (Bergeron et al., 1997). A more detailed calculation of the accretion/convective mixing is required, however, as well as an extension to higher $T_{\rm eff}$ where pure-He stars are known to exist. A larger sample of stars would improve the statistics of the stars with mixed composition, which is also desirable.

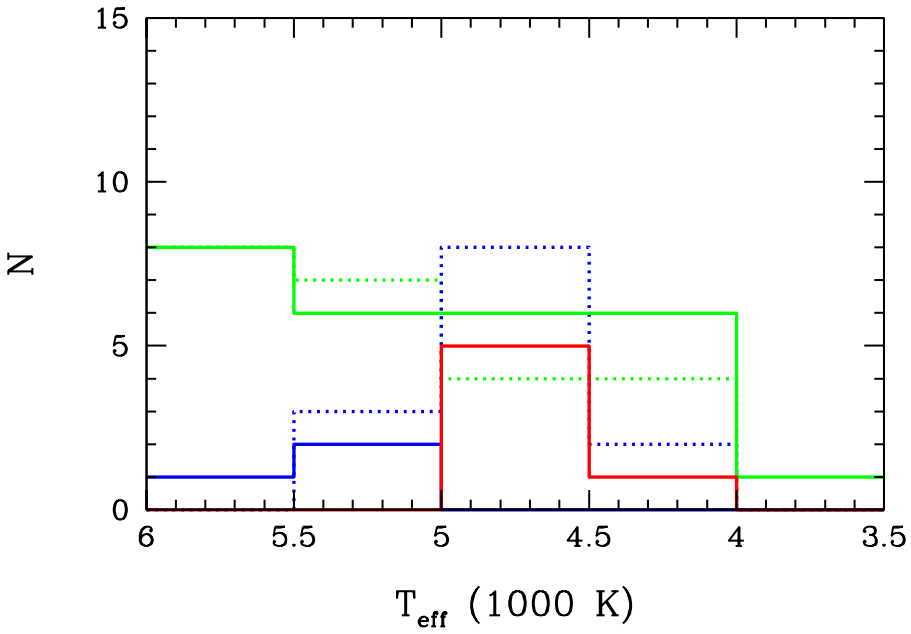

Figure 68: The distribution of the atmospheric composition of the white dwarfs in the sample of Bergeron et al. (2001) with H (solid green), $0 < \mathrm{He/H} < 1$ (solid red) and $1 < \mathrm{He/H} < 2$ (solid blue) atmospheres as determined with our models. The composition determined by Bergeron et al. (2001) for the same stars is shown with dotted lines: green for pure H and blue for pure He.

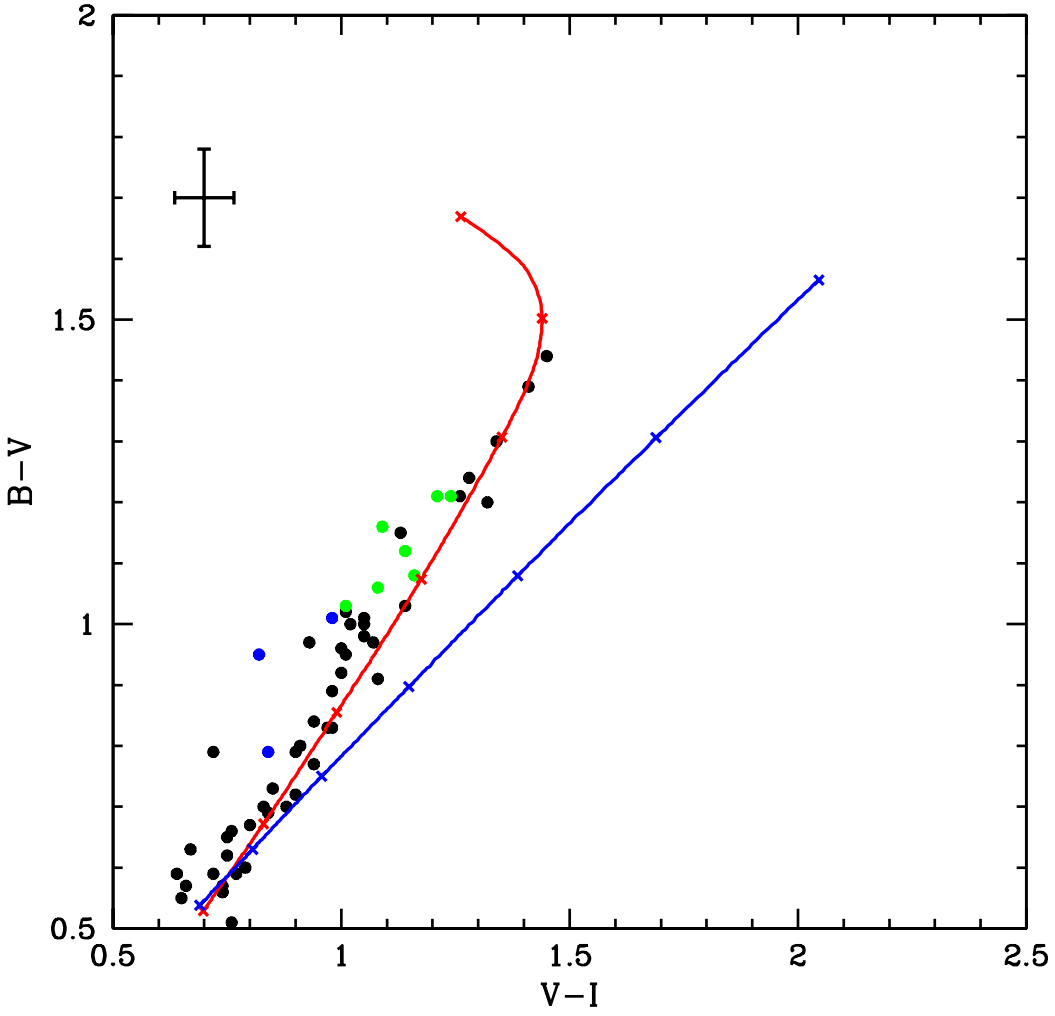

Figure 69: Color-color diagram in optical photometry for cool white dwarfs from the sample of Bergeron et al. (2001). The composition, as determined in this work, is shown by filled circles of different colors: black (hydrogen-rich), green ($0 < \mathrm{He/H} < 1$), and blue ($1 < \mathrm{He/H} < 2$). The photometric uncertainties are shown by the error bar in the upper left. The lines represent the synthetic colors of the models: pure hydrogen (red) and pure He sequence (blue). The $T_{\rm eff}$ along each curve is indicated by crosses at 6000 to 3000 K from bottom to top, in steps of 500 K. All models shown have $\log g = 8$. The DQ, DZ, and known or suspected double degenerates stars have been removed from the samples.

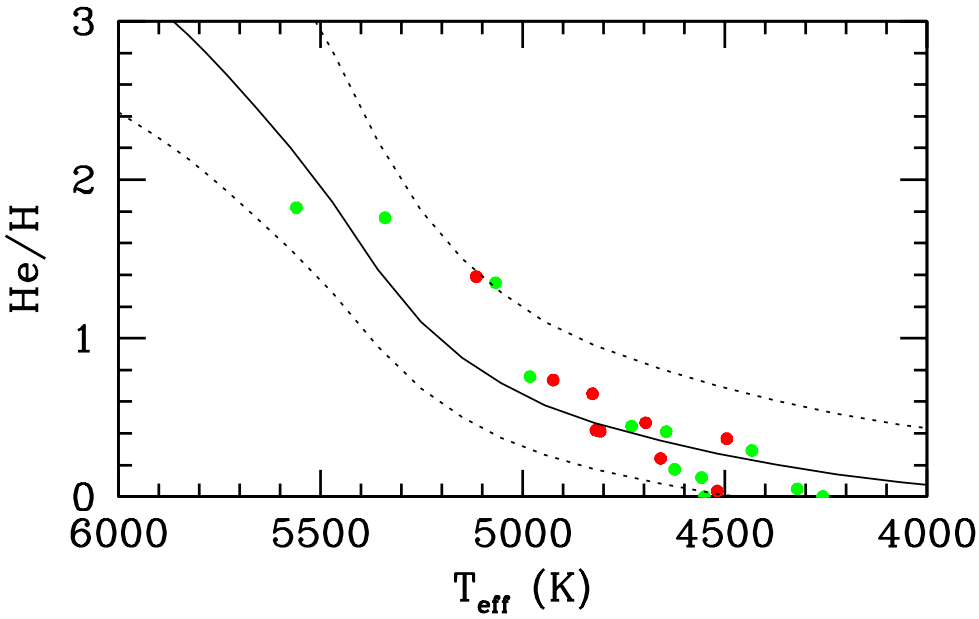

Figure 70: He/H ratio obtained in our fits to the stars of Bergeron et al. (2001) (red dots) and Bergeron et al. (2005) (green dots) to which they assigned a pure He composition. The lines represent the predictions from a simple accretion/mixing model with $\dot{M} = 6 \times 10^{-17} M_{\odot}$/year (solid curve), 7.5 $\times 10^{-17} M_{\odot}$/year (lower dotted curve), and $4.5 \times 10^{-17} M_{\odot}$/year (upper dotted curve).

CHAPTER XI

CONCLUSIONS

In this dissertation we developed models for a number of physical effects that occur in the atmospheres of cool white dwarf stars ($T_{\rm eff} \lesssim 6000\,{\rm K}$). These improvements are new and constitute important advances in modeling these objects. We have computed a new generation of atmosphere models and spectra, and performed a preliminary analysis of a well-studied sample of cool white dwarfs. These models can reproduce the data very well and reveal a new picture for the spectral evolution of very cool white dwarfs.

Having realized that in the dense atmospheres of very cool He-rich white dwarf stars the index of refraction departs significantly from unity, we have solved the general problem of radiative transfer in a refractive medium in plane-parallel geometry (Chapters II and IV). For cool white dwarfs, the most important effect of refraction on the propagation of radiation in a dispersive medium is total internal reflection. In an atmosphere in radiative equilibrium, this results in higher surface temperatures than in the non refractive case. We also find that limb darkening is dramatically reduced by refraction, a prediction that will be difficult to test, however.

It is thought that a fraction of the very cool white dwarfs have atmosphere compositions dominated by helium. In these atmospheres high densities are reached at the photosphere and the physics of dense fluids affects the equation of state, the chemistry and the opacities, effects which had largely been ignored in white dwarfs atmosphere models. We presented corrections to the abundances of the spectroscopically important species (H, H_2, H^-, He, He^+, He_2^+, and e) that arise from strong interactions with atomic helium (Chapters V–VII). We found that in dense, helium-rich, cool white dwarf atmospheres with small amount of hydrogen, the formation of H_2 and H^- is more favorable than in the ideal gas description. We investigated the ionization fraction of fluid helium with two different theoretical approaches. While the two models give different results and do not agree well with the experimental data, we can reach a firm conclusion. The number of free electrons, and hence, the He^- ff opacity, is higher than in previous models of Bergeron et al. (1995a) by $2-3$ orders of magnitude. The relatively grey He^- ff opacity becomes dominant in pure-He atmospheres, and the model spectra of pure He atmospheres stars are very close to those of black bodies. The spectra are insensitive to further variation in the density of free electrons in the atmosphere, as would

occur with changes in gravity or the addition of small amount of hydrogen or metals (as seen in DZ stars). The increased overall atmospheric opacity in pure He models will lengthen their calculated cooling times.

The existence of an unknown absorption mechanism in the atmospheres of cool, H-rich white dwarfs at short wavelengths was reported about a decade ago (Bergeron et al., 1997). This opacity source has been attributed to the pseudo-continuum, bound-free opacity from hydrogen atoms in their ground state. The lowering of the ionization potential as a result of inter-particle interactions in the gas extends the bf opacity beyond the Lyman edge at 912 Å. The simple opacity model generally used for this process in stellar atmospheres has been known for some time to fail in cool white dwarfs atmospheres. We developed a realistic semi-classical model for this absorption mechanism based on binary collisions, exact pair interaction potentials, and the ionization energy of colliding pairs (Chapter VIII). We find that the pseudo-continuum bound-free opacity decreases very rapidly with wavelength beyond the Lyman edge and becomes completely negligible beyond $\lambda \sim 2000$ Å over the entire range of temperature, density, and H/He composition relevant to cool white dwarf atmospheres. An alternative absorption mechanism at short wavelengths is the red wing of the Ly α line of hydrogen (Wolff et al., 2002). We presented a new calculation of the extreme pressure-broadening of the wing of the Ly α line by H, H_2, and He. When included in our new pure hydrogen atmosphere models, we achieved the first successful fits of the UV/optical/near-IR spectral energy distribution of the cool DA white dwarf BPM 4729. We also obtain excellent fits of the B through K spectral energy distributions of stars with hydrogen-rich atmospheres in the samples of Bergeron et al. (2001) and Bergeron et al. (2005) (Chapters IX and X). Including the broadening of the Ly α by collisions with H_2, a first in this work, is essential to reproduce the entire SED of very cool hydrogen white dwarfs. The red wing of the Ly α line and the new calculation of the He^- ff opacity are the two most important physical effects we have introduced in the models.

We have computed colors from our grid of synthetic spectra for a comparison with large samples of white dwarfs and to fit the $BVRIJHK$ photometry of individual stars. In color-color diagrams, the new pure hydrogen models follow the observed sequence of cool white dwarfs very well, whereas our improved physical description of dense helium moves the cool end of the helium sequence to the red, away from the observed sequence. This result strongly suggests that most cool white dwarfs have hydrogen atmospheres. Detailed fits of the photometry of all the DC and DA white dwarfs with $T_{\rm eff} < 6000$ K in the samples of Bergeron et al. (2001, 2005) confirm this result. For the H-rich stars, our results confirm the analysis of Bergeron et al. (1997, 2001, 2005). All of the stars they found to be H-rich are best fitted with our pure-H models (our fits

are much better in the B filter), with ($T_{\rm eff}$, g) determinations that agree well with theirs. On the other hand, we find that all of their He-rich stars (i.e., best fitted with pure He models) are not well reproduced with our pure He models. Instead, mixed composition models, with He/H ~ 1 give good fits, and we find a clear trend of decreasing He/H ratio as $T_{\rm eff}$ decreases, with all stars below 4500 K having pure H atmospheres. This trend can be explained with a simple model of accretion from the ISM and convecting mixing in the atmosphere. For the coolest subset of stars, our values of $T_{\rm eff}$ and $\log g$ are lower than those of Bergeron et al. (2001) by $200 - 300$ K and ~ 0.2 dex, respectively. This result will affect the statistics near the cutoff of the white dwarfs luminosity function (Fig. 3) as well as the mass distribution of very cool white dwarfs.

Our analysis shows that pure He (and even He rich) stars are rare among DC stars below 6000 K. The non-DA gap reported by Bergeron et al. (1997) (Fig. 4) therefore becomes non-DA "cut-off" at $T_{\rm eff} \sim 6000$ K. In a sense this result is fortunate because the difficult – and still uncertain – modeling of dense helium, which is essential to model cool, pure He atmospheres, appears not to be required to study the majority of cool white dwarfs. Our improved description of the physics of warm, dense He results in pure He synthetic spectra that deviate substantially from those observed. This is an important result. However, we have only analyzed the DA and DC stars in the sample of Bergeron et al. (2001) and Bergeron et al. (2005).

Because we focused on the physics of He/H mixture, we have purposefully ignored other, rarer types of white dwarfs such as the DZ whose spectra show lines of metals and no lines of hydrogen (§1.2.1). DZ's have been successfully modeled with He-dominated atmospheres, "polluted" by small amounts of metals. There are four known DZ stars with $T_{\rm eff} < 6000$ K, which constitute evidence that at least some very cool white dwarfs have minimal amounts, if any, of hydrogen in their atmospheres. Our improved description of the physics of He, with its significantly larger ionization fraction, justifies a new analysis of the coolest DZ stars, as this research will effect the determination of the abundances of metals from the analysis of their spectral lines. The question of whether there is any hydrogen in their atmospheres should also be revisited.

Another group of cool white dwarfs, that may have He-rich atmospheres are the so-called "ultra cool" white dwarfs (§1.2.1), which show no spectral lines and no resemblance to any model computed so far. The model fits are so poor that it is not even clear that the "ultra cool" white dwarfs are much cooler than ~ 4000 K. For all the improvements we have made to the models, we are unable to fit any of these stars, and they were not discussed here. In color-color diagrams, they fall far from the sequence of cool white dwarfs and from the model sequences. It appears likely that they have mixed He/H atmospheres, possibly dominated by helium. The inability of the models to reproduce their spectra may be a result of inadequate

$H_2 - He$ CIA and $He - He - H_2$ CIA under the extreme conditions found in He-rich atmospheres. This result is a dense physics problem we have not addressed and, in our opinion, the most important next challenge in this field.

Our new models also have implications for white dwarfs cosmochronology. We saw that the new pure He model structures are very different from those of previous calculations. The net effect will be to increase the cooling time of white dwarfs with pure He atmospheres as their surface boundary conditions. However, our work shows that such stars probably do not exist and that pure H atmospheres are sufficient for the boundary conditions of cooling models at low $T_{\rm eff}$. This simplifies the task of computing theoretical white dwarf luminosity function. Because of the introduction of the Ly α line, our pure H models have a higher overall opacity and lower pressures, which would increase somewhat the calculated cooling age of white dwarfs models with pure H atmospheres for the surface boundary condition.

In terms of the input physics, remaining problems include a new calculation of CIA opacities with more sophisticated models in regimes appropriate for very cool white dwarfs, especially $H_2 - He$ CIA and $He - He - H_2$ CIA. We also need to include the Balmer lines and the main Paschen lines of hydrogen to extend our models to $T_{\rm eff} > 6000\,{\rm K}$. This will allow for a more complete analysis of the data and a broader understanding of cool white dwarfs. We think that it will be difficult to improve on our study of the ionization of warm, dense helium in the near future. New high-quality experimental data is very much needed to validate these opacity calculations.

Our work, which focused on modeling the physics of dense He/H mixtures, represents a significant advance in the field of very cool white dwarfs. It opens the door to many new and renewed studies of the oldest stellar remains, that will slowly reveal clues to the ancient history of our Galaxy.

APPENDIX A

INDEX OF REFRACTION OF FLUID HELIUM

We compute the index of refraction of fluid helium with a semi-empirical virial expansion provided by Didier Saumon (unpublished). The expression is derived by compiling results from Langhoff & Karplus (1969); Koch et al. (1999); Moszynski et al. (1995); Hätting et al. (1999)

$$n = 1 + a(\nu) n_{\rm He} + b(\nu, T) n_{\rm He}^2, \tag{204}$$

where

$$a(\nu) = 1.5913 \times 10^9 \left(\frac{0.6097}{\nu_a^2 - \nu^2} + \frac{1.065}{\nu_b^2 - \nu^2} \right) \mathrm{cm}^3, \tag{205}$$

$$b(\nu, T) = \frac{3}{2N_A^2} \left[-0.02192X^2 + 0.00396X + 0.08453 \right. \tag{206}$$

$$\left. + \left(\frac{\nu}{\nu_0} \right)^2 (-0.01029X^2 - 0.31167X + 0.64737) \right] \tag{207}$$

$$+ \frac{a^2(\nu)}{6} \mathrm{cm}^6, \tag{208}$$

$X = \log_{10} T\,(\mathrm{K})$, $\nu_a = 5.413 \times 10^{15}\,\mathrm{Hz}$, $\nu_b = 9.771 \times 10^{16}\,\mathrm{Hz}$, $\nu_0 = 4.13414 \times 10^{16}\,\mathrm{Hz}$ and N_A is Avogadro's number. The expansion is valid as long as $n_{\rm He} < |a(\nu)/2b(\nu, T)|$. The above equations, derived by Didier Saumon, are unpublished.

APPENDIX B

CALCULATION OF MAGNITUDES FROM MODEL SPECTRA

Magnitudes at the surface of the star in each bandpass i are computed as follows

$$m = -2.5 \log f_i + c_i, \tag{209}$$

where

$$f_m = \frac{\int_0^\infty \nu^{-1} f_\nu S_i(\nu) d\nu}{\int_0^\infty \nu^{-1} S_i(\nu) d\nu} \tag{210}$$

and where $S_i(\nu)$ is the transmission function of filter i, f_ν is the modeled flux and c_i is a constant. The $BVRIJHK$ photometry is in the Vega system of magnitudes, from which

$$c_i = 2.5 \log \frac{\int_0^\infty \nu^{-1} F_\nu S_i(\nu) d\nu}{\int_0^\infty \nu^{-1} S_i(\nu) d\nu}, \tag{211}$$

where F_ν is the flux of Vega (Bohlin & Gilliland, 2004). The SDSS colors are in the AB magnitude system where c_i is a constant $c_i = -48.60$.

The transmission functions $S_i(\nu)$ are those of Bessell (1990) for the $BVRI$ filters on the Johnson-Cousins photometric system, from Bessell & Brett (1988) for the JHK filters on the Johnson-Glass system and from Fukugita et al. (1996) for the *ugriz* colors. As the JHK data of Bergeron et al. (2001) are on the CIT system for which transmission functions are not available, they were transformed to the Johnson-Glass JHK with the color transformation equations of Legget (1992).

REFERENCES

Abdallah, P. B., & Dez, V. L. 2000, JQSRT, 65, 595

Adams, W. S. 1915, Pub. Astron. Soc. Pac, 27, 236

Adams, W. S. 1925, Proc. Natl. Acad. Sci. USA, 11, 382

Allard, N. F., Koester, D., Feautrier, N., & Spielfiedel, A. 1994, A&A Supp., 108, 417

Allard, N. F., Drira, I., Gerbaldi, M., Kielkopf, J., & Spielfiedel 1998, A&A,335, 1124

Allard, N. F., Kielkopf, J. F., & Loeillet, B. 2004, A&A, 424, 347

Allard, N. F., & Kielkopf, J. F. 1982, Rev. Mod. Phys., 54, 1103

Allen, M. P., & Tildesley, D. 1987, Computer Simulation of Liquids, (Oxford: Clarendon Press)

Aulbur, W. G., Stadele, M., & Gorling, A. 2000, Phys. Rev. B, 62, 7121

Baroni, S., Dal Corso, A., de Gironcoli, S., Giannozzi, P., Cavazzoni, C., Ballabio, G., Scandolo, S., Chiarotti, G., Focher, P., Pasquarello, A., Laasonen, K., Trave, A., Car, R., Marzari, N., Kokalj, A. 2006, http://www.pwscf.org/.

Bates, D. R., & Reid, H. G. 1968, Adv. Atom. and Molec. Phys. 4, 13

Beaudet, G., Petrosian, V., & Salpeter, E. E. 1967, ApJ, 150, 979

Becke, A. D. 1988, Phys. Rev. A, 38, 3098

Bell, K.L., Berrington, K.A., & Croskery, J. P. 1982, J. Phys. B: At. Mol. Phys., 15, 977

Bergeron, P. 2001, ApJ, 558, 369

Bergeron, P., Wesemael, F., & Fontaine, G. 1991, ApJ, 367, 253

Bergeron, P., Saumon, D., & Wesemael, F. 1995, ApJ, 443, 764

Bergeron, P., Wesemael, F., & Beauchamp, A. 1995, ApJ, PASP, 107, 1047

Bergeron, P., Ruiz, M. T., & Leggett, S. K. 1997, ApJ, 108, 339

Bergeron, P., Leggett, S. K., & Ruiz, M. T. 2001, ApJS, 133, 433

Bergeron, P., Ruiz, M. T., Hamuy, M., Leggett, S. K., Currie, M. J., Lajoie, C. P., & Dufour, P. 2005, ApJ, 625, 838

Bergeron, P., & Leggett, S. K. 2002, ApJ, 580, 1070

Bessell, M. S. 1990, PASP, 102, 1181

Bessell, M. S., & Brett, J. M. 1988, PASP, 100, 1134

Bohlin, R. C., & Gilliland, R. L. 2004, AJ, 127, 3508

Bondi, H., & Hoyle, F. 1944, Mon. Not. R. Astron. Soc., 104, 273

Blochl, P.E., 1994, Phys. Rev. B, 50, 17953; Kresse, G., & Joubert, J. 1999, Phys. Rev. B, 59, 1758

Böhm, K. H., Carson, T. R., Fontaine, G., & Van Horn, H. M. 1977, ApJ, 217, 521

Böhm-Vitense, E. 1958, Zs. f. Ap., 46, 108

Boltjes, B., de Graaf, C., & de Leeuw, S. W. 1993, J. Chem. Phys., 98, 592

Bradley, P. A., 2001, ApJ, 552, 326

Broomall, J. R., Johnson, W. D. and Onn, D. G. 1976, Phys. Rev. B., 17, 2819

Boothroyd, A. I., Keogh, W. J., Martin, P. G., & Peterson, M. R. 1991, J. Chem. Phys., 95, 4343

Boothroyd, A. I., Keogh, W. J., Martin, P. G., & Peterson, M. R. 1996, J. Chem. Phys., 104, 7139

Callaway, J. 1974, Quantum Theory of the solid state (Academic Press: New York).

Cannon, C. J. 1973, AJ, 185, 621

Ceperley, D. M., & Alder, B. J. 1980, Phys. REv. Lett., 45, 566

Chandrasekhar, S. 1931, ApJ, 74, 81

Chandrasekhar, S. 1945, ApJ, 102, 223

Chayer, P., Vennes, S., Dupuis, J., & Kruk, J. W. 2005, ApJ, 630, L169

Cox, J. P., & Giuli, R. T. 1968, Principles of stellar structure, Vol. 1 (New York: Gordon and Breach), Chap. 2.

D'Antona, F., & Mazzitelli, I., Annual review of astronomy and astrophysics, 28, 139

Däppen, W., Anderson, L., & Mihalas, D. 1987, ApJ, 319, 195 (DAM)

Davydov, A. S. 1965, Quantum Mechanics (Oxford: Addison-Wesley), Chap. 12, Sec. 123

Desjarlais, M.P. 2003, Phys. Rev. B, 68, 064204

Dirac, P. A. M. 1926, Proc, Roy, Soc, London Ser. A, 112, 661

Dufour, P., Bergeron, P., & Fontaine, G. 2005, ApJ, 627, 404

Dupuis, J., Fontaine, G., Pelletier, C., & Wesemael, F. 1992, ApJS, 82, 505

Dupuis, J., Fontaine, G., & Wesemael, F. 1993, ApJS, 87, 345

Ebeling, W., Förster, A., Richert, W., & Hess, H. 1988, Physica A, 150, 159

Farihi, J. 2005, AJ, 129, 2382

Fermi, E. 1927, Rend. Accad. Lincei, 6, 602

Fontaine, G., Van Horn, H. M., Böhm, K. H., & Grenfell, T. C. 1974, ApJ, 193, 205

Fontaine, G., Graboske, H.C., & Van Horn, H.M. 1977, ApJS, 35, 293

Fontaine, G., Brassard, P., & Bergeron, P. 2001, PASP, 113, 409

Fontaine, G., & Michaud, G. 1979, ApJ, 231, 826

Ford, A. L., Kate, K. D., & Dalgarno, A. 1975, ApJ, 195, 819

Fortov, V.E., Ternovoĭ, V. Ya., Zhernokletov, M.V., Mochalov, M.A., Milkhailov, A.L., Filimonov, A.S., Pyalling, A.A., Mintsev, V.B., Gryaznov, V.K., & IosilevskiĭI.L. 2003, JETP, 97, 259

Fortov, V. E., & Iakubov, I. T. 2000, The Physics of Non-Ideal Plasma, (Singapore: World Scientific)

Fowler, R. H. 1926, Mon. Not. Roy. Astron. Soc. 87, 114

Fukugita, M., Ichikawa, T., Gunn, J. E., Doi, M., Shimasaku, K., & Schneider, D. P. 1996, AJ, 111, 1748

Gates, E et al. 2004, ApJ, 612, L129

Godby, R. W., & Schluter, M. 1986, Phys. Rev. Let., 56, 2415

Gonze, X., Beuken, J.-M., Caracas, R., Detraux, F., Fuchs, M., Rignanese, G.-M., Sindic, L., Verstraete, M., Zerah, G. , Jollet, F., Torrent, M., Roy, A., Mikami, M., Ghosez, Ph., Raty, J.-Y., & Allan, D. C. 2002, Computational Materials Science, 25, 478

Gonze, X., Rignanese, G.-M., Verstraete, M., Beuken, J.-M., Pouillon, Y., Caracas, R., Jollet, F., Torrent, M., Zerah, G., Mikami, M., Ghosez, Ph., Veithen, M., Raty, J.-Y., Olevano, V., Bruneval, F., Reining, L., Godby, R., Onida, G., Hamann, D. R., & Allan, D. C. 2005, Zeit. Kristallogr., 220, 55

Green, T. A. et al. 1974, J. Chem. Phys., 61, 5186

Greenstein, J.L. 1986, ApJ, 304, 334.

Grenfell, T. C., & Böhm, K. H. 1970, ApJ, 161, 1183

Guillot, T. 1999, Science 286, 72

Hansen, B. 1999, ApJ, 520, 680

Hansen, B. 2004, Physics Reports, 399, 1

Hansen, B.M.S. et al. 2002, ApJL, 574, L155

Harris, E. G. 1965, Phys. Rev., 138, B479

Harris, H. C., Dahn, C. C., Vrba, F. J., Henden, A. A., Liebert, J., Schmidt, G. D., & Reid, I. N. 1999, ApJ, 524, 1000

Harris, H. C. et al., 2001, ApJ, 549, L109

Harris, G. J., Lynas-Gray, A. E., Miller, S., & Tennyson, J. 2004, ApJ, 617, L143

Harris, H. C. et al. 2006, ApJ, 131, 571

Harrison, W. A. 1970, Solid State Theory (McGraw-Hill: New York).

Hart, J. F., & Herzberg, G. 1957, Phys. Rev. 106, 79

Hättig, C., Larsen, H., Olsen, J., Jørgensen, P., Koch, H., Fernández, B., & Rizzo, A. 1999, J. Chem. Phys., 111, 10099

Hauschildt, P. H. 1992, JQSRT, 47, 6, 433

Hauschildt, P. H., Storzer, H., & Baron, E. 1993, JQSRT, 51, 6, 875

Hedin, L. 1965, Phys. Rev., 139, A796

Hernanz, M., Garcia-Berro, E., Isern, J., Mochkovitch, R., Segretain, L., & Chabrier, G. 1994, ApJ, 434, 652

Hirshfeld, F. 1977, Israel Journal of Chemistry, 16, 198

Hodgkin, S. T., Oppenheimer, B. R., Hambly, N. C., Jameson, R. F., Smartt, S. J., & Steele, I. A. 2000, Nature, 403, 57

Hohenberg, P., & Kohn, W. 1964, Phys. Rev. 136, B864

Huang, Y., Xia, X., & Tan, H. 2003, Numerical Heat Transfer Part B, 44, 83

Huber, K. P., & Herzberg, G. Molecular Spectra and Molecular Structure. IV. Constants of Diatomic Molecules (Princeton 1979: Von Nostrand)

Hummer, D. G., & Mihalas, D. 1988, ApJ, 331, 794 (HM)

Ibata, R., Irwin, M., Bienaymé, O., Scholz, R., & Guibert, J. 2000, ApJ, 532, L41

Iglesias, C. A., Rogers, F. J., & Saumon, D. 2002, ApJ, 569, L111

Jackson, J. D. 1975, Classical Electrodynamics, (New York: John Willey & Sons)

John, T. L., 1988, A&A, 193, 189

Johnson, K. A., & Ashcroft, N. W. 1998, Phys. Rev. B. 58, 584

Kapranidis, S. 1983, ApJ, 275, 342

Karsas, W. J., & Lather, R. 1961, ApJS, 6, 167

Kestner, N. R., Jortner, J., Cohen, M. H., & Rice, S. A. 1965, Phys. Rev. A, 140, 56

Kilic, M., Munn, J. A., Harris, H. C., Liebert, J., von Hippel, T., Williams, K. A., Metcalfe, T. S.,Winget, D. E., & Levine, S. E. 2005, preprint (astro-ph/0503601)

Kilic, M., Munn, J. A., Harris, H. C., Liebert, J., von Hippel, T., Williams, K. A., Metcalfe, T. S., Winget, D. E., & Levine, S. E. 2006, AJ, 131, 582

Kilic, M., von Hippel, T., Leggett, S. K., & Winget, D. E. 2006, ApJ, 646, 474

Koch, H., Hättig, C., Larsen, H., Olsen, J., Jørgensen, P., Fernández, B., & Rizzo, A. 1999, J. Chem. Phys. 111, 10108

Koch, W. & Holthausen, M. C. 2000, A chemist's guide to density functional theory, (Weinheim: WILEY-VCH)

Koester, D. 2002, A&A, 11, 33

Koester, D., & Knist, S. 2006, A&A, 454, 951

Koester, D., & Wolff, B. 2000, A&A, 357, 587

Kohn, W. & Sham, L. J. 1965, Phys. Rev., 140, A1133

Kolos, W., & Wolniewicz, L. 1965, J. Chem. Phys. 43, 2429

Kowalski, P. M. 2006a, ApJ, 641, 488

Kowalski, P. M. 2006b, ApJ, 651, 1120

Kowalski, P. M., Saumon, D., & Mazevet, S. 2005, ASP Conf. Ser. 334, White Dwarfs, ed. Koester, D., & Moehler, S. (San Francisco: ASP), 203

Kowalski, P. M., Mazevet, S., & Saumon, D. 2006, in Proceedings of the 14th APS Topical Conference on Shock Compression of Condensed Matter –2005, M. D. Furnish, M. L. Elert, T. P. Russell and C. T. White., Eds., in press (2006)

Kowalski, P. M., & Saumon, D. 2004, ApJ, 607, 970

Kowalski, P. M., & Saumon, D. 2006, ApJL, 651, L137

Kraeft, W. D., Kremp, D., Ebeling, W., & Röpke, G. 1986, Quantum Statistics of Charged Particle Systems, (New York: Plenum Press)

Kress, J.D., Mazevet, S., Collins, L.A., & Wood, W. W. 2001, Phys. Rev. B, 63, 024203

Kresse, G., & Hafner, J., 1993, Phys. Rev. B, 47, RC558; Kresse, G., & Furthmüller, J. 1996, Comput. Mat. Sci., 6, 15; Kresse, G., & Furthmüller, J. 1996, Phys. Rev. B, 54, 11169

Kuhlbrodt, S., Redmer, R., Reinholz, H., Röpke, G., Holst, B., Mintsev, V. B., Gryaznov, V. K., Shilkin, N. S., & Fortov, V. E. 2005, Contrib. Plasma Phys., 45, 61

Kurucz, R. L. 1970, SAO report, 309

Langhoff, P.W., Karplus, M., 1969, J. Opt. Soc. Am. 59, 863

Legget, S. K. 1992, ApJS, 82, 351

Lee, C., Yang, W., & Parr, R. G. 1988, Phys. Rev. B, 37, 785

Liebert, J., Dahn, C.C., Gresham, M., & Stritmatter, P. A. 1979, ApJ, 233, 226

Liebert, J., Wesemael, F., Hansen, C.J., Fontaine, G., Shipman, H.L., Sion, E.M., Winget, D.E., & Green, R.F. 1986, ApJ, 309, 241

Liebert, J., Dahn, C.C, & Monet, D.G., 1988, ApJ, 332, 891.

Liebert, J., Bergeron, P., & Holberg, J. B. 2005, ApJS, 156, 47

MacDonald, J., Hernanz, M., & Jos, J. 1998, Mon. Not. R. Astron. Soc. 296, 523

Malo, A., Wesemael, F., & Bergeron, P. 1999, ApJ, 322, 891

Marchi, R. P., & Smith, F. T. 1965, Phys. Rev. A, 139, 1025

Martin, R. M. 2004, Electronic structure (Cambridge University Press: New York).

Martynov, G. A. 1992, Fundamental theory of liquids (Bristol: Adam Hilger), Chap. 5, 6 and 10

Mazevet, S., Kress, J., & Collins, L.A. 2004, "Atomic Processes in Plasmas", AIP Conf. Proc. 730, 139 (AIP, Melville, 2004).

Mazevet, S., Collins, L. A., Magee, N.H., Kress. J. D., & Keady. J. J. 2003, A&Ap, 405, L5

McCook, G. P., & Sion, E. M. 1999, ApJS, 121, 1

Mermin, N.D. 1965, Phys. Rev., 137A, 1441

Mestel, L, Mon. Not. Roy. Astron. Soc. 1952, 112, 583

Mihalas, D. 1978, Stellar Atmospheres (San Francisco: W. H. Freeman)

Militzer, B., 2006, Phys. Rev. Lett., in press

Moszynski, R., Heijmen, T. G. A., & van der Avoird, A. 1995, Chem. Phys. Lett. 247, 440

Nellis, W. J., Holmes, N. C., Mitchell, A. C., Trainor, R. J., Governo, G. K., Ross, M., & Young, D. A. 1984, Phys. Rev. Lett., 53, 1248

Nikiforov, A. F., Novikov, V. G., & Uvarov, V. B. 2005, "Quantum-Statistical Models of Hot Dense Matter", (Basel: Birkhäuser Verlag)

Olson, R. E., & Mueller, C. R. 1967, J. Chem. Phys. 46, 3810

Olson, G. L., Auer, & L. H., Buchler, J. R. 1986, JQSRT, 35, 6, 431

Olson, G.L., & Kunasz, P.B. 1987, JQSRT, 38, 5, 325

O'Marley, T. F., Burke, P. G., & Berrington, K. A. 1978, J. Phys. B, 12, 953

Onida, G., Reining, L., & Rubio, A. 2002, Rev. Mod. Phys., 74, 601

Oppenheimer, B. R., Saumon, D., Hodgkin, S. T., Jameson, R. F., Hambly, N. C., Chabrier, G., Filippenko, A. V., & Brown, M. E. 2001, ApJ, 550, 448

Oppenheimer, B. R., Hambly, N. C., Digby, A. P., Hodgkin, S. T., & Saumon, D. 2001, Science, 292, 698

Palenius, H. P., Kohl, J. L., & Parkinson, W. H. 1975 Phys. Rev. A. 13, 1805

Pelletier, C., Fontaine, G., Wesemael, F., Michaud, G., & Wegner, G. 1986, ApJ, 307, 242

Peng, Z., Kristyan, S., & Kuppermann, A. 1995, Phys. Rev. A, 52, 1005

Perdew, J.P. & Wang, Y. 1992, Phys. Rev. B, 46, 12947

Perdew, J. P., Burke, K., & Ernzerhof, M. 1996, Phys. Rev. Lett., 77, 3865

Perdew, J. P., Ernzerhof, M. & Burke, K. 1996, J. Chem. Phys., 105, 9982

Perdew, J. P. and Levy, M. 1997, Phys. Rev. B., 56, 16021

Pedrew, J. P. & Wang, Y. 1992, Phys Rev. B., 45, 13244

Pomranin, G. C. 1968, ApJ, 153, 321

Prosmiti, R. Polyansky, O. L. and Tennyson, J. 1997, Chem. Phys. Lett. 273, 107

Redmer, R., Juranek, H., Kuhlbrodt, S., & Schwarz, V. 2003, Z. Phys. Chem., 21, 783

Ree, F. H. 1983, J. Chem. Phys., 78, 409

Richer et al. 2006, Science, 313, 936

Ross, M., Ree, F. H., & Young, D. A. 1983, J. Chem. Phys., 79, 1487

Ross, M., & Young, D. A. 1986, Phys. Lett. A, 118, 463

Rybicki, G. 1971, JQSRT, 11, 589

Salaris, M., Dominguez, I., Garcia-Berro, E., Hernanz, M., Isern, J., & Mochkovitch, R. ApJ, 486, 413

Sando, K., Doyle, R. O., & Dalgarno, A. 1969, ApJ, 157, L143

Saumon, D., & Chabrier, G. 1991, Phys. Rev. A, 44, 5122

Saumon, D., & Chabrier, G. 1992, Phys. Rev. A., 46, 2084

Saumon, D., Chabrier, G., & Van Horn, H.M., 1995, ApJS, 99, 713

Saumon, D., & Guillot, T. 2004, ApJ, 609, 1170

Saumon, D., & Jacobson, 1999, ApJ, 511, L107

Schatzman, E. 1958, (Amsterdam: North-Holland)

Schmidt, M. 1959, ApJ, 129, 243

Schmidt, G. D., Bergeron, P., & Fegley, B. 1995, ApJ, 443, 274

Schwarz, K. W. 1978, Phys. Rev. Lett., 41, 239

Scifoni, E., Dellepiane, G., & Gianturco, F. A. 2004, Eur. Phys. J. D, 30, 353

Seaton, M. J., Yan, Y., Mihalas, D., & Prodhan, A. K. 1994, MNRAS, 266, 805

Shafer, R., & Gordon, R. G. 1973, J. Chem. Phys., 58, 5422

Shalabi, A. S., Eid, Kh. M., Kamel, M. A., & El-Barbary, A. A. 1998, Physics Letters A, 239, 87

Shapiro, S. L., & Teukolsky, S. A. 1983, Black Holes, White Dwarfs, and Neutron Stars: The physics of compact objects (New York: John Willey & Sons), Chap. 3

Shipman, H. L. 1977, ApJ, 213, 138

Sion, E.M. 1984, ApJ, 282, 612

Sion, E.M. et al. 1983, ApJ, 269, 253

Stancil, P. C. 1994, ApJ, 430, 360

Staszewska, G. & Wolniewicz, L. 1999, J. Mol. Spect., 198, 416

Tang, K. T., & Yang, X. D. 1990, Phys. Rev. A, 42, 311

Tankersley, L. L. 1973, J. Low. Temp. Phys., 11, 451

Tao, F. 1993, J. Chem. Phys., 100, 4942

Tassoul, M., Fontaine, G., & Winget, D. E. 1990, ApJS, 72, 335

Theodorakopoulos, G., Petsalakis, I. D., Nicolaides, C. A., & Buenker, R. J. 1987, J. Phys. B., 20, 2339

Thomas, L. H. 1927, Proc. Camb. Phil. Soc., 23, 542

Tschumper, G. S., & Schaefer, H. F. 1997, J. Chem. Phys., 107, 2529

von Hippel, T. 2005, ApJ, 662, 565

Vyrdov, O. A., & Scuseria, G. E. 2005, J. Chem. Phys. 122, 184107

Winget, D. E., Hansen, C. J., Liebert, J., Van Horn, H. M., Fontaine, G., Nather, R. E., Kepler, S. O., & Lamb, D. Q. 1987, ApJL, 315, L77

Winisdoerffer, C., &, Chabrier, G. 2005, Phys. Rev. E, 71, 026402

Wolff, B., Koester, D., & Liebert, J. 2002, A&A, 385, 995

Wood, M.A. 1995, In Proceedings of the 9th European Workshop on White Dwarfs, Editors: D. Koester, & K. Werner, Lecture Notes in Physics vol. 43, Springer, Heidelberg

Young, D.A., McMahan, A.K., & Ross, M. 1981, Phys. Rev. B., 24, 5119

Yuan, J. 1988, J. Phys. B, 21, 3753

Zeldovich, Ya., & Raizer, Yu. 1966, Physics of Shock Waves and High-Temperature Hydrodynamic Phenomena (Academic Press: New York)

Zheleznyakov, V. V. 1967, ApJ, 148, 849

Zuckerman, B., Koester, D., Reid, I. N., & Hünsch, M. 2003, ApJ, 596, 477